UNIVERSITY OF CALIFORNIA,
IRVINE

Developing New Ideas with ATLAS: Dark Matter Searches, Detector Upgrades, and Phenomenology

DISSERTATION

submitted in partial satisfaction of the requirements
for the degree of

DOCTOR OF PHILOSOPHY

in Physics

by

Kevin Thomas Bauer

Dissertation Committee:
Professor Daniel Whiteson, Chair
Professor Andrew Lankford
Professor Mu-Chun Chen

2019

TABLE OF CONTENTS

Page

LIST OF FIGURES **v**

LIST OF TABLES **xi**

ACKNOWLEDGMENTS **xiii**

CURRICULUM VITAE **xiv**

ABSTRACT OF THE DISSERTATION **xvi**

1 Introduction **1**
- 1.1 The Standard Model . . . 1
  - 1.1.1 Historical background . . . 1
  - 1.1.2 Overview . . . 2
  - 1.1.3 Incompleteness of the Standard Model . . . 3
- 1.2 Dark Matter . . . 4
  - 1.2.1 Evidence . . . 4
  - 1.2.2 Dark Matter Candidate Theories . . . 6

2 The Large Hadron Collider (LHC) and the ATLAS Detector **8**
- 2.1 The LHC . . . 8
- 2.2 ATLAS . . . 9
  - 2.2.1 The ATLAS Coordinate System . . . 10
  - 2.2.2 The Inner Detector . . . 11
  - 2.2.3 The Calorimeters . . . 14
  - 2.2.4 The Muon Spectrometer (MS) . . . 16
  - 2.2.5 Reconstruction of Physics Objects in ATLAS . . . 17
  - 2.2.6 Dark Matter Research Using ATLAS . . . 21

3 FELIX: the new detector readout system for the ATLAS experiment **23**
- 3.1 Introduction . . . 23
- 3.2 FELIX as a System . . . 25
- 3.3 FELIX Hardware Prototype . . . 26
- 3.4 FELIX Software and Data Transfer . . . 27
- 3.5 Conclusions . . . 28

4 Mono Z' Phenomenology **29**
4.1 Introduction . . . 29
4.2 Current Constraints on Z' Bosons . . . 31
4.2.1 Dijet Constraints . . . 33
4.2.2 Dilepton Constraints . . . 33
4.2.3 Other Limits . . . 34
4.3 Models of $Z' + \not{E}_{\mathrm{T}}$ production . . . 35
4.3.1 Dark Higgs . . . 35
4.3.2 Light Vector . . . 37
4.3.3 Light Z' with Inelastic EFT coupling . . . 41
4.4 LHC Sensitivity . . . 42
4.4.1 Dijet Mode . . . 42
4.4.2 Dilepton mode . . . 44
4.5 Discussion . . . 48
4.5.1 Model Constraints . . . 51
4.6 Conclusions . . . 54

5 ATLAS Mono V/Z' Search **56**
5.1 Introduction . . . 56
5.2 Signal models . . . 57
5.3 Simulated signal and background samples . . . 59
5.4 Object reconstruction and identification . . . 62
5.5 Event selection and categorization . . . 66
5.6 Background estimation . . . 74
5.7 Systematic uncertainties . . . 77
5.8 Results . . . 80
5.8.1 Statistical interpretation . . . 80
5.8.2 Measurement results . . . 81
5.8.3 Constraints on invisible Higgs boson decays . . . 88
5.8.4 Constraints on the simplified vector-mediator model . . . 89
5.8.5 Mono-W/Z constraints with reduced model dependence . . . 91
5.8.6 Constraints on mono-Z' models . . . 95
5.9 Summary . . . 98

6 Jet Substructure **100**
6.1 Introduction . . . 100
6.2 Theory . . . 102
6.3 Data . . . 103
6.4 Training . . . 107
6.5 Results . . . 109
6.6 Interpretation . . . 111
6.7 Discussion . . . 112

7 Muon Images **117**
7.1 Introduction . . . 117
7.2 Approach . . . 118
7.3 Data Generation . . . 119
7.4 Neural Network Architecture . . . 120
7.4.1 Low level images . . . 120
7.4.2 High level variables . . . 121
7.5 Results . . . 124
7.5.1 Low Level compared to Isolation . . . 124
7.6 Results . . . 125
7.6.1 Low Level compared to Isolation+EFP variables . . . 125
7.7 Conclusion . . . 127

Bibliography **129**

LIST OF FIGURES

Page

1.1 Overview of the elementary particles of the Standard Model [1] 3
1.2 A comparison of the expected vs observed velocity as a function of distance from the center for an example galaxy [3] 5

2.1 A schematic of the ATLAS detector and its subdetectors. The LHC beam runs horizontal in this image [12] 10
2.2 A schematic of the ATLAS inner detector for tracking charged particles from the collision point [12] 12
2.3 A schematic of the ATLAS calorimeter system for stopping and measuring the properties of photons, electrons, and hadrons [12] 15
2.4 A schematic of the ATLAS Muon Spectrometer system for identifying and measuring the momentum of muons [12] 16
2.5 A cross-section schematic of the ATLAS detector and how particles interact with the system [13] 18
2.6 An example mono-jet event where an invisible particle(s) is traveling opposite to an energetic jet [18] 22

3.1 Current TDAQ System [21]. 24
3.2 Planned TDAQ System by 2024. Some systems will be upgraded to FELIX in 2019 [21]. 25
3.3 Overview of the FELIX system. FELIX consists of a PCIe card (FLX Card), a PC running a software application, and a Network Interface Card (NIC). . 26
3.4 The FLX-711 Card [20] 27

4.1 Diagram of the production of a Z' in association with a dark Higgs boson (h_D) which decays into two stable dark states, χ. It is assumed that h_D is lighter than $2M_{Z'}$ and decays with 100% branching to the invisible states. . 36
4.2 Diagram of the production of $\chi_1\chi_2$, followed by decay of the heavier dark sector state χ_2 to $Z' + \chi_1$, where χ_1 is a possible dark matter candidate. . . 38
4.3 Distribution of reconstructed $\not{E}_{\mathrm{T}}$ (*left*) and m_{jj} (*right*) in the $jj + \not{E}_{\mathrm{T}}$ final state for each of the three models considered. We show a subset of our Z' mass points and consider the two cases for the masses of the other states, as discussed in the text. 40

4.4 Distribution of reconstructed m_{jj} in the $jj + \not{E}_{\rm T}$ final state, for the expected SM background as well as several examples of the signal in the dark Higgs (DH) model. Events are required to satisfy the preselection as well as have $\not{E}_{\rm T} > 300$ GeV and leading jet $p_{\rm T} > 250$ GeV, but no m_{jj} selection is applied. 43
4.5 (*Left*) Efficiency of the $jj+\not{E}_{\rm T}$ selection described in the text, for two choices of mass spectra in each of the three models considered. Note that the minimum required $\not{E}_{\rm T}$ increases above $m_{Z'} > 100$ GeV. (*Right*) 95% CL upper limits on the production of $Z' \to jj + \not{E}_{\rm T}$ as a function of the Z' mass. 44
4.6 Distribution of reconstructed $\not{E}_{\rm T}$ (*left*) and $m_{\ell\ell}$ (*right*) in the $\ell\ell + \not{E}_{\rm T}$ final state for each of the three models considered. We show a subset of our Z' mass points and consider the two cases for the masses of the other states, as discussed in the text. 45

4.7 Distribution of reconstructed $m_{\ell\ell}$ in the $\mu^+\mu^-+\not{E}_{\rm T}$ final state, for the expected background as well as a signal example. The IFT label refers to the inelastic EFT model. Events are required to satisfy the preselection as well as have $\not{E}_{\rm T} > 100$ GeV and $p_{\ell\ell} > 80$ GeV, but no $m_{\ell\ell}$ selection is applied. 47
4.8 (*Left*) Efficiency of the $\mu^+\mu^- + \not{E}_{\rm T}$ selection described in the text as a function of the Z' mass, for two choices of mass spectra in each of the three models considered. (*Right*) 95% CL upper limits on the production of $(Z' \to \mu^+\mu^-) + \not{E}_{\rm T}$ as a function of the Z' mass. 48
4.9 Expected upper limits at 95% CL on the product of couplings $g_q g_{h_D}$ as a function of $M_{Z'}$ for the dark Higgs model, for 8 TeV pp collisions in two different mass benchmarks. Left, the sensitivity of the $jj + \not{E}_{\rm T}$ channel is compared to the constraint on the hadronic Z width (labelled R_Z), shown in black for $g_{h_D} = 1$ (solid) and $g_{h_D} = 2$ (dashed), as well as direct dijet resonance searches [63] for a new Z'. Right, the sensitivity of the $\mu\mu + \not{E}_{\rm T}$ channel is compared to various dimuon resonance searches at CDF [70] and ATLAS [71], all shown for $g_{h_D} = 1$. The low-mass dimuon limits are interpreted from the results of Ref. [75]: both 7 TeV recast limits (dotted) and 8 TeV sensitivity projections (dashed) are shown. We do not consider masses in the grey shaded region due to the extremely large Drell-Yan background near the Z mass. . 49
4.10 Expected upper limits at 95% CL on the product of couplings $g_q g_{h_D}$ as a function of $M_{Z'}$ in the Light Vector model, for 8 TeV pp collisions in two different mass benchmarks. The dijet and dilepton resonance limits are the same as those in Fig. 4.9, with $g_\chi = 1$ for all dilepton resonance limts. . . . 49
4.11 Expected lower bound at 95% CL on Λ from in the Inelastic EFT model, for 8 TeV pp collisions in two different mass benchmarks. The branching ratio of the Z' to jets and muons is taken to be 100% in each case. 50

5.1 Examples of dark matter particle (χ) pair-production (top left) in association with a W or Z boson in a simplified model with a vector mediator Z' between the dark sector and the SM [96]; (top right) via decay of the Higgs boson H produced in association with the vector boson [98, 99, 100, 101, 102]; (bottom left) in association with a final-state Z' boson via an additional heavy dark-sector fermion (χ_2) [94] or (bottom right) via a dark-sector Higgs boson (h_{D}) [94]. 58
5.2 Expected distributions of missing transverse momentum, $E_{\mathrm{T}}^{\mathrm{miss}}$, normalized to unit area, for the simplified vector-mediator model and invisible Higgs boson decays after the full selection in the (a) resolved and (b) merged event topologies, and the expected invariant mass distributions (c) m_{jj} in the resolved and (d) m_J in the merged event topologies, before the mass window requirement. The signal contributions from each resolved (merged) category are summed together. The invisible Higgs boson decays include a large contribution from ggH events, which results in the observed mass distribution. 71
5.3 Expected distributions of missing transverse momentum, $E_{\mathrm{T}}^{\mathrm{miss}}$, normalized to unit area, after the full selection for the dark-fermion mono-Z' model in the (a) resolved and (b) merged event topologies, the dark-Higgs mono-Z' model in the (c) resolved and (d) merged event topologies, as well as the expected invariant mass distribution (e) m_{jj} in the resolved and (f) m_J in the merged event topologies for the dark-fermion mono-Z' model in the light dark-sector scenario before the mass window requirement. Similar mass distributions are also observed in the simulation of the other mono-Z' models. 72
5.4 The product of acceptance and efficiency $(\mathcal{A} \times \varepsilon)_{\mathrm{total}}$, defined as the number of signal events satisfying the full set of selection criteria, divided by the total number of generated signal events, for the combined mono-W and mono-Z signal of the simplified vector-mediator model and for the mono-Z' dark-fermion and dark-Higgs signal models, shown in dependence on the mediator mass $m_{Z'}$. For a given model, the signal contributions from each category are summed together. The lines are drawn to guide the eye. 73
5.5 The observed (dots) and expected (histograms) distributions of missing transverse momentum, $E_{\mathrm{T}}^{\mathrm{miss}}$, obtained with 36.1 fb^{-1}of data at $\sqrt{s} = 13$ TeV in the mono-W/Z signal region with the merged event topology after the profile likelihood fit (with $\mu = 0$), shown separately for the (a) 0b-HP, (b) 0b-LP, (c) 1b-HP, (d) 1b-LP, and (e) 2b-tag event categories. The total background contribution before the fit to data is shown as a dotted blue line. The hatched area represents the total background uncertainty. The signal expectations for the simplified vector-mediator model with $m_\chi = 1$ GeV and $m_{Z'} = 600$ GeV (dashed red line) and for the invisible Higgs boson decays (dashed blue line) are shown for comparison. The inset at the bottom of each plot shows the ratio of the data to the total post-fit (dots) and pre-fit (dotted blue line) background expectation. 84

5.6 The observed (dots) and expected (histograms) distributions of missing transverse momentum, $E_{\mathrm{T}}^{\mathrm{miss}}$, obtained with 36.1 fb^{-1}of data at $\sqrt{s} = 13$ TeV in the mono-W/Z signal region with the resolved event topology after the profile likelihood fit (with $\mu = 0$), shown separately for the (a) 0b-, (b) 1b- and (c) 2b-tag categories. The total background contribution before the fit to data is shown as a dotted blue line. The hatched area represents the total background uncertainty. The signal expectations for the simplified vector-mediator model with $m_\chi = 1$ GeV and $m_{Z'} = 600$ GeV (dashed red line) and for the invisible Higgs boson decays (dashed blue line) are shown for comparison. The inset at the bottom of each plot shows the ratio of the data to the total post-fit (dots) and pre-fit (dotted blue line) background expectation. 85

5.7 The observed (dots) and expected (histograms) distributions of missing transverse momentum, $E_{\mathrm{T}}^{\mathrm{miss}}$, obtained with 36.1 fb^{-1}of data at $\sqrt{s} = 13$ TeV in the mono-Z' signal region with $m_{Z'} = 90$ GeV and the merged event topology after the profile likelihood fit (with $\mu = 0$), shown separately for the (a) 0b-HP, (b) 0b-LP, (c) 1b-HP, (d) 1b-LP, and (e) 2b-tag event categories. The total background contribution before the fit to data is shown as a dotted blue line. The hatched area represents the total background uncertainty. The expectations for the selected dark-Higgs (dashed red line) and dark-fermion (dashed blue line) signal points are shown for comparison. The inset at the bottom of each plot shows the ratio of the data to the total post-fit (dots) and pre-fit (dotted blue line) background expectation. 86

5.8 The observed (dots) and expected (histograms) distribution of missing transverse momentum, $E_{\mathrm{T}}^{\mathrm{miss}}$, obtained with 36.1 fb^{-1}of data at $\sqrt{s} = 13$ TeV in the mono-Z' signal region with the resolved event topology after the profile likelihood fit (with $\mu = 0$), shown separately for the (a,b) 0b, (c,d) 1b and (e,f) 2b-tag event categories. On the left-hand side, the mediator mass of 90 GeV and on the right-hand side of 350 GeV is assumed. The total background contribution before the fit to data is shown as a dotted blue line. The hatched area represents the total background uncertainty. The expectations for the selected dark-Higgs (dashed red line) and dark-fermion (dashed blue line) signal points are shown for comparison. The inset at the bottom of each plot shows the ratio of the data to the total post-fit (dots) and pre-fit (dotted blue line) background expectation. 87

5.9 (a) Observed upper limits on the signal strength μ at 95% CL in the grid of the DM and mediator particle masses, (m_χ, $m_{Z'}$), for the combined mono-W and mono-Z search in the simplified vector-mediator model with Dirac DM particles and couplings $g_{\mathrm{SM}} = 0.25$ and $g_{\mathrm{DM}} = 1$. There are no interpolated points and thus no limit values listed for the mass point (m_χ = 100 GeV, $m_{Z'}$ = 10 GeV) and in the parameter region (m_χ = 10 GeV, $m_{Z'}$ = 200–2000 GeV). (b) The corresponding exclusion contours at 95% CL. The black solid (dashed) curve shows the observed (expected) limit. The dotted magenta curve corresponds to the set of points for which the expected relic density is consistent with the WMAP [169] and Planck [170] measurements ($\Omega h^2 = 0.12$), as computed with MadDM [171]. The region below the curve corresponds to higher predicted relic abundance than these measurements. . 92
5.10 Upper limits at 95% CL on the visible cross section $\sigma_{\mathrm{vis},\,W+\mathrm{DM}}$ (left) and $\sigma_{\mathrm{vis},\,Z+\mathrm{DM}}$ (right) in the six $E_{\mathrm{T}}^{\mathrm{miss}}$ regions, after all selection requirements, but inclusive in the b-tag multiplicity and the W/Z candidate mass m_{jj}/m_J. The observed limits (solid line) are consistent with the expectations under the SM-only hypothesis (dashed line) within uncertainties (filled bands). 93
5.11 Upper limits at 95% CL on the cross section times the branching ratio $\mathcal{B}_{Z'\to q'q}$ in mono-Z' models as a function of the mediator mass, $m_{Z'}$, for the dark fermion model in the (a) light and (b) heavy dark-sector scenario, as well as the dark Higgs model in the (c) light and (d) heavy dark-sector scenario. . . 96
5.12 Upper limits at 95% CL on the product of couplings g_{SM} g_{DM} in mono-Z' models as a function of the mediator mass for the dark fermion model in the (a) light and (b) heavy dark-sector scenario, as well as the dark Higgs model in the (c) light and (d) heavy dark-sector scenario. 97

6.1 Distributions in simulated samples of high-level jet substructure variables widely used to discriminate between jets due to collimated decays of massive objects ($W \to qq$) and jets due to individual quarks or gluons (QCD). Two cases are shown: with and without the presence of additional in-time pp interactions, included at the level of an average of 50 such interactions per collision. 105
6.2 Typical jet images from class 1 (single QCD jet from q or g) on the left, and class 2 (two overlapping jets from $W \to qq'$) on the right, after preprocessing as described in the text. 106
6.3 Average of 100,000 jet images from class 1 (single QCD jet from q or g) on the left, and class 2 (two overlapping jets from $W \to qq'$) on the right, after preprocessing. 107
6.4 Signal efficiency versus background rejection (inverse of efficiency) for deep networks trained on the images and boosted decision trees trained on the expert features, both with (bottom) and without pile-up (top). Typical choices of signal efficiency in real applications are in the 0.5-0.7 range. Also shown are the performance of jet mass individually as well as two expert variables in conjunction with a mass window. 111

6.5 Distributions in simulated samples without pileup of high-level jet substructure variables for pure signal ($W \to qq$) and pure background (QCD) events. To explore the decision surface of the ML algorithms, also shown are background events with various levels of rejection for deep networks trained on the images and boosted decision trees trained on the expert features. Both algorithms preferentially select jets with values near the peak signal values. Note, however, that while the BDT has been supplied with these features as an input, the DNN has learned this on its own. 113
6.6 Distributions in simulated samples with pileup of high-level jet substructure variables for pure signal ($W \to qq$) and pure background (QCD) events. To explore the decision surface of the ML algorithms, also shown are background events with various levels of rejection for deep networks trained on the images and boosted decision trees trained on the expert features. Both algorithms preferentially select jets with values near the peak signal values. Note, however, that while the BDT has been supplied with these features as an input, the DNN has learned this on its own. 114

7.1 Average calorimeter images in the vicinity of reconstructed muons within a cone of $R = 0.4$. The color of each cell represents the sum of the E_T of the calorimeter deposits within the cell. Left are images from muons inside heavy boson decays, right are images from muons within b-quark jets. 119
7.2 Signal efficiency versus background rejection (inverse of efficiency) for deep networks trained on muon images, shallow networks trained on a set of isolation cones and the most widely-used approach: a single isolation cone. 122
7.3 Comparison of classification performance using the metric AUC (Area Under the Curve of signal efficiency versus background efficiency, see Fig 7.2) between the deep networks trained on muon images and shallow networks with increasing numbers of isolation cones. 123
7.4 Comparison of classification performance using the metric AUC (Area Under the Curve of signal efficiency versus background efficiency, see Fig 7.2) between the deep networks trained on muon images and shallow networks with increasing numbers of EFP graphs. Kevin add N=1,2,4,8 iso + EFP 125
7.5 Discriminant ordering between different networks. A score of 1.0 indicates perfect similarity. The diagonal is measured as the DO between two networks trained with identical inputs but different initial conditions. 126
7.6 ROC curve comparing LL CNN with ATLAS state of the art isolation and our best HL network build from a combination of isolation and EFP 128

LIST OF TABLES

Page

4.1 Signal efficiency and expected background yields for several Z' masses in the $jj + \not{E}_{\mathrm{T}}$ final state. Only the heavy mass spectrum choice is listed. The background uncertainty is 27% obtained by varying the renormalization and factorization scales by factors of two. 46

4.2 Signal efficiency and expected background yields for several Z' masses in the $\mu^+\mu^- + \not{E}_{\mathrm{T}}$ final state with $\not{E}_{\mathrm{T}} > 100$ GeV. In each model, the masses are are chosen to be that of the heavy spectrum case. 48

5.1 Particle mass settings in the simulated mono-Z' samples for a given mediator mass $m_{Z'}$. 61

5.2 Event selection criteria in the mono-W/Z and mono-Z' signal regions with merged and resolved event topologies. The symbols "j" and "J" denote the reconstructed small-R and large-R jets, respectively. The abbreviations HP and LP denote respectively the high- and low-purity signal regions with merged topology, as defined by the cut on the large-R jet substructure variable $D_2^{(\beta=1)}$. 70

5.3 The expected and observed numbers of events for an integrated luminosity of 36.1 fb^{-1} and $\sqrt{s} = 13$ TeV, shown separately in each mono-W/Z signal region category. The background yields and uncertainties are shown after the profile likelihood fit to the data (with $\mu = 0$). The quoted background uncertainties include both the statistical and systematic contributions, while the uncertainty in the signal is statistical only. The uncertainties in the total background can be smaller than those in individual components due to anti-correlations of nuisance parameters. 83

5.4 The expected and observed numbers of events for an integrated luminosity of 36.1 fb^{-1} and $\sqrt{s} = 13$ TeV, shown separately in each mono-Z' signal region category assuming $m_{Z'} = 90$ GeV. The background yields and uncertainties are shown after the profile likelihood fit to the data (with $\mu = 0$). The quoted background uncertainties include both the statistical and systematic contributions, while the uncertainty in the signal is statistical only. The uncertainties in the total background can be smaller than those in individual components due to anti-correlations of nuisance parameters. 88

5.5 The expected and observed numbers of events for an integrated luminosity of 36.1 fb^{-1} and $\sqrt{s} = 13$ TeV, shown separately in each mono-Z' signal region category assuming $m_{Z'} = 350$ GeV. The background yields and uncertainties are shown after the profile likelihood fit to the data (with $\mu = 0$). The quoted background uncertainties include both the statistical and systematic contributions, while the uncertainty in the signal is statistical only. The uncertainties in the total background can be smaller than those in individual components due to anti-correlations of nuisance parameters. 89
5.6 Breakdown of expected signal strength uncertainties for several mono-W/Z and mono-Z' signal models, obtained for an integrated luminosity of 36.1 fb^{-1} and $\sqrt{s} = 13$ TeV. A dark matter mass of 1 GeV is used for the two vector-mediator signals. Each systematic uncertainty contribution is determined from the quadratic difference between the total uncertainty and the uncertainty obtained by neglecting the systematic uncertainty source in question. Only the largest systematic uncertainties are shown. 90
5.7 The observed and expected exclusion limit at 95% CL on σ_{vis} for $W + \text{DM}$ production for an integrated luminosity of 36.1 fb^{-1} and $\sqrt{s} = 13$ TeV, together with the corresponding product of acceptance and efficiency ($A \times \varepsilon$) for different regions of $E_{\text{T}}^{\text{miss}}$. 94
5.8 The observed and expected exclusion limit at 95% CL on σ_{vis} for $Z + \text{DM}$ production for an integrated luminosity of 36.1 fb^{-1} and $\sqrt{s} = 13$ TeV, together with the corresponding product of acceptance and efficiency ($A \times \varepsilon$) for different regions of $E_{\text{T}}^{\text{miss}}$. 94

6.1 Hyperparameter support for Bayesian optimization of deep neural network architectures. For the no-pileup case, networks with a single hidden layer were allowed to have up to 1000 units per layer, in order to remove the possibility of the deep networks performing better simply because they had more tunable parameters. 110
6.2 Hyperparameter support for BDTs trained on 6 high-level features, and the best combinations in 110 and 140 experiments, respectively, for the no-pileup and pileup tasks. Minimum leaf percent was constrained to be one fourth of the minimum split percent in all cases. 110
6.3 Performance results for BDT and deep networks. Shown for each method are both the signal efficiency at background rejection of 10, as well as the Area Under the Curve (AUC), the integral of the background efficiency versus signal efficiency. For the neural networks, we report the mean and standard deviation of three networks trained with different random initializations. . . 110

7.1 Comparison of classification performance using the AUC (Area Under the Curve of signal efficiency versus background efficiency, see Fig 7.2) for various approaches. Statistical uncertainty in each case is ±0.002. 124

ACKNOWLEDGMENTS

I would like to thank the Department of Energy Office of Science for their funding over the course of my graduate career.

Chapter 4 of this dissertation is a reprint of the material as it appears in "Mono-Z': searches for dark matter in events with a resonance and missing transverse energy". Daniel Whiteson directed and supervised this research. Tongyan Lin provided the theoretical expertise and Marcelo Autran aided in the strategy building.

Chapter 5 of this dissertation is a reprint of the material as it appears in "Search for dark matter in events with a hadronically decaying vector boson and missing transverse momentum in pp collisions at $\sqrt{s} = 13$ TeV with the ATLAS detector". I would like to thank the entire ATLAS collaboration for which this work would be impossible. In particular I'd like to thank Sarah Barnes, Jike Wang, Patrick Rieck, Sandra Kortner, Philipp Gadow, Oleg Brandt, Krisztian Peters, Xuanhong Lou, Song-Ming Wang, Koji Terashi, Daniel Whiteson, Dan Guest, and Sam Meehan for their significant contributions to this work.

Chapter 6 of this dissertation is a reprint of the material as it appears in "Jet Substructure Classification in High-Energy Physics with Deep Neural Networks". Daniel Whiteson and Pierre Baldi directed and supervised this research. Peter Sadowski and Clara Eng contributed to the model building and testing.

I would also like to thank my advisor Daniel Whiteson for all of his support during my graduate career. I could not ask for a more creative advisor willing to support me through multiple research directional shifts.

And lastly, thank to everyone else at UCI who has impacted my life, fellow students and professors. There are too many names to list, but your continued support and friendship, no matter how large or small, has meant a lot.

CURRICULUM VITAE

Kevin Thomas Bauer

EDUCATION

Doctor of Philosophy in Physics **2019**
University of California, Irvine *Irvine, CA*

Bachelor of Science in Physics and Mathematics **2014**
Indiana University *Bloomington, IN*

RESEARCH EXPERIENCE

Graduate Research Assistant **2014–2018**
University of California, Irvine *Irvine, CA*

Undergraduate Research Assistant **2011–2014**
Indiana University *Bloomington, IN*

TEACHING EXPERIENCE

Teaching Assistant **2014–2016**
University of California, Irvine *Irvine, CA*

REFEREED JOURNAL PUBLICATIONS

Search for dark matter in events with a hadronically decaying vector boson and missing transverse momentum in pp collisions at $\sqrt{s} = 13$ TeV with the ATLAS detector **2018**
JHEP

Searching for spin-3/2 leptons **2016**
Phys. Rev. D

Jet Substructure Classification in High-Energy Physics with Deep Neural Networks **2016**
Phys. Rev. D

Search in the MET plus V hadronic final state **2016**
Phys. Lett. B

Mono-Z': searches for dark matter in events with a resonance and missing transverse energy **2015**
Phys. Rev. D

A measurement of the energy and timing resolution of GlueX Forward Calorimeter using an electron beam **2013**
NIMA

ABSTRACT OF THE DISSERTATION

Developing New Ideas with ATLAS: Dark Matter Searches, Detector Upgrades, and Phenomenology

By

Kevin Thomas Bauer

Doctor of Philosophy in Physics

University of California, Irvine, 2019

Professor Daniel Whiteson, Chair

This thesis covers a new search for dark matter at the LHC in addition to improved particle identification techniques using neural networks. Models are introduced for a new search at the LHC, mono-Z', where dark matter is produced in association with a new hypothetical boson. Searches are performed using data collected from pp collisions at $\sqrt{s} = 13\ TeV$ using the ATLAS detector. Measurements from this search are consistent with the Standard Model, and upper limits are estimated on the production cross sections and model parameters. Next, we explore techniques for identification of for jets and muons using deep convolutional neural networks trained on calorimeter energy deposits. In both studies, improvements on the baseline techniques using high-level engineered features is observed.

Chapter 1

Introduction

This chapter will briefly summarize modern particle physics and how it relates to the research documented in this thesis. We will begin with a brief history of modern particle physics and the development of the Standard Model and discuss a few of its key shortcomings. Then, we will discuss the phenomena of dark matter, and evidence for its existence. Finally, we will briefly discuss a few candidate theories for dark matter.

1.1 The Standard Model

1.1.1 Historical background

In the early 20th century, physicists were starting to probe the inner workings of the atom and beginning to understand the fundamental laws that governed nature at this scale. By the 1930s physicists knew the atom was made up of a nucleus, containing protons and neutrons, and electrons bound to the nucleus in shells. These particles were studied and quantum mechanics was developed to explain their interactions.

Later, by the 1960s, particle accelerators were rapidly increasing in complexity and power and along with cosmic ray experiments had discovered dozens of new particles with distinct properties. They were classified as baryons (protons, neutrons, and other similar particles), mesons (e.g. pions), quarks (subatomic building blocks of baryons and mesons), and leptons (electrons, neutrinos, and other similar particles). This became known as the "particle zoo" and physicists were struggling to piece together a fundamental theory of all of these particles and interactions.

1.1.2 Overview

The Standard Model is a theory developed to describe the interactions of all known particles. The Standard Model describes three out of four known forces in the universe (electromagnetic, strong and weak forces) and predicts all matter is built from just 17 "elementary" particles.

The elementary particles consist of matter particles, quarks and leptons, and carrier particles known as bosons. There are 6 quarks that come in 3 different colours. The quarks combine to form colourless composite particles like baryons and mesons and are never found in isolation. There are 6 leptons consisting of three generations. The electron and electron neutrino, the muon and muon neutrino, and the tau and tau neutrino. The electron, muon, and taus carry electric charge and mass, whereas the neutrinos are electrically neutral and consist of very little mass.

The rest of the elementary particles consist of a family of particles called bosons which carry the fundamental forces. The strong and weak forces, are atomic short range forces within the nucleus. The strong force is mediated by the gluons, whereas the weak force is mediated by the W and Z bosons. The electromagnetic force is mediated by the photon.

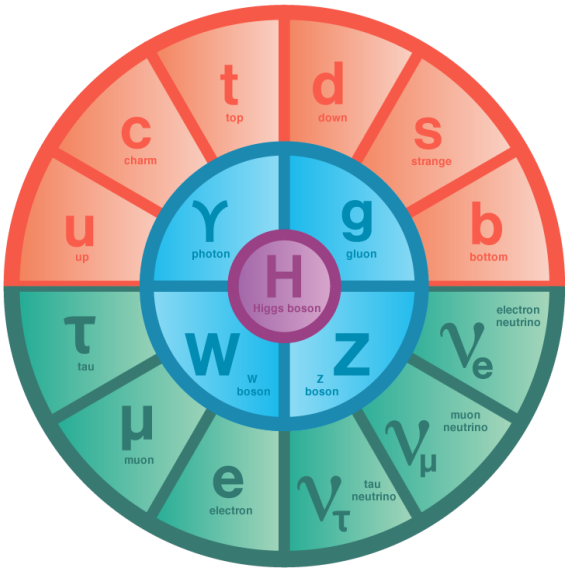

Figure 1.1: Overview of the elementary particles of the Standard Model [1]

The last of the elementary particles predicted by the Standard Model is the Higgs Boson. The Higgs Boson is a prediction from the the Higgs Mechanism introduced to explain the mass of the bosons. This rare, heavy, and elusive particle was the last of the elementary particles discovered in 2012, completing the Standard Model.

An overview of these particles is shown in Fig. 1.1.

1.1.3 Incompleteness of the Standard Model

While all fundamental predictions made by the Standard Model have been consistent with experimental findings, it is not fully comprehensive.

While the Standard Model predicts three of the four known forces, it does not account for gravity. While there are many models beyond the Standard Model accounting for gravity, being many orders of magnitude weaker than all of the other known forces this force has so far eluded experimental predictions.

Another phenomena that is not accounted by the Standard Model is dark matter, a core subject of this thesis and will be discussed at length in the next section. Most of what we know about dark matter is from astronomical observations. Dark matter interacts gravitationally, and either does not interact electromagnetically or interacts only very weakly. Dark matter is also stable and accounts for approximately 85% of the known matter in the universe.

1.2 Dark Matter

1.2.1 Evidence

Evidence of dark matter exists primarily from astronomical and cosmological observations. This subsection will introduce a few of the core pieces of evidence and provide resources for further study.

Galactic Rotation Curves

Perhaps the most clear evidence of dark matter in the universe comes from the rotations of galaxies.

Spiral galaxies are observed to rotate around its center and the amount and distribution of a galaxy's luminous matter is measured. Since a galaxy's mass is concentrated at the center, we can model a galaxy as a large point mass in the center and predict the velocity of the outer bands using Kepler's Second Law. It is expected that the velocity of the outer bands decrease the farther from the center of the galaxy. However, observations show that the velocity remains relatively constant [2] as shown in Fig. 1.2. One way to rectify this discrepancy is the existence of non-luminous dark matter in the outer reaches of galaxies in a surrounding halo.

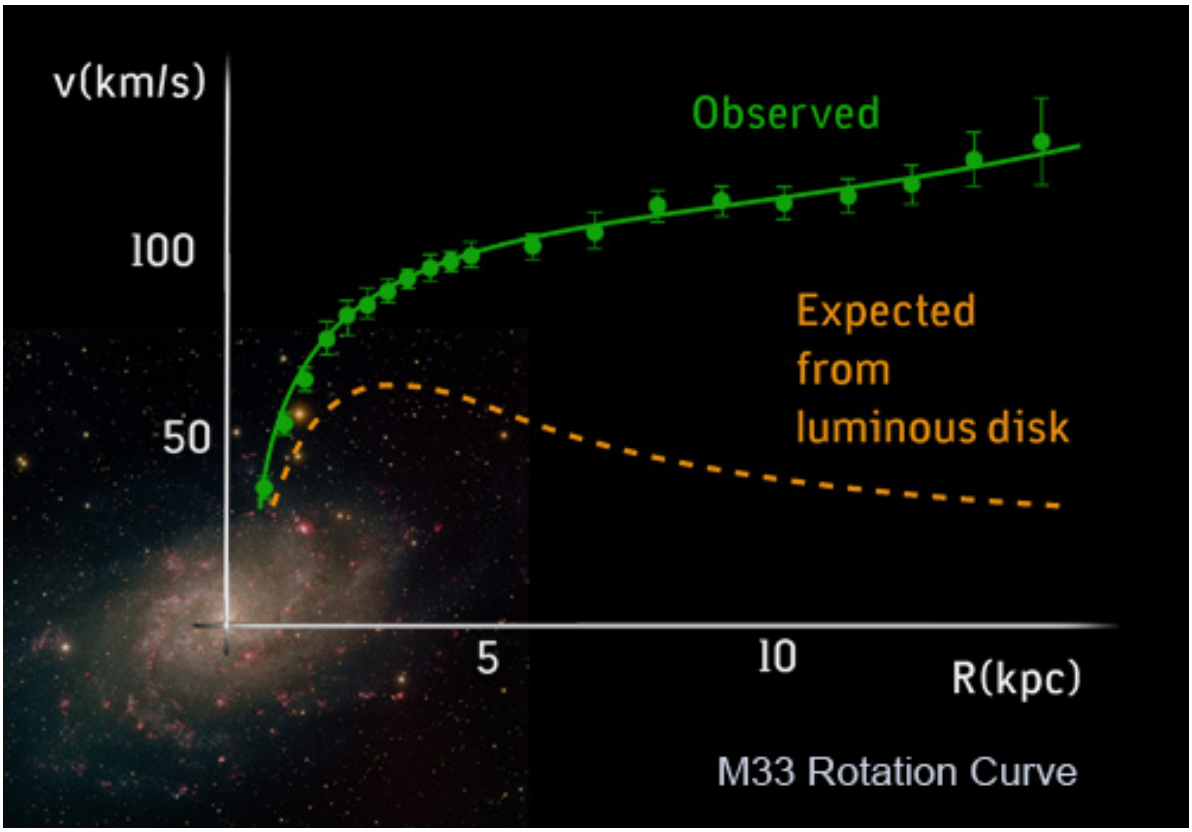

Figure 1.2: A comparison of the expected vs observed velocity as a function of distance from the center for an example galaxy [3]

The Bullet Cluster

Another important observation providing evidence for the existence of dark matter is from the Bullet Cluster, a galaxy cluster that is the by-product of a recent (on galactic time-scales) collision. Gravitational lensing mapped the center of mass of the total matter of the colliding galaxies and found an offset from the location of the luminous matter observed from x-rays from the colliding gas [4]. The evidence from the Bullet Cluster suggests that dark matter in the individual galaxies passed through unaffected (as predicted) and caused the offset between the total center of mass and the luminous mass.

Cosmic Microwave Background

The Cosmic Microwave Background (CMB) is more evidence for the existence of dark matter. The CMB is a nearly perfect blackbody, but contains small temperature fluctuations of about 1 part in 100,000. These temperature anisotropies have been extensively mapped and studied most precisely by the Planck spacecraft. Their findings are consistent with large amounts of dark matter and give the most precise measurements of the dark matter density [5].

1.2.2 Dark Matter Candidate Theories

For a candidate theory of dark matter a postulated particle must be stable, interact very weakly or not at all with electromagnetic radiation, and must have the correct relic dark matter density as measured by Planck. This subsection will introduce a few candidate theories and provide resources for further study.

Weakly Interacting Massive Particle

One such intriguing dark matter candidate is a Weakly Interacting Massive Particle (WIMP) [6]. WIMPs are predicted in many Beyond Standard Model (BSM) theories. WIMPs main characteristics are that they only interact via the weak nuclear force and gravity, and are massive. Many dark matter models tested at the LHC contain dark matter WIMPs and will be covered more extensively in later chapters of this thesis.

Primordial Black Holes

One might wonder if dark matter necessarily must be a particle at all. It is possible that the discrepancy for the galactic rotation curves is accounted for black holes present in the

outer reaches of galaxies and left over from the big bang. While not being a new idea, the possibility of primordial black holes is still an active area of research [7].

Axions

Axions, postulated to solve the Strong CP problem in Quantum Chromodynamics, are another class of hypothetical particles which are dark matter candidates [8]. Axions are predicted to have no electric charge, a very small mass, and very weakly interacting. This topic is an area of extensive active research but is not the focus of this thesis.

Sterile Neutrinos

Sterile neutrinos have also been postulated as a dark matter candidate [9]. Sterile neutrinos only interact via the gravitational force. Detection could be made through mixing between active and sterile neutrinos and is another area of active research in particular with the MiniBooNE experiment [10].

Chapter 2

The Large Hadron Collider (LHC) and the ATLAS Detector

This chapter will briefly introduce the Large Hadron Collider (LHC) as well as the ATLAS detector. Without the successful design, completion, operation, and maintenance this thesis would not be possible.

2.1 The LHC

The Large Hadron Collider (LHC) is a two-ring-superconducting-hadron accelerator and collider built in a tunnel underground Switzerland and France, nearby the city of Geneva and previously used to house the older Large Electron-Positron Collider (LEP). Built by the European Organization for Nuclear Research (CERN) between 1998 and 2008, the LHC is 26.7 kilometers in circumference and is the world's most powerful particle collider.

The LHC consists of two parallel beamlines each containing accelerated hadrons traveling in opposite directions. Roughly 10000 superconducting magnets are used to focus and target

the paths of the hadrons. The beams intersect at four points where detectors are housed to record the collisions [11].

Since its successful completion, the LHC has been recording data since 2010. The focus of this thesis will be on data collected since 2015, when the LHC began operating at near-peak collision center of mass energy of $\sqrt{s} = 13\ TeV$ and a collision rate of approximately 40 MHz.

2.2 ATLAS

Just underground the entrance main entrance to CERN in Meyrin, Switzerland at one of the four beam crossing points houses the ATLAS (A Toroidal LHC ApparatuS) detector. ATLAS is 25 meters in height, 44 meters in length, and weighs approximately 7000 tonnes [12]. ATLAS is itself made up of several subdetectors, each will be summarized in this chapter. In total there are seven particle detectors placed at the four intersection points of the LHC, where ATLAS, along with CMS (Compact Muon Solenoid), is designed as a general purpose detector aiming to probe proton-proton collisions for any signs of new physics beyond the Standard Model. This thesis will only cover the ATLAS detector where the entirety of the data used in this research originates.

There are four main sections of the ATLAS detector with the objective to identify and measure particles coming from the proton collisions of the LHC.

The inner tracker consists of a pixel detector, silicon microstrip tracker, and a transition radiation tracker. The purpose of the inner tracker is to measure the direction, momentum, and charge of charged particles.

Next are the calorimeters which are designed to absorb particles coming from the inner tracker and measure energy depositions. There are two calorimeters, the electromagnetic

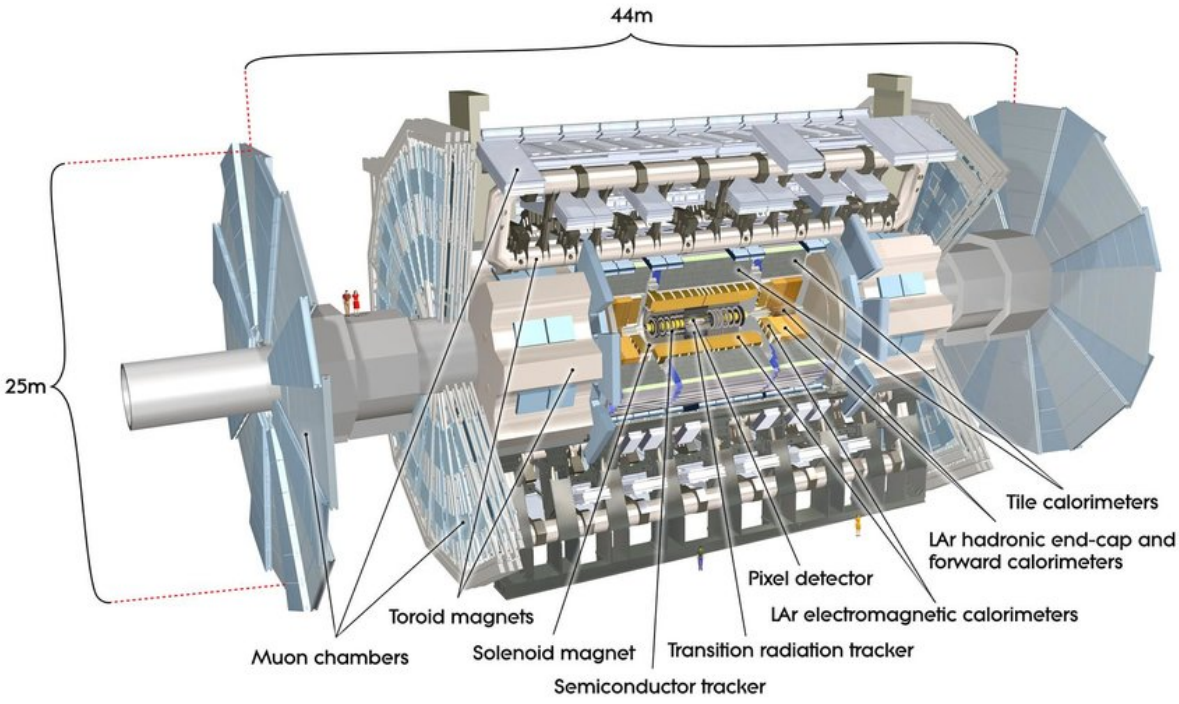

Figure 2.1: A schematic of the ATLAS detector and its subdetectors. The LHC beam runs horizontal in this image [12]

calorimeter designed to absorb photons and electrons, and the hadronic calorimeter designed to absorb hadrons. The electromagnetic calorimeter works with Liquid Argon, while the hadronic calorimeter consists of over 500,000 scintillator tiles [12].

Finally, the last layer of the ATLAS detector is the muon spectrometer, designed to identify and measure the momenta of muons, particles which are minimum ionizing and pass through the rest of ATLAS largely undetected.

2.2.1 The ATLAS Coordinate System

In this subsection, the coordinate system used to track particles measured by the ATLAS detector is summarized in this section, as the definitions are used extensively throughout the

rest of this thesis.

A schematic of the ATLAS detector is shown in Fig. 2.1.

The collision point of the protons is defined as the origin of the ATLAS coordinate system. The beam direction defines the z-axis and the $x - y$ plane is transverse to the beam. The azimuthal angle ϕ is measured around the beam axis, and the polar angle θ is measured as the angle from the beam axis. In this thesis, we use the polar angle to define pseudorapidity as:

$$\eta := -\ln\left[\tan\left(\theta/2\right)\right]$$

Pseudorapidity is defined in the range $(-\infty,\infty)$, where 0 is perpendicular to the beam line and ∞ is along the beam line.

The distance metric, ΔR is defined as:

$$\Delta R := \sqrt{\Delta\eta^2 + \Delta\phi^2}$$

From these definitions, we calculate the transverse momentum p_{T}, transverse energy E_{T}, and the missing transverse energy $E_{\mathrm{T}}^{\mathrm{miss}}$ all of which are defined in the $x - y$ plane and will be used extensively in this thesis.

2.2.2 The Inner Detector

The inner detector lies within a 2 T solenoidal magnetic field along the beam axis and is shown in Fig. 2.2. With this detector pattern recognition, momentum and interaction vertex measurements, and particle identification are achieved [12].

High precision measurements must be made with the inner detector in order to track the momentums and vertex of thousands of particles originating from the interaction point at

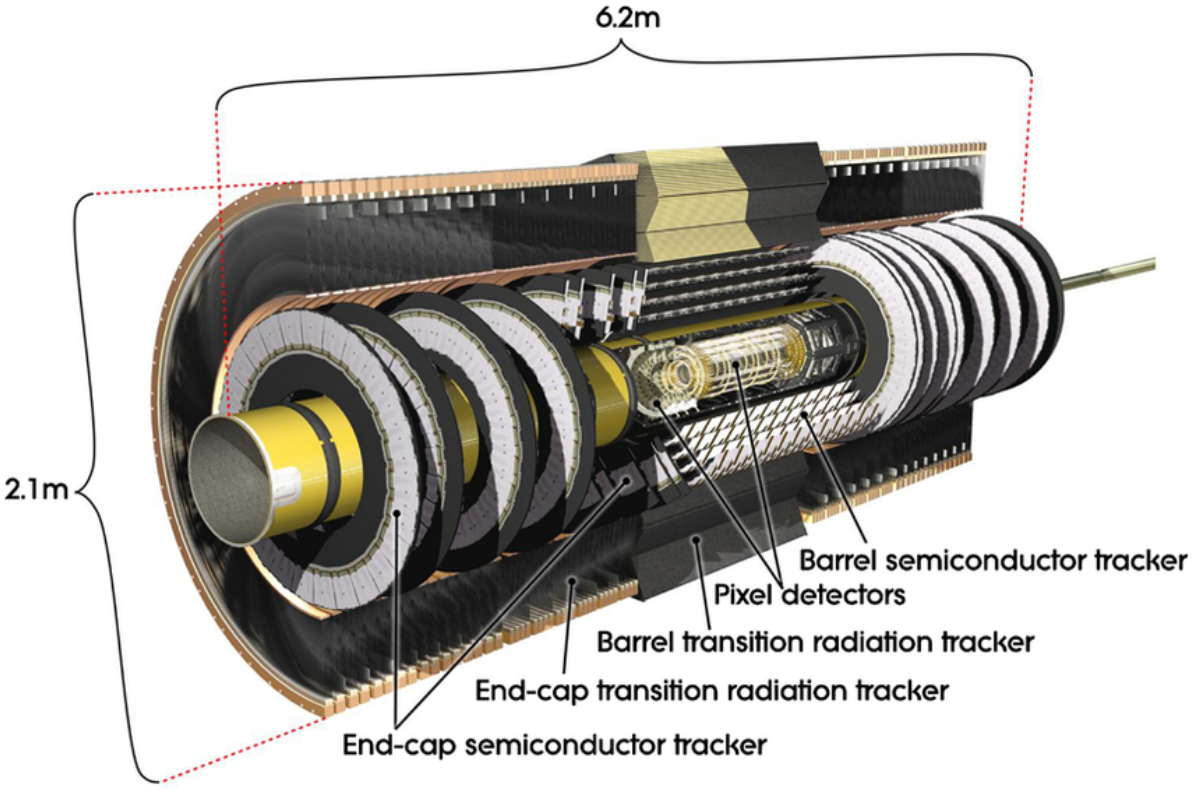

Figure 2.2: A schematic of the ATLAS inner detector for tracking charged particles from the collision point [12]

rates up to 40 MHz [12].

The inner detector itself is made up of three main layers, the Pixel Detector, the Silicon Microstrip Trackers (SCT) and the Transition Radiation Tracker (TRT).

The Pixel Detector

The Pixel Detector is the innermost module of the inner tracker and consists of approximately 80 million pixels over a total area of $1.7m^2$. This high granularity provides high precision tracking for charged particles within $|\eta| < 2.5$. In total there are six Pixel disks (three in each endcap) and three Pixel layers within the barrel.

Within the barrel, the Pixel Detector measurement accuracy of $R - \phi$ is approximately 10 μ

m and 115μ m for z. In the disks the accuracy in $R-\phi$ is approximately 10 μ m and 115μ m for R [12].

The Silicon Microstrip Trackers (SCT)

The next layer within the Inner Detector is the SCT. In the SCT, 60 m^2 of silicon is used over 4 layers within the barrel and 18 endcap disks, read out by approximately 6.3 million channels.

Eight strip layers are crossed by each track. Within the barrel, stereo strips measure $R-\phi$ with one set parallel to the beam. In the end caps, the SCT consists of strips running radially from the beam line as well as strips at an angle of 40 mrad.

Within the end-caps, the SCT measurement accuracy of $R-\phi$ is approximately 17 μ m and 580μ m for z. In the disks the accuracy in $R-\phi$ is approximately 17 μ m and 580μ m for R [12].

The Transition Radiation Tracker (TRT)

The outermost subsection of the Inner Detector is the Transition Radiation Tracker (TRT). The TRT consists of straw tubes, 4mm in diameter filled with Xenon and containing a 0.03mm in diameter gold-plated tungsten wire in the center. The TRT can only measure $R-\phi$ where it does so with an accuracy of 130μm per straw. Data from each straw is read out in a separate channel.

Approximately 50,000 straws are contained in the barrel region, where the straws are parallel to the beam axis and 144 cm long.

The TRT region of the end-caps contain approximately 250,000 straws. These end-cap straws

are 37 cm long and are arranged radially [12].

2.2.3 The Calorimeters

Just outside of the Inner Detector rests the calorimeters, covering a range of $|\eta < 4.9$. The closest calorimeter to the beam is the EM calorimeter (ECAL), optimized to stop and measure the energy deposits of electrons and photons. Outside of this calorimeter is the Hadronic calorimeter (HCAL) designed to stop and measure the energy deposition of hadrons.

The ECAL is 53 cm thick while the HCAL is 197 cm. The thickness was chosen in order to contain most of the electromagnetic and hadronic showers, and also to limit the chances of these particles punching-through to the muon detector. The layout of the calorimeter system within the ATLAS detector is shown in Fig. 2.3 [12].

The Electromagnetic Calorimeter (ECAL)

The ECAL is a lead-liquid Argon detector divided into a barrel section ($|\eta| < 1.475$) and two end cap sections ($1.375 < |\eta| < 3.2$). The barrel is made up of two identical half-barrels each of length 3.2m and resulting in a 4mm gap at $z = 0$. Each half-barrel weighs 57 tonnes. 1024 accordion-patterned absorbers and electrodes make up each half-barrel. This geometry ensures full coverage of η without gaps.

The ECAL end-caps are made up of two wheels, each 63cm thick and weighing 27 tonnes. The ECAL is divided into three layers of depth. The first two layers are read out in cells of granularity $\Delta\eta \times \Delta\phi = 0.025 \times 0.025$. The outermost layer has a granularity that is twice coarser in η [12].

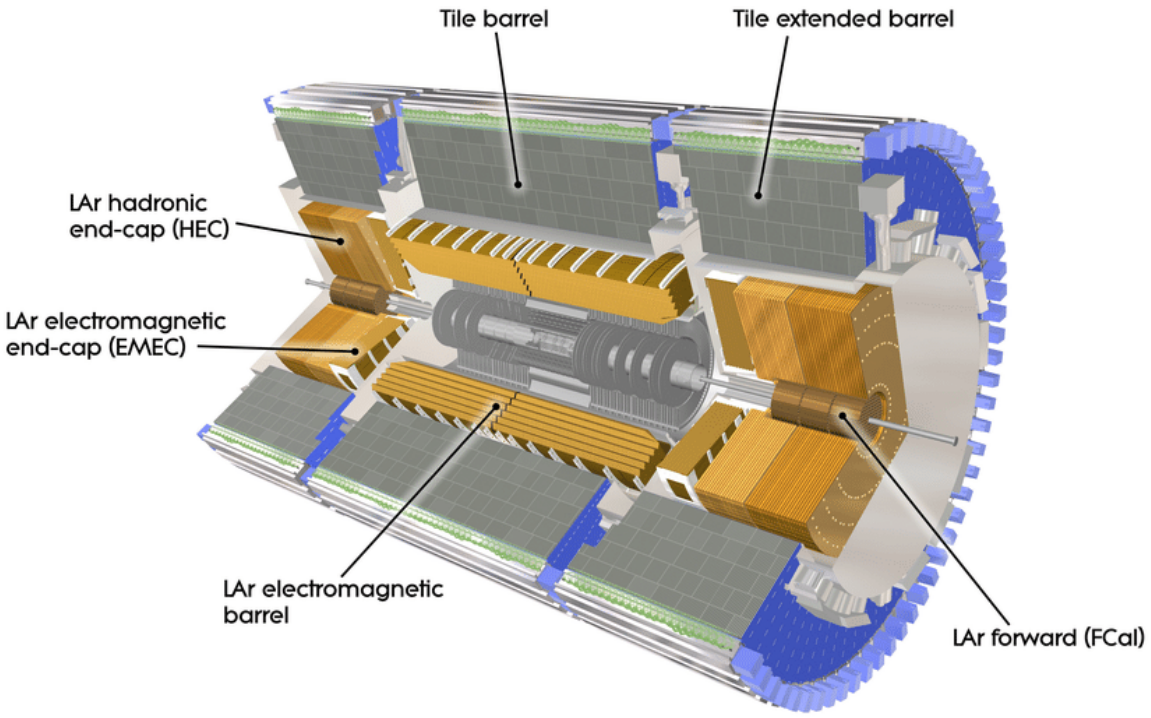

Figure 2.3: A schematic of the ATLAS calorimeter system for stopping and measuring the properties of photons, electrons, and hadrons [12]

The Hadronic Calorimeter (HCAL)

Directly beyond the ECAL is the HCAL. The HCAL is a sampling calorimeter with steel plate absorbers and scintillators. The HCAL is divided into three subsections, a 5.8m long barrel, and two other barrels of length 2.6m each. The central barrel weighs 20,000 kg and the two extended barrels weigh 9,600 kg each. In total 500,000 scintillator tiles make up the HCAL. Each barrel is made up of 64 modules of size $\Delta\eta$ 0.1.

In total the full region $|\eta| < 3.2$ is covered by the HCAL system. The scintillator tiles are oriented radially and are perpendicular to the beam. Light produced by the scintillator material is read out by photomultiplier tubes (PMTs) connected to wavelength-shifting fibers at the edges of the tiles. The HCAL is read out in cells of $\Delta\eta \times \Delta\phi = 0.01 \times 0.01$ in the first

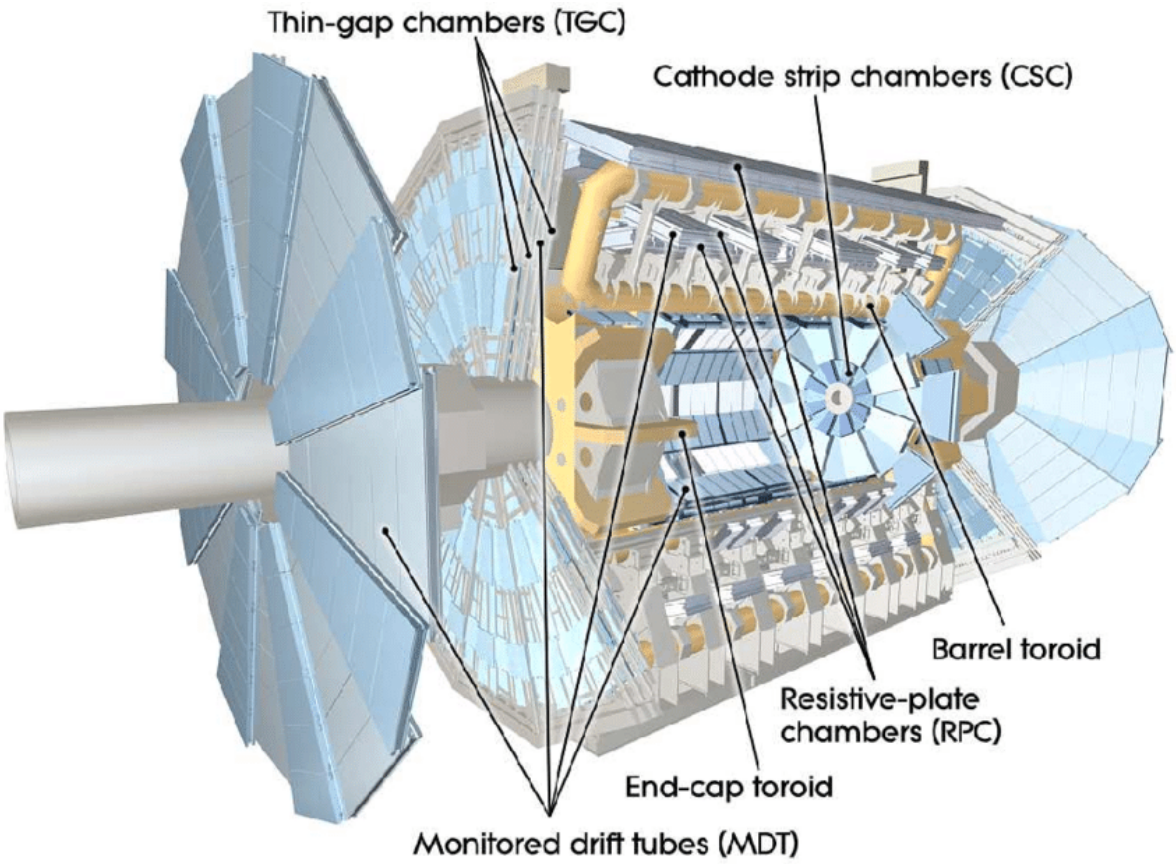

Figure 2.4: A schematic of the ATLAS Muon Spectrometer system for identifying and measuring the momentum of muons [12]

two layers and $\Delta\eta \times \Delta\phi = 0.02 \times 0.01$ in the last layer [12].

2.2.4 The Muon Spectrometer (MS)

The last subdetector we will cover in this thesis is the outermost Muon Spectrometer (MS) shown as a schematic Fig. 2.4. Since muons are minimum ionizing particles, they are the only charged particles which consistently escape the calorimeters. It is the purpose of the MS to identify these muons and measure their momentum. The MS measures a track made by a muon and subsequently can be compared to tracks in the Inner Detector to provide a precise measurement of a muon's momentum.

Muons are bent in the MS by a magnetic field generated by three large air-core toroids. Each toroid consists of eight coils which are radial and symmetric about the beam.

The muon tracks are measured by Monitored Drift Tubes (MDT's) and Cathode Strip Chambers (CDC's). Each of the approximately 350,000 MDT's are 3 cm in diameter and 0.85-6.5 m long. The resolution of the MDT's is 80μm. The CDC's are used in the innermost plane $2.0 < |\eta| < 2.7$, due to the higher rates and background conditions. In total there are 70,000 readout channels for the CDS's and they have a resolution of 60 μm.

For high-frequency triggering, the MS utilizes Thin Gap Chambers (TGC's) and Resistive Plate Chambers (RPC's). In addition these systems provide information for muon's non-bending direction. The TGC's are read out by approximately 440,000 channels at the end caps of the detector, while the RPC's are used in the central region and read out using approximately 380,000 channels [12].

2.2.5 Reconstruction of Physics Objects in ATLAS

ATLAS can detect any Standard Model particle that interacts via the electromagnetic force or the strong force. Neutrinos pass through ATLAS fully undetected. The major physics objects which are used in this thesis and throughout ATLAS are muons, electrons, photons, jets (cones of hadrons originating from the fragmentation and hadronization of a quark or gluon) and $E_{\mathrm{T}}^{\mathrm{miss}}$ ("missing transverse energy" is the vector sum of energy needed to satisfy conservation of momentum for all reconstructed physics objects).

A schematic cross-section of ATLAS subdetector layers is shown in Fig. 2.5 along with examples of identifiable particles within ATLAS and how they interact with each detector and system as a whole.

The reconstruction process for each of these objects will be summarized in this subsection

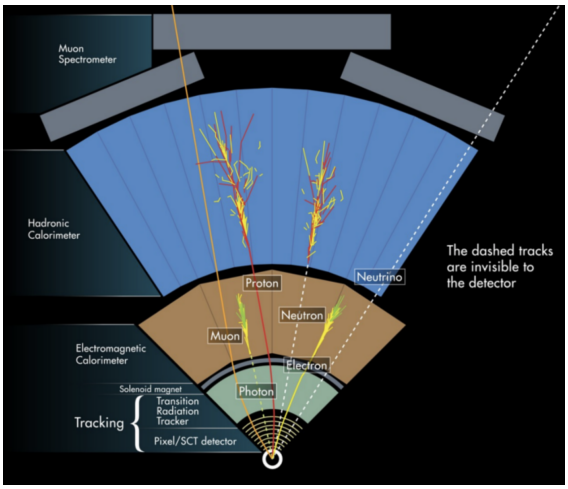

Figure 2.5: A cross-section schematic of the ATLAS detector and how particles interact with the system [13]

and references for further reading provided.

Muons

As muons are minimum ionizing particles, they primarily pass through the detector only making a single track, bent by the magnetic field. Muons are reconstructed using information combined by both the specialized Muon Spectrometer and the Inner Detector. Tracks are independently reconstructed in both systems and extrapolated to the full system.

A global fit is performed using tracks in both the MS and the ID and a combined track is accepted as a muon if it passes quality of fit criteria. In addition, a candidate muon's isolation is measured as the sum of hadronic energy within a cone of the candidate. A cut on the isolation of muons is applied to minimize this hadronic activity to remove background from non-isolated muons within the decay chains of b or c quarks [14]. This topic will be covered more extensively in Chapter 7 of this thesis.

Electrons and Photons

Both electrons and photons induce an "electromagnetic shower" within the using electron-positron creation by the photons and bremsstrahlung radiation of photons by the energetic electrons. Therefore, incident electrons and photons look nearly identical in the ECAL and thus have very similar reconstruction techniques. One major difference, however, is the addition of a charged track in the Inner Detector for electron candidates, but not for photon candidates (as they are uncharged).

In electron-photon reconstruction, the ECAL is divided into a grid of "towers" of size $\Delta\eta \times \Delta\phi = 0.025 \times 0.025$. The energy of each of the three layers of the ECAL as well as the presampler is summed. Electron-photon candidates are then seeded from energy deposits using a sliding-window algorithm of 3×5 towers in the plane which exceed 2.5 GeV. Duplicates are removed by selecting the highest E_{T} candidate in close proximity [15].

Electron candidate tracks are reconstructed using the Gaussian-sum filter (GSF) method which is designed to better account for energy loss of charged particles. The electron candidate tracks are then matched to the electron-photon candidate calorimeter deposit. A candidate is determined to match if $-0.10 < q \times [\Delta(\phi_{cluster}, \phi_{track})] < 0.05$, where q is the electric charge. A track which passes this condition is primarily considered an electron candidate, however, if the track can be matched to a secondary vertex and has no Pixel Detector hits then it is a photon candidate (likely from photon conversion) [15].

Furthermore, several other criteria and selection cuts (including isolation as is applied also to muons and described in the previous subsection) regarding electron-photon identification are applied and described in reference [15].

Jets

Unlike the other objects discussed earlier in this subsection, jets are not individual particles themselves, but rather narrow cones of many hadrons produced through fragmentation and hadronization of a quark or gluon. Quark products in the proton collisions cannot exist alone because QCD confinement only allows for colorless states, and quarks carry color charge. Therefore, as a quark fragments, it quickly creates new quarks and gluons in order to form colorless states. The result is a shower of new particles which then form the cone hadrons represented as a jet object.

Jets are reconstructed in ATLAS experiments using topo-clusters (topologically connected calorimeter cells) as inputs to the anti-k_t jet clustering algorithm [16]. A radius parameter is also included in the clustering algorithm to define the width of the jet cone. In this thesis, a radius parameter of $R = 0.4$ is used to define "small-R" jets and $R = 1.0$ defines "large-R" jets.

Jets are calibrated to the hadronic scale. The effects of pileup, additional in-time proton-proton collisions other than the primary, is subtracted from the jet transverse momentum by a factor proportional to the jet area. The direction of the jet is also corrected to the primary collision vertex [16].

Missing Transverse Energy

As the protons in a particle collision are traveling in approximately head on collisions, we know that the vector sum of all particles in the direction transverse to the beam line must be zero. Therefore, $E_{\mathrm{T}}^{\mathrm{miss}}$ exploits this law and allows us to measure the vector sum of momentum for all invisible particles (e.g. neutrinos).

$E_{\mathrm{T}}^{\mathrm{miss}}$ is calculated independently for the two axis x and y in the transverse plane, and is

defined as the negative vector sum of all the reconstructed visible objects. In the occurrence of overlapping objects, only one is used in order to avoid double counting (e.g. in the case of an overlapping muon and a jet, only the jet is included in the calculation of the $E_{\mathrm{T}}^{\mathrm{miss}}$ [17].

2.2.6 Dark Matter Research Using ATLAS

A limitation of a particle detector like ATLAS is that it is only able to identify and detect particles which interact via the electromagnetic force or the strong force. Dark matter, being only known to interact gravitationally or possibly weakly, if produced during LHC collisions will pass straight through the entire detector unnoticed. Neutrinos when produced will similarly pass through the detector unnoticed.

In order to search for dark matter with ATLAS we must look for signatures where dark matter is produced in association with another, detectable, particle. These events are likely to be reconstructed with large $E_{\mathrm{T}}^{\mathrm{miss}}$ and then we can infer that there must be an invisible particle (likely neutrinos or dark matter) traveling in the other direction. An example event of this process is shown in Fig. 2.6.

Since neutrinos are also unable to interact with the detector, we are unable to distinguish them from dark matter. However, the rate of neutrinos we are to observe can be predicted by the Standard Model. Therefore, to look for dark matter we count how many of these events with MET we see in data and compare to the number of events we predict using just Standard Model neutrinos.

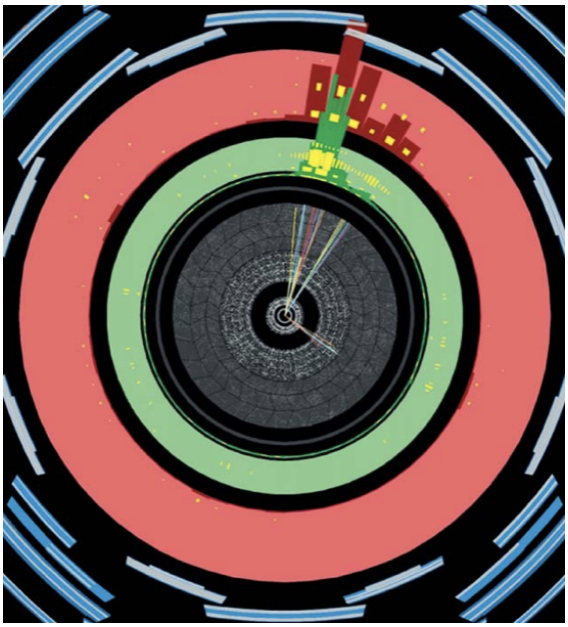

Figure 2.6: An example mono-jet event where an invisible particle(s) is traveling opposite to an energetic jet [18]

Chapter 3

FELIX: the new detector readout system for the ATLAS experiment

3.1 Introduction

During operation, the LHC collides bunches of protons at peak rates of 40MHz. Only a small fraction of this data is important for further study and permanently stored. It is the function of the Trigger and Data Acquisition system (TDAQ) to identify this data and forward to the storage systems.

TDAQ consists of multiple levels. First is the Level 1 trigger system which reduces the 40MHz collision rate to approximately 100kHz. Accepted event fragments are forwarded from the on-detector Front-End (FE) electronics to the back end electronics (RODs) located in a separate service cavern. The RODs push data to the ReadOut System PCs (ROS) which handle data buffering. ROS PCs send accepted event fragments to the High Level Trigger (HLT) computer farm which runs physics algorithms and reduces the rate to approximately 1.5kHz. An overview of the current TDAQ is shown in Fig. 3.1.

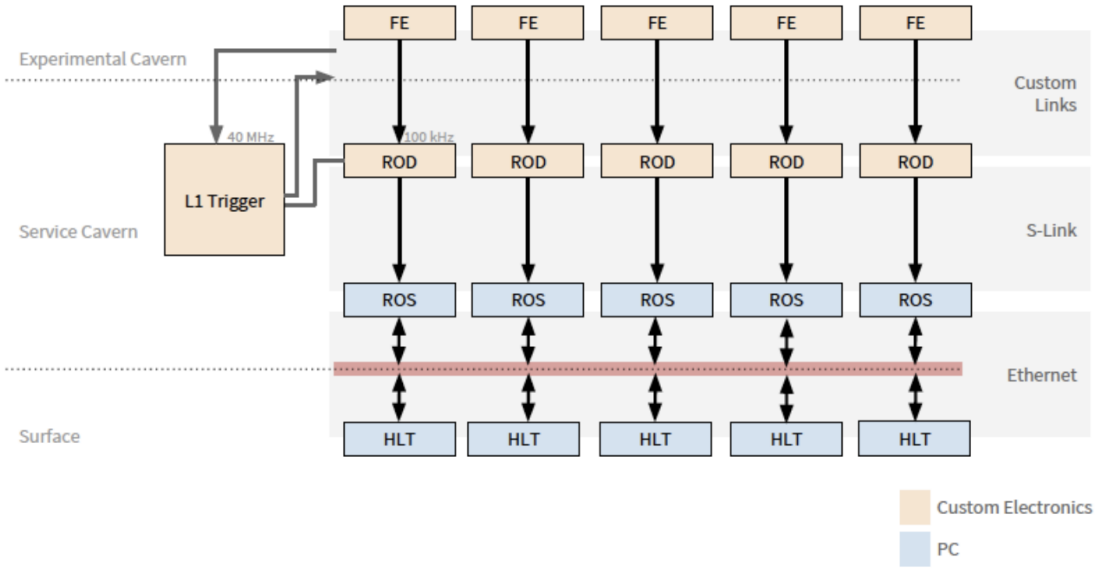

Figure 3.1: Current TDAQ System [21].

The LHC is currently shut down until 2021 and ATLAS will upgrade the Liquid Argon (LAr) Calorimeter trigger electronics, New Small Wheel (NSW) muon detector, and Level-1 calorimeter trigger. For these new systems, the ROD functionality can be replaced by Commercial Off-The Shelf (COTS) PCs. In addition, new GigaBit Transceiver (GBT) [19] links will provide data transfer from the new detector FE electronics to the rest of TDAQ. These new GBT links will support bi-directional traffic and provide commonality among the detectors. Distinct paths for data acquisition (DAQ), Detector Control System (DCS), and trigger timing and control (TTC) will be provided using E-links (a feature of the GBT) to separate traffic. An overview of future changes to TDAQ is shown in Fig 3.2.

The Front-End LInk eXchange (FELIX) will serve the new GBT links in a scalable and detector agnostic way. FELIX functions as a routing device for the bi-directional data and commands from the GBT to and from a commodity network. The network will connect to the rest of the TDAQ system for event readout, detector control, calibration, and configuration.

FELIX is beginning installation to service the new LAr and NSW detectors starting in the

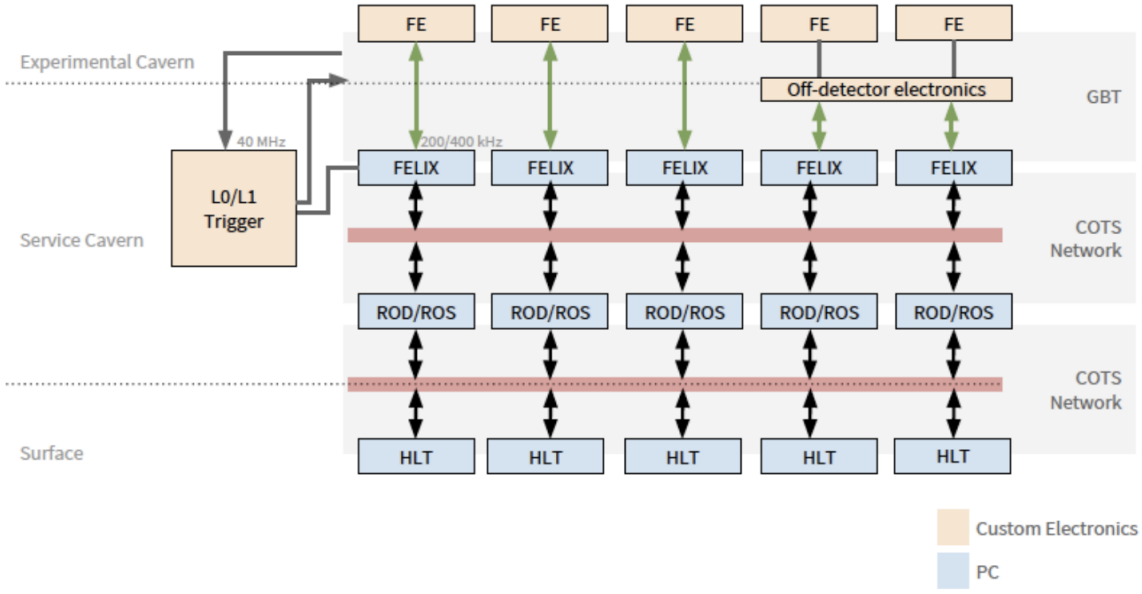

Figure 3.2: Planned TDAQ System by 2024. Some systems will be upgraded to FELIX in 2019 [21].

shutdown. During the subsequent LHC shutdown beginning approximately 2024, FELIX will be installed for all the rest of ATLAS detectors.

3.2 FELIX as a System

FELIX consists of a host PC running a Linux based OS, a Network Interface Card (NIC), and up to two Field Programmable Gate Array (FPGA) based PCIe cards (a.k.a. FLX Card). The FLX Card is responsible to handle the GBT link inputs and to transfer data packets both to and from the host PC. Direct Memory Access (DMA) engines are implemented in the FPGA and the throughput was measured up to 101.7 Gb/s. In addition, the FLX Card handles the TTC and DCS information and forwards to the front ends on separate paths.

A software application processes the data packets and sends them over the network to the swRODs. In the opposite direction, FELIX can receive commands from the network and

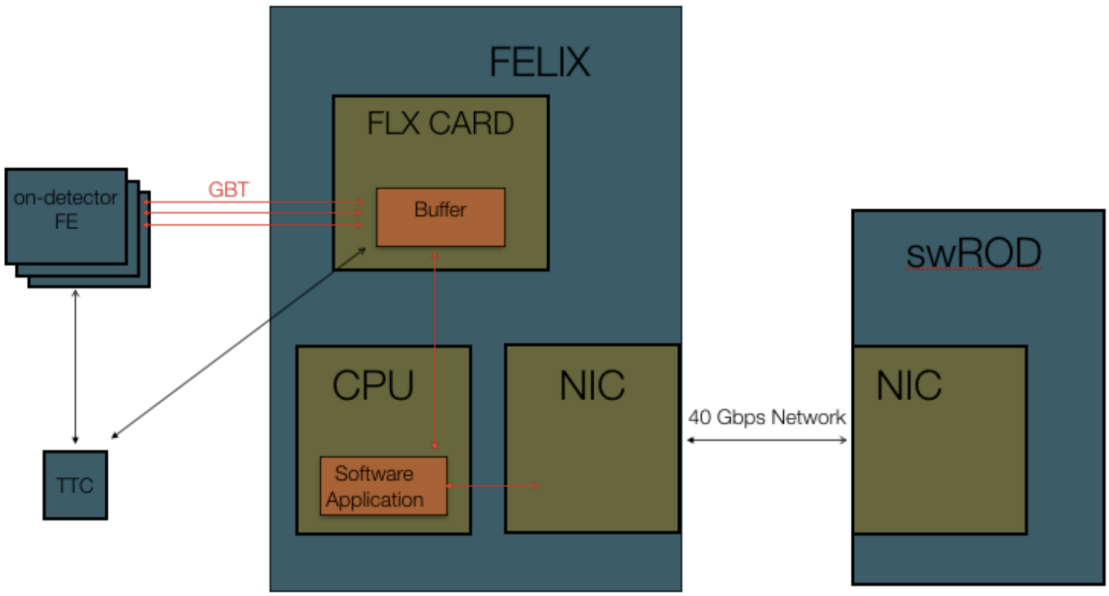

Figure 3.3: Overview of the FELIX system. FELIX consists of a PCIe card (FLX Card), a PC running a software application, and a Network Interface Card (NIC).

forward to the FE via the FLX Card. A diagram of this system is shown in Fig 3.3

3.3 FELIX Hardware Prototype

A prototype FLX Card (FLX-711) has been developed. The main component is a 16-lane Gen3 PCIe board. The FPGA on the board is a Xilinx Kintex UltraScale XCKU115FLVF1924. The FLX-711 supports up to 48 optical bi-directional links with 8 MiniPODs. These links reach a maximum speed of 14 Gb/s. An ADN2814 is used for the TTC clock and data.

The FLX-711 board is shown in Fig. 3.4. Direct Memory Access (DMA) engines are implemented in the FPGA to test the throughput, which was measured to be up to 101.7 Gb/s.

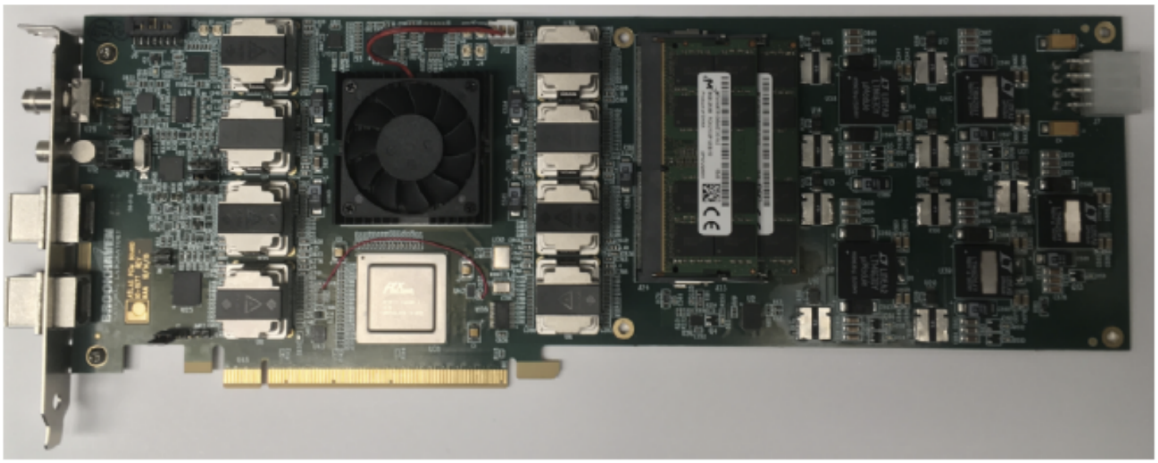

Figure 3.4: The FLX-711 Card [20]

3.4 FELIX Software and Data Transfer

A C++ application (FELIX Core) has been developed to run on the FELIX host PC. FELIX Core's main function is to process data packets to and from the FLX Card and the network. FELIX Core supports both high-throughput and low-latency channels. The high-throughput channel is designed for processing data packets from the FE in real-time, whereas the low-latency channel is provided for the detector control and configuration.

The FLX Card encodes variable-length data packets into 1kByte (blocks) in the DMA buffer. FELIX Core communicates with the DMA buffer and processes the data with multi-threads separated by subsets of E-link IDs. The 1kB blocks are decoded in the software and checked for errors.

A publish and subscribe system has been implemented in FELIX Core for sending and receiving data packets to and from the network. Data from the FEs can be published to the network with distinct tags for the E-link IDs. The downstream swROD PCs then subscribe on the network to specific data types. Additionally, FELIX Core supports subscribing to low-latency channels sending commands to the FEs.

Features have been implemented in the FELIX software for the purpose of testing the system. A test suite has been developed to test key features of the FLX Card firmware for continuous testing of new releases. In addition an internal software data generator was developed for testing the FELIX software and network independently of the FLX Card.

Performance benchmarking has been performed for the FELIX software and network. See reference [21] for a detailed description.

3.5 Conclusions

FELIX is a PC-based system designed to transfer to and from the detector FE electronics and a network connected to the rest of the ATLAS TDAQ system. This system introduces COTS PCs and network earlier in the detector readout system, allowing for the system to be scalable and detector agnostic.

FELIX plans to be operating with ATLAS subsystems by 2024. FELIX is progressing well in integrating with the swRODs and other systems. All major firmware is available, and core software has been developed and performance benchmarks reached. A prototype has been developed and is being tested.

Chapter 4

Mono Z' Phenomenology

4.1 Introduction

A central area of focus at the LHC is the search for physics beyond the standard model (SM). While the LHC will have sensitivity to many models inspired by theoretical extensions or generalizations of the SM, the search for dark matter is of particular interest due to the well-established fact of its existence [22]. The collider detection of dark matter is a cornerstone of the effort to elucidate and obtain evidence for the particle nature of dark matter, and is complementary to astrophysical methods of detection.

Searches for dark matter production at the LHC rely on the production of a visible object X recoiling against the missing transverse momentum ($\not{E}_{\mathrm{T}}$) from the invisible dark matter particles. Cases where X is a SM particle such as g/q [23, 24, 25, 26, 27, 28], W [29, 30, 31, 32], Z [33, 34], H [35, 36], γ [24, 37, 38], or a heavy quark [39, 40, 41, 42] have been considered. For a review of simplified models for dark matter at the LHC, see Refs. [43, 44].

In this chapter, we present a new mechanism for dark matter production at the LHC, where

the visible object is itself a new particle, a Z' boson. We propose examples of models giving rise to a signal of $Z' + \not{E}_{\rm T}$, where the Z' boson can decay to pairs of charged leptons ($\ell^+\ell^-$) or to pairs of quarks leading to jets (jj), and is therefore distinguishable as a resonance in the dilepton or dijet mass spectrum. In each case, we study the sensitivity of the LHC in this channel, and compare with existing searches for the Z' without a requirement of large $\not{E}_{\rm T}$.

The models here specifically target the production of a new Z' which is present in a hypothetical, non-minimal dark sector. New Z' bosons arise in many extensions to the SM [45], and the possibility of dark matter coupled to a Z' has been explored extensively in the literature, including in the context of the LHC (see, e.g. [46, 47, 24, 48, 49, 50, 51, 52, 53, 54]). It should be noted that the experimental signature of a dijet or dilepton resonance plus missing transverse momentum does not require a Z': other possibilities, including new scalar resonances or colored resonances, are natural directions to explore.

In addition to extending the current program of $X + \not{E}_{\rm T}$ studies, the models presented here point to final states whose LHC data remains unexamined and which are natural generalizations [55] of previously performed searches for $Z/W + \not{E}_{\rm T}$ with $Z \to \ell\ell$ or $Z/W \to jj$. These data therefore contain real, untapped discovery potential, independent of theoretical interest in models of dark matter involving Z' bosons.

The models considered here are also examples of dark sector signals that, to some extent, could be hidden in existing $\not{E}_{\rm T}$-based searches. Searching specifically for a dijet or dilepton resonance reduces the backgrounds and could give a strong hint of new physics. Furthermore, many searches have been optimized for new high-mass particles. For the examples below, we find that the most unconstrained parameter space is for relatively light Z' states, those with $m_{Z'}$ below 100 GeV, where current LHC searches have low efficiency.

In the following, we first review experimental constraints on Z' gauge bosons and then

describe several models of Z'+ dark matter production. The range of Z' mass explored is 50-800 GeV: for lower masses, dijet masses would be more difficult to reconstruct due to a smaller angular separation in the partons. Work on LHC signals of $Z' + \not{E}_{\rm T}$ with lower values of $m_{Z'}$ will appear elsewhere [56], while related work focusing on leptonic Z' decays plus missing transverse momentum can be found in Ref. [57].

We consider two models with a minimal set of renormalizable interactions: dark-Higgsstrahlung from a Z', with the dark Higgs decaying invisibly; and a dark sector with two states $\chi_{1,2}$ that couple off-diagonally to the Z'. We also study the case where the production of the dark-sector states is through a higher-dimension operator. We analyze the sensitivity of the current LHC run to these models in $jj+\not{E}_{\rm T}$ and $\ell\ell+\not{E}_{\rm T}$ final states, and compare to existing constraints. For the renormalizable models, the $Z' + \not{E}_{\rm T}$ search has better sensitivity than direct resonance searches only for low Z' masses. In the operator case, it is possible to probe the scale of new interactions to around a few TeV.

4.2 Current Constraints on Z' Bosons

For simplicity, we assume a $U(1)'$ where the Z' has universal vector couplings to SM quarks:

$$\mathcal{L} \supset -\sum_q g_q \bar{q}\gamma^\mu q Z'^\mu. \tag{4.1}$$

The couplings above are the same as for gauged baryon number $U(1)_B$ with $g_q = g_B/6$, where anomaly cancellation could be achieved with additional heavy quarks or with chiral matter in a dark sector. This possibility has been studied in detail in the context of dark matter (*e.g.*, [58, 59]). However, we do not assume that the gauged baryon number is the origin of the $U(1)'$. For example, it is possible that the Z' couplings to SM fermions are generated

by higher-dimensional operators [60] while the dark sector states are directly charged under the Z'.

When we consider dilepton searches, we will introduce additional free parameters for couplings of the Z' to leptons. Since the production of the Z' does not depend on the lepton coupling (except through the dependence on the Z' width, which we neglect) we present constraints from dilepton resonances searches simply in terms of the Z' branching ratio to the appropriate lepton flavor.

Although we will not impose any relationship between the Z' coupling to quarks, leptons, or dark sector particles, one natural possibility is that of kinetic mixing [61], where a mixing of Z' and hypercharge generates couplings of the Z' to SM fermions. Since the natural size of the couplings is small in this case (10^{-2} or less), we do not consider this for the models that rely on dark matter production via the Z' couplings to quarks. However, this gives a simple way for the Z' to decay to visible states in our last model, where the Z' is only produced in the decay of dark sector states.

The range of Z' mass explored here is 50-800 GeV. For heavier masses, constraints from dilepton or dijet resonance searches are precisely where LHC searches excel since backgrounds are relatively low. The $Z' + \not{E}_{\mathrm{T}}$ signature has additional particles produced along with the Z' and so has a smaller rate than direct Z' production; therefore we expect it to be a less sensitive probe of the models in the high mass regime. Meanwhile, a low mass Z' decaying to quarks is difficult to resolve as separate jets; however, it is possible that this regime could be studied by employing jet substructure techniques [56, 62].

4.2.1 Dijet Constraints

Direct dijet resonance searches constrain a Z' coupling to quarks. We take limits on g_q as a function of $M_{Z'}$ from Ref. [63], which compiles experimental results down to $M_{Z'} = 140$ GeV. Here, the lowest mass region was covered by UA2 [64] with integrated luminosity of 10.9 pb^{-1}. At lower Z' mass, dijet resonances are more difficult to constrain due to the large QCD background. Data on the dijet spectrum down to $m_{jj} = 48$ GeV have been published by UA2 [65] (4.7 pb^{-1}) and down to 60 GeV from CDF [66] (26 nb^{-1}). While a reanalysis of the data would be needed to obtain limits on new resonances, we estimate that the UA2 dijet limits continue to weaken below 140 GeV, reaching $g_q \lesssim 1$ at $M_{Z'} = 50$ GeV (see also [67]).

Future LHC analyses may be able to provide more robust coverage of the low mass $M_{Z'}$ region. This was studied in Ref. [49], which considered associated Z' searches, such as a Z' in addition to a Z, γ, or jet. Using the additional object in the final state to improve trigger efficiency, it was shown that LHC searches can have sensitivity even down to $M_{Z'} \approx 50$ GeV and couplings comparable to or better than the estimated UA2 dijet limits.

4.2.2 Dilepton Constraints

A Z' coupling to electrons is strongly constrained by LEP measurements [68]. In the first two of our models, we will focus on the possibility that the Z' has suppressed couplings to electrons but $O(1)$ branching ratio of the Z' to muons (for example, see Ref. [69] and references therein).

Then if the Z' has a preferred coupling to muons and to quarks, a hadron collider can give interesting limits relative to the LEP precision measurements. As a direct comparison to $Z' + \not{E}_{\rm T}$ searches, we consider constraints from searches for dimuon resonances. Limits are

available from the CDF collaboration [70] down to $M_{Z'} = 100$ GeV, while ATLAS [71] and CMS [72] limits extend down to $M_{Z'} = 150$ GeV and $M_{Z'} = 300$ GeV, respectively[1]. Here published results are not available below M_Z due to the large Drell-Yan background.

Below the Z-pole, Ref. [75] showed that LHC measurements of the Drell-Yan spectrum at low invariant mass [76] can be used to set strong constraints on a Z' coupling to quarks and muons. The recast of the data leads to constraints on couplings at the $10^{-3} - 10^{-2}$ level. (In the context of kinetic mixing, the current constraint is $\epsilon < 0.012$ and can reach $\epsilon = 5 \times 10^{-3}$ for a binned 8 TeV LHC analysis at $M_{Z'} = 50$ GeV.)

We also consider small, universal couplings of the Z' to all of the charged leptons, as in the case of kinetic mixing. As discussed above, this will be most relevant in our third model (Inelastic EFT) where the Z' may be very weakly coupled to SM fermions.

4.2.3 Other Limits

A light Z' coupling to quarks contributes to the Z hadronic width through $Z \to q\bar{q}Z' \to 4j$ and through a $Z\bar{q}q$ vertex correction [77, 78]. Applying the results of Ref. [77] to the most recent measurement of $R_Z = \Gamma(Z \to \text{hadrons})/\Gamma(Z \to \mu^+\mu^-) = 20.785 \pm 0.033$ [79], this places a constraint of $g_q \lesssim 0.4 - 0.6$ for $M_{Z'} = 50 - 140$ GeV where there are no dijet resonance constraints.

Finally, even if a Z' couples only to quarks, kinetic mixing of the Z' with Z, γ can be generated at one-loop. There are strong constraints on this kinetic mixing from precision electroweak measurements [80, 78], giving a bound $\epsilon \lesssim 0.02$ for $M_{Z'} \ll M_Z$. Since the kinetic mixing parameters are model-dependent, we do not examine this constraint any further, except to note that it is particularly strong for $M_{Z'} \approx M_Z$ and so any model in this case would have

[1]LHC searches for the SM Higgs decay to dimuons can also be recast to place constraints down to $M_{Z'} = 110$ GeV [73, 74]; we do not consider these analyses as they are not directly applicable to our models, and would not qualitatively change our conclusions.

to be particularly tuned.

4.3 Models of $Z' + \not{E}_{\mathrm{T}}$ production

4.3.1 Dark Higgs

A model with a new Z' naturally comes with its own scalar (or set of scalars) responsible for spontaneous symmetry breaking. Suppose there is a new massive scalar that couples to the Z', which we call the dark Higgs, h_D. Analogous to the SM process of Higgs-boson radiation from a W or Z, the new scalar is radiated by the Z' in a dark-Higgsstrahlung process. If this new dark Higgs boson additionally couples with invisible states[2], its primary signature could be $\not{E}_{\mathrm{T}}$, as shown in Fig. 4.1.

As a minimal model for this process, we introduce a new $U(1)'$ with a charged scalar field Φ_D and an invisible singlet scalar ϕ_X:

$$\begin{aligned}\mathcal{L} \supset & |D_\mu \Phi_D|^2 + \mu_D^2 |\Phi_D|^2 - \lambda_D |\Phi_D|^4 - \frac{1}{4}(F'_{\mu\nu})^2 \\ & + \frac{1}{2}(\partial_\mu \phi_X)^2 - \lambda_X |\Phi_D|^2 \phi_X^2 - V(\phi_X). \end{aligned} \tag{4.2}$$

The dark Higgs field $\Phi_D = \frac{1}{\sqrt{2}}(v_D + h_D)$ obtains a vev v_D, giving mass to the Z'. The masses of the dark scalars h_D and ϕ_X are fixed by the scalar potentials, and the Z' couplings to quarks are as in Eq. 4.1. Furthermore, if $m_X \gtrsim 100$ GeV or is very close to $m_h/2$, it is straightforward for ϕ_X to be a good thermal relic dark matter candidate if a scalar Higgs portal coupling is added to the Lagrangian in Eq. 4.2 [81]. However, we do not require ϕ_X to be a thermal relic as this would impose a restriction on M_{h_D}.

[2]Another possibility is that the Z' decays to dark matter, while the dark Higgs decays to SM states through mixing with the SM Higgs. Then the monojet search channel would also be sensitive to the model.

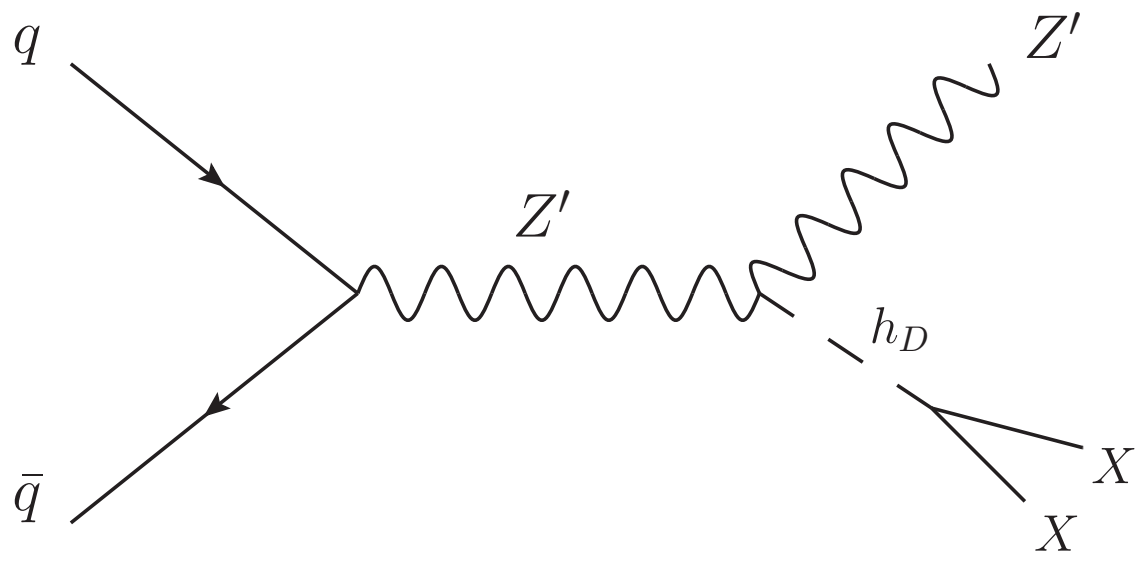

Figure 4.1: Diagram of the production of a Z' in association with a dark Higgs boson (h_D) which decays into two stable dark states, χ. It is assumed that h_D is lighter than $2M_{Z'}$ and decays with 100% branching to the invisible states.

The coupling of h_D with the new gauge boson is

$$Q_h g_z M_{Z'} h_D Z'_\mu Z'^\mu \equiv g_{h_D} M_{Z'} h_D Z'_\mu Z'^\mu, \tag{4.3}$$

where Q_h is the charge of Φ_D, which is a free parameter that we absorb by defining the effective coupling g_{h_D}. The dark Higgs can decay dominantly to the invisible ϕ_X states through the λ_X coupling, which we can take to be $O(1)$. Meanwhile, decays of $h_D \to Z'Z'^*$ will be suppressed as long as $m_{h_D} < 2M_{Z'}$. We assume the mixing of h_D with the SM Higgs is small.

As discussed in the previous section, we will take the SM charges under the Z' to be a separate free parameter, in order to be as general as possible. In considering signatures with dijets plus missing transverse momentum, we consider only the coupling to quarks; for dilepton plus missing transverse momentum signals, we will focus on the possibility of a non-zero branching fraction to muons.

The masses M_{h_D} and $M_{Z'}$ are independent quantities in the model, though they are set by the same scale v_D, with $M_{h_D}/M_{Z'} = \sqrt{2}\lambda_D/g_{h_D}$. Note that since the $Z' + \not{E}_{\rm T}$ signal due to the process shown in Fig. 4.1 favors larger g_{h_D}, this implies that for perturbative couplings the dark Higgs cannot be much heaver than the Z'. In order to capture most of the effects of different particle masses, we simply consider here two benchmark scenarios. In the "light" M_{h_D} benchmark case, we set:

$$M_{h_D} = \begin{cases} M_{Z'} & , \ M_{Z'} < 125 \text{ GeV} \\ 125 \text{ GeV} & , \ M_{Z'} > 125 \text{ GeV}, \end{cases} \tag{4.4}$$

In the "heavy" M_{h_D} benchmark case, we set[3]:

$$M_{h_D} = \begin{cases} 125 \text{ GeV} & , \ M_{Z'} < 125 \text{ GeV} \\ M_{Z'} & , \ M_{h_D} > 125 \text{ GeV}. \end{cases} \tag{4.5}$$

4.3.2 Light Vector

When the Z' is relatively light, it can be produced in the decays of dark sector states[4]. An example is given in Fig. 4.2, where the Z' possesses off-diagonal couplings to dark sector states χ_2 and χ_1. If the mass splitting between the two states is larger than $M_{Z'}$, the heavier state (χ_2) can decay to an on-shell Z' and a χ_1. Meanwhile χ_1 is stable and a dark matter candidate.

As a concrete example, we consider a Z' coupled to a new fermion which has both Dirac and Majorana masses. The fermion χ initially has a Dirac mass M_d and vector coupling with respect to the Z'. A Majorana mass can be generated from the vev of a $U(1)'$ Higgs through

[3]For the lowest mass point considered $M_{Z'} = 50$ GeV, the decay of $h_D \to Z'Z'$ is kinematically allowed; for simplicity we continue to fix the h_D invisible branching fraction to 1.

[4]Alternatively, the Z' can be produced as radiation from off-shell dark sector states [56, 57].

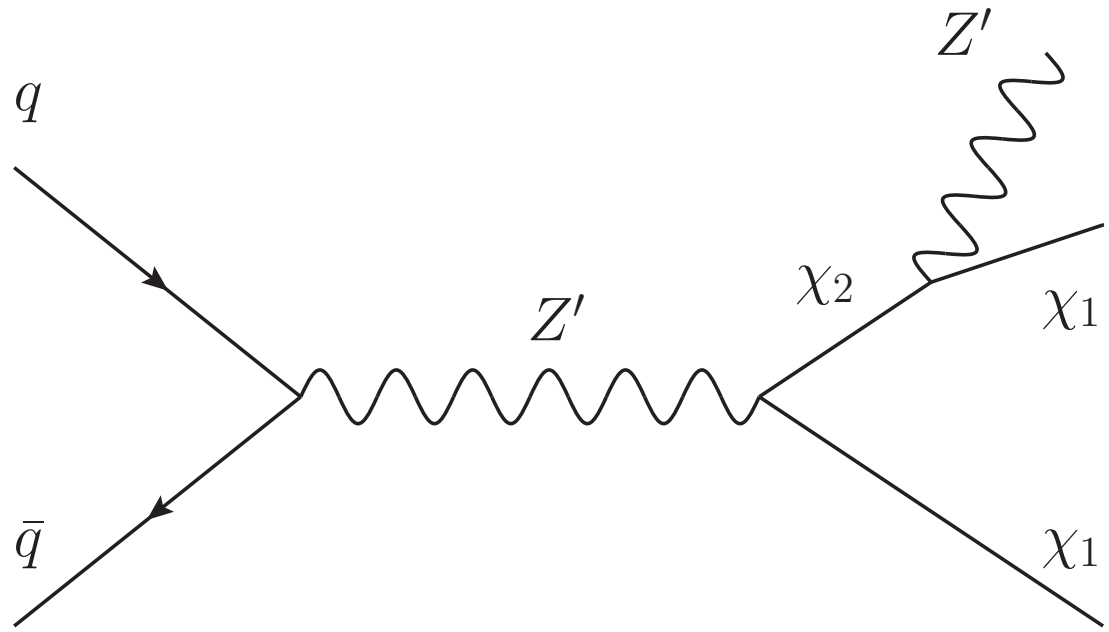

Figure 4.2: Diagram of the production of $\chi_1\chi_2$, followed by decay of the heavier dark sector state χ_2 to $Z' + \chi_1$, where χ_1 is a possible dark matter candidate.

an interaction $y_\chi \Phi_\chi \bar{\chi}\chi^c$, so that

$$\mathcal{L} \supset \bar{\chi}(i\not{D} - M_d)\chi - \frac{M_m}{2}(\bar{\chi}\chi^c + \text{h.c.}). \tag{4.6}$$

This will lead to two Majorana states $\chi_{1,2}$ with masses $M_{1,2} = |M_m \pm M_d|$. The interaction with the Z' is off-diagonal and can be written as:

$$\frac{g_\chi}{2} Z'_\mu \left(\bar{\chi}_2 \gamma^\mu \gamma^5 \chi_1 + \bar{\chi}_1 \gamma^\mu \gamma^5 \chi_2\right) \tag{4.7}$$

As long as the splitting is large enough, it is possible to have the decay $\chi_2 \to Z'\chi_1$. For example, if the scalar giving rise to the Majorana mass is also the scalar responsible for $U(1)'$ breaking, M_m can easily be of order $M_{Z'}$. Here we have assumed a charge conjugation symmetry, such that there is only one Majorana mass; if there are different Majorana masses for left- and right-handed components, diagonal couplings are also present.

As in the previous model, we allow the Z' couplings to quarks and leptons to be set by additional free parameters. Our assumption is that the χ_2 has 100% branching to $\chi_1 Z'$, and that the Z' has 100% branching to $q\bar{q}$, giving the final state signature of a dijet resonance plus missing transverse momentum. For the dilepton plus missing transverse momentum signature, we allow for a significant branching fraction of the Z' to muons.

To avoid scanning over too many parameters, we consider two sets of benchmarks for $M_{1,2}$. Since the cross section increases with lower χ_1 mass, we include one optimistic case with very light χ_1:

$$M_1 = 5 \text{ GeV}, \quad M_2 = M_1 + M_{Z'} + \Delta; \ \Delta = 25 \text{ GeV} \tag{4.8}$$

This case is somewhat tuned for large Z' mass, since it requires a cancellation between Dirac and Majorana masses.

We also include a case where the fermion masses scale with $M_{Z'}$:

$$M_1 = M_{Z'}/2, \quad M_2 = 2M_{Z'} \tag{4.9}$$

With $M_1 < M_{Z'}$, the interactions above are not sufficient for χ_1 to obtain the correct thermal abundance in the standard cosmology. Since this is model-dependent, we leave this an open question and instead focus here on lighter dark sector masses, where the LHC sensitivity is better.

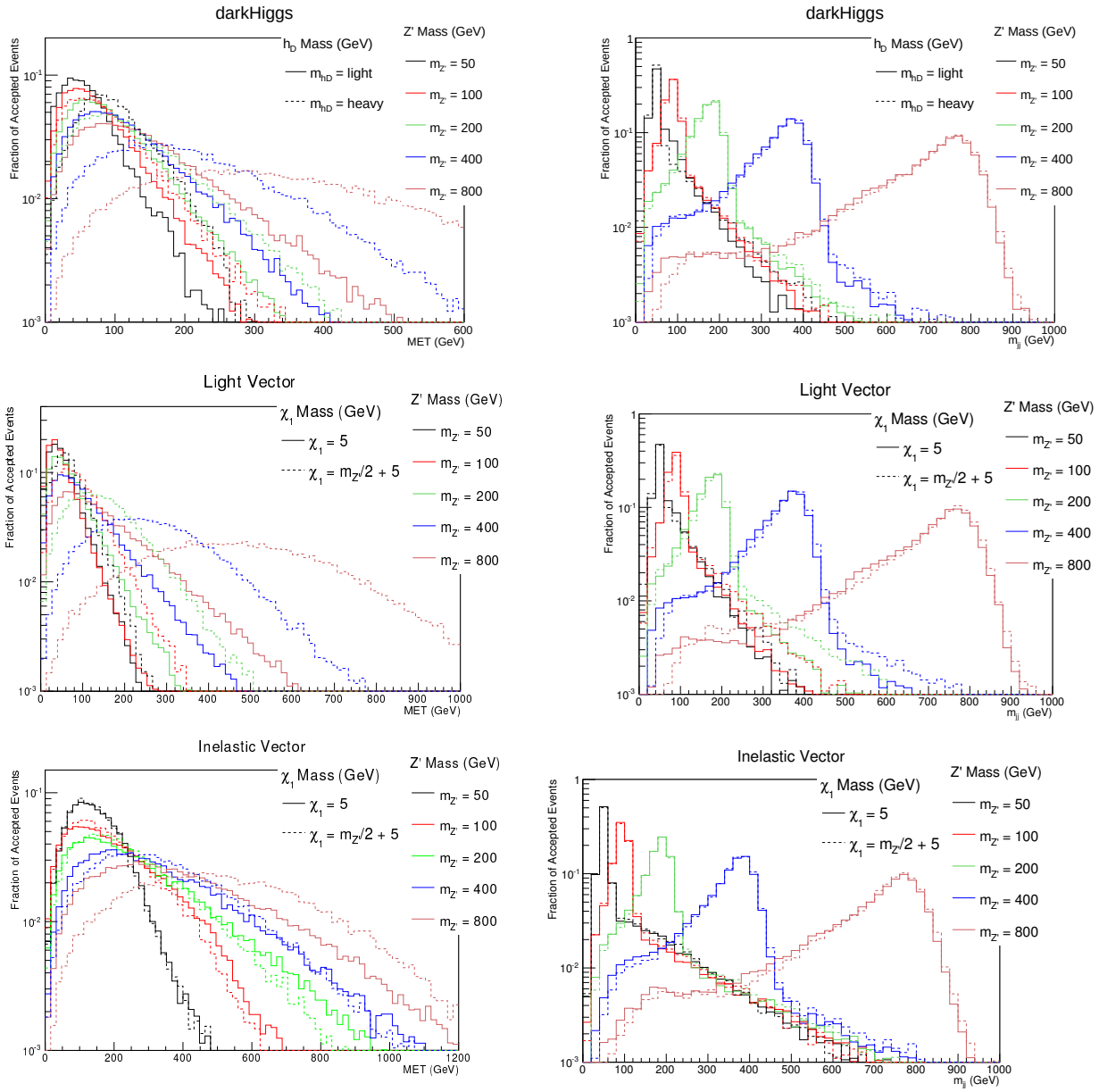

Figure 4.3: Distribution of reconstructed $\not{E}_{\mathrm{T}}$ (*left*) and m_{jj} (*right*) in the $jj + \not{E}_{\mathrm{T}}$ final state for each of the three models considered. We show a subset of our Z' mass points and consider the two cases for the masses of the other states, as discussed in the text.

4.3.3 Light Z' with Inelastic EFT coupling

The models thus far rely on the Z' coupling to quarks in order to be produced at the LHC. Rather than producing dark sector states through the new Z', we consider the possibility that it is produced through a new contact interaction:

$$\frac{1}{2\Lambda^2}\bar{q}\gamma^\mu q\left(\bar{\chi}_2\gamma^\mu\gamma^5\chi_1+\bar{\chi}_1\gamma^\mu\gamma^5\chi_2\right). \tag{4.10}$$

Similar to the model just discussed, we have assumed two dark sector states $\chi_{1,2}$ with an off-diagonal coupling to the Z'. The $Z'+\not{E}_{\mathrm{T}}$ process is analogous to that of the previous section; however, we have effectively replaced the intermediate s-channel Z' with a heavy Z'_H, where the Z'_H has been integrated out to give the operator above. For our benchmarks, the mass spectrum of the states is taken be the same as in Eqs. 4.8 and 4.9.

The Z' produced in the decay can then be very weakly coupled to SM fermions, evading many direct search constraints. For example, this small coupling could be generated by kinetic mixing of the Z' with hypercharge and kinetic mixing parameter $\epsilon \ll 1$. The only requirement is that the Z' decays to the visible fermions on collider time scales, which is easily satisfied for $\epsilon \gtrsim 10^{-5}$. For each search channel we show results assuming either a 100% branching fraction to jj or $\mu\mu$ in order to match our signal regions; however the results can easily be scaled for the case of kinetic mixing where, for example, $\mathrm{Br}(\mu\mu) \approx 0.12$ for large $M_{Z'}$.

Similar ideas have been considered in hidden valley models [82, 83], which can give lepton jet signals from multiple light Z's [84, 85]. The main difference here is a looser signal requirement of a single Z' in the final state, and a wider range of Z' masses considered, which allow reconstruction of the dijet or dilepton resonance.

4.4 LHC Sensitivity

In the following sections, we consider the $Z' \to jj$ and $Z' \to \ell\ell$ decay modes, propose an event selection and describe the expected sensitivity of the LHC dataset to $Z' + \not{E}_{\mathrm{T}}$ for each of the models above.

4.4.1 Dijet Mode

Decays of a Z' to a pair of quarks results in two high-p_{T} jets. In the following, the basic preselection requires at least two jets, each with $p_{\mathrm{T}} > 20$ GeV and $|\eta| < 2.5$. Events with a reconstructed electron or muon with $p_{\mathrm{T}} > 10$ and $|\eta| < 2.5$ are vetoed.

The candidate Z' is reconstructed from the leading two p_{T} jets. To suppress the non-peaking backgrounds, a mass window $m_{jj} \in [0.8 \times m_{Z'}, m_{Z'} + 30 \text{ GeV}]$ is applied. Distributions of m_{jj} and $\not{E}_{\mathrm{T}}$ for the signal are shown in Fig. 4.3. For further details on how these distributions vary among the models, see the Discussion section.

The primary background processes are $Z \to \nu\nu$ in association with two initial-state jets, or $W \to \ell\nu$ in association with two initial-state jets and where the charged lepton is not identified. Events are simulated at parton level with MADGRAPH5 [108], with PYTHIA [129] for showering and hadronization and DELPHES [88] with the ATLAS-style configuration for detector simulation. Backgrounds are normalized to leading-order cross sections; the uncertainty is calculated by varying the factorization and renormalization scales by factors of two. We validate our background model by comparing to the ATLAS results [30] with $m_{jj} \in [50, 120]$ GeV and $\not{E}_{\mathrm{T}} > 350{,}500$ GeV; the comparison is not precise due to the differences in the jet algorithm and radius parameters, but the estimates are roughly consistent. In Fig. 4.4, distributions of m_{jj} are shown for the expected backgrounds.

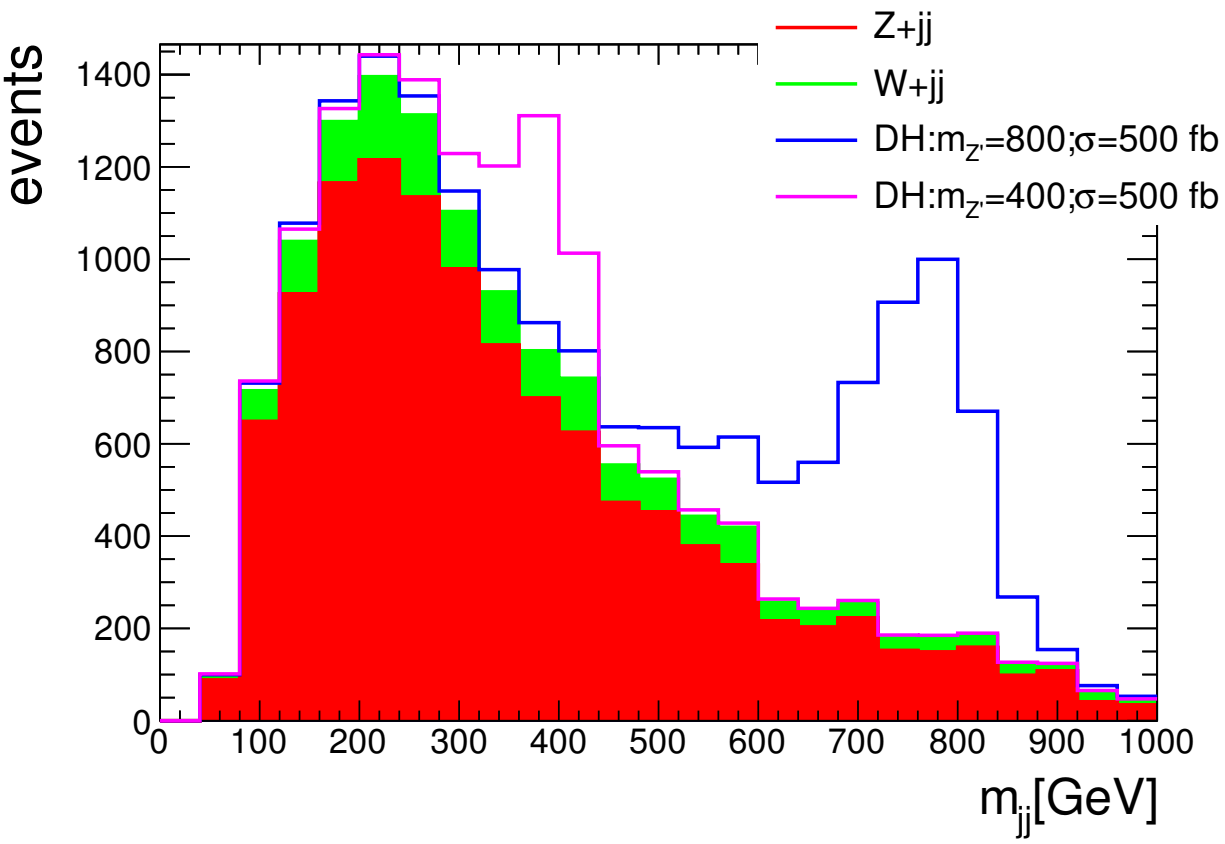

Figure 4.4: Distribution of reconstructed m_{jj} in the $jj + \not{E}_{\mathrm{T}}$ final state, for the expected SM background as well as several examples of the signal in the dark Higgs (DH) model. Events are required to satisfy the preselection as well as have $\not{E}_{\mathrm{T}} > 300$ GeV and leading jet $p_{\mathrm{T}} > 250$ GeV, but no m_{jj} selection is applied.

To suppress the large dijet background, large $\not{E}_{\mathrm{T}}$ is required. The value of the threshold in $\not{E}_{\mathrm{T}}$ is determined by optimizing with respect to the expected upper limits on the cross section. In the case of the dark Higgs and light vector models, which have similar $\not{E}_{\mathrm{T}}$ distributions, the threshold is $\not{E}_{\mathrm{T}} > 200(300)$ GeV for values of $m_{Z'} < 100$ (> 100) GeV. In the case of the inelastic EFT model, which has larger $\not{E}_{\mathrm{T}}$, the threshold is $\not{E}_{\mathrm{T}} > 300(400)$ GeV for values of $m_{Z'} < 100$ (> 100) GeV. In addition, we require the p_{T} of the leading jet to be at least $(\not{E}_{\mathrm{T}}{}^{\mathrm{thresh}} - 50)$ GeV, which helps in suppressing the V+jets background. The efficiency of the final selection is shown in Fig 4.5 and detailed in Table 4.1 for various Z' and dark matter masses.

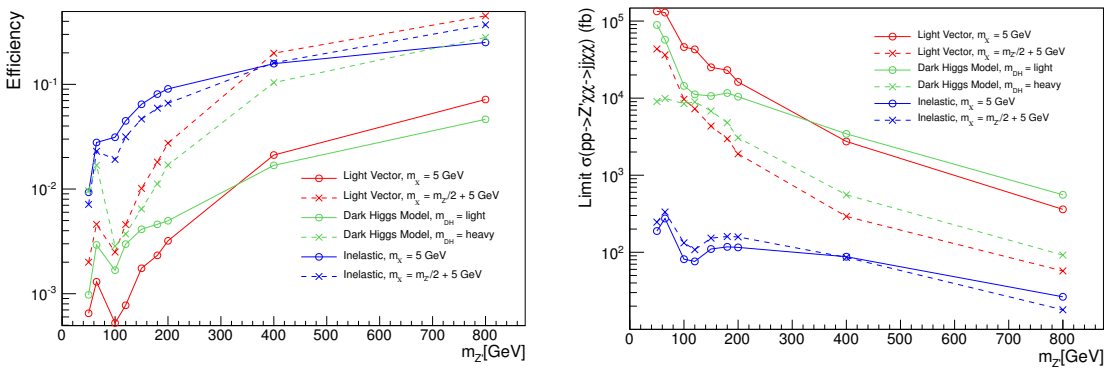

Figure 4.5: (*Left*) Efficiency of the $jj + \not{E}_{\mathrm{T}}$ selection described in the text, for two choices of mass spectra in each of the three models considered. Note that the minimum required $\not{E}_{\mathrm{T}}$ increases above $m_{Z'} > 100$ GeV. (*Right*) 95% CL upper limits on the production of $Z' \to jj + \not{E}_{\mathrm{T}}$ as a function of the Z' mass.

Upper limits are calculated in counting experiments, using a profile likelihood ratio [166] with the CLs technique [167, 91]. Limits on the production cross section of $\sigma(pp \to Z'\chi\bar{\chi} \to jj\chi\bar{\chi})$ are shown in Fig. 4.5.

4.4.2 Dilepton mode

Leptonic decays of a Z' may result in two high-p_{T} electrons or muons. In the following, the basic preselection requires at least two opposite-sign electrons or muons, each with $p_{\mathrm{T}} > 30$ GeV and $|\eta| < 2.5$ as well as $\not{E}_{\mathrm{T}} > 100$ GeV and $p_{\mathrm{T}}(\ell\ell) > 80$ GeV. Events with a third charged lepton or at least one jet with $p_{\mathrm{T}} > 20$ GeV and $|\eta| < 2.5$ are vetoed.

Due to the tight constraints on Z' coupling to electrons discussed above, we will focus on the muonic channel here. To a good approximation, the backgrounds would be larger by a factor of 2 if both lepton final states were included, and for models where the Z' decays to both charged lepton flavors, the resulting limits would be stronger by up to a factor of $\sqrt{2}$ if systematic uncertainties are not dominant.

The candidate Z' is reconstructed from the two leptons. To suppress backgrounds which do

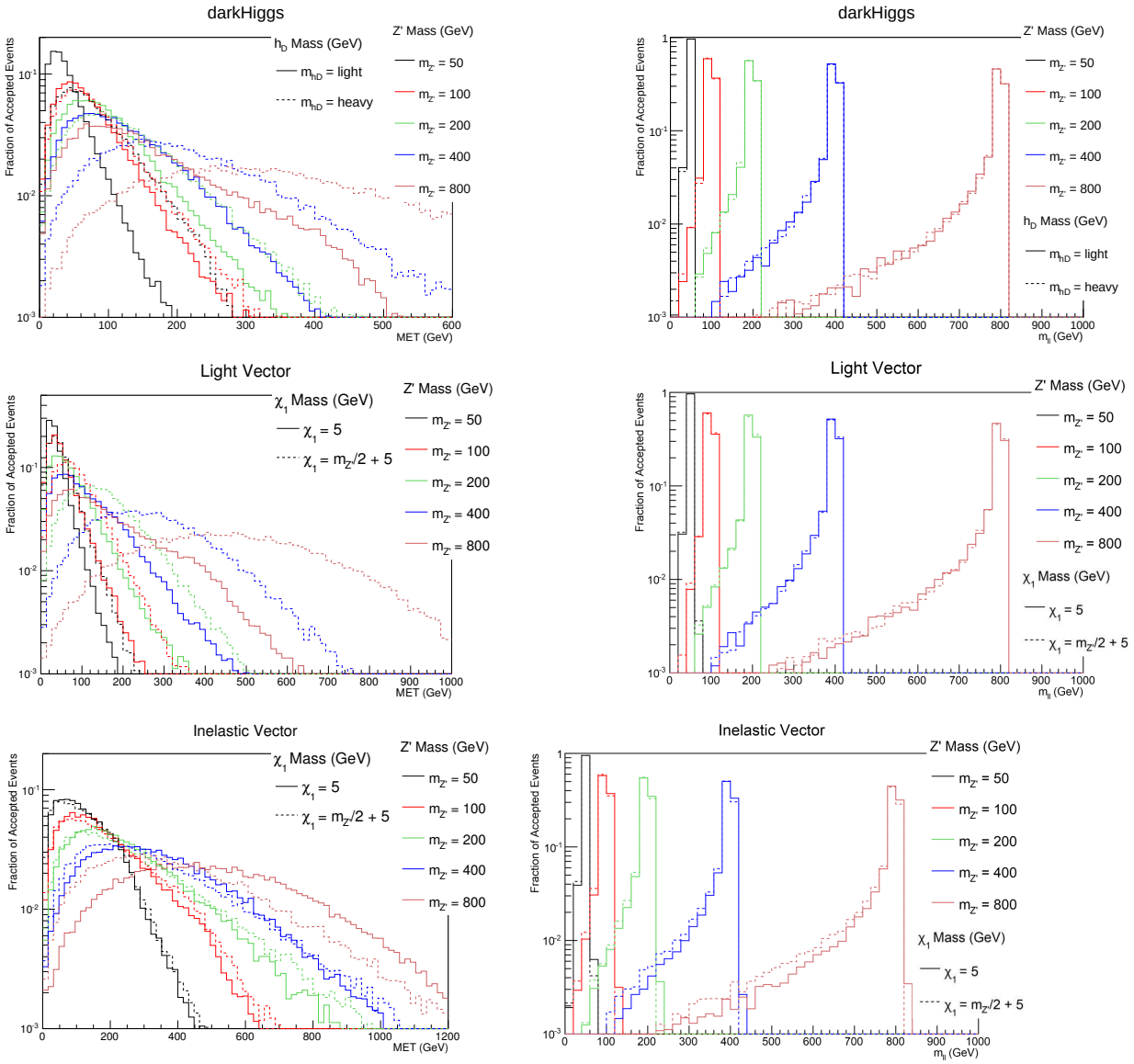

Figure 4.6: Distribution of reconstructed $\not{E}_{\mathrm{T}}$ (*left*) and $m_{\ell\ell}$ (*right*) in the $\ell\ell + \not{E}_{\mathrm{T}}$ final state for each of the three models considered. We show a subset of our Z' mass points and consider the two cases for the masses of the other states, as discussed in the text.

Table 4.1: Signal efficiency and expected background yields for several Z' masses in the $jj + \not{E}_{\mathrm{T}}$ final state. Only the heavy mass spectrum choice is listed. The background uncertainty is 27% obtained by varying the renormalization and factorization scales by factors of two.

	$m_{Z'}$ [GeV]		
	50	200	400
$\not{E}_{\mathrm{T}}$ [GeV]	> 200	> 300	> 300
	Signal Efficiencies		
Dark Higgs	0.01	0.02	0.10
Light Vector	0.002	0.03	0.20
	Background Estimates		
$Z \to \nu\nu + jj$	3000	2,200	2,000
$W \to \ell\nu + jj$	350	300	330
Total Background	3,350	2,500	2,300
$\not{E}_{\mathrm{T}}$ [GeV]	> 300	> 400	> 400
	Signal Efficiencies		
Inelastic EFT	0.007	0.07	0.16
	Background Estimates		
$Z \to \nu\nu + jj$	60	360	470
$W \to \ell\nu + jj$	10	50	65
Total Background	70	410	535

not peak at the Z' mass, a requirement that $m_{\ell\ell} \in [0.9 \times m_{Z'}, m_{Z'} + 25 \text{ GeV}]$ is applied. Distributions of $m_{\ell\ell}$ and $\not{E}_{\mathrm{T}}$ are shown in Fig. 4.6; the dependence of these on different models and mass parameter choices is examined further in the Discussion section.

The primary background processes are diboson production, such as $ZZ \to \ell\ell\nu\nu$, $WZ \to \ell\nu\ell\ell$, $WW \to \ell\nu\ell\nu$ or $Z\gamma \to \ell\ell\nu\nu$. Top pair backgrounds are effectively suppressed via the jet veto. Events are simulated at parton level with MADGRAPH5 [108], with PYTHIA [129] for showering and hadronization and DELPHES [88] for detector simulation. Backgrounds are normalized to leading-order cross sections; the uncertainty is calculated by varying the factorization and renormalization scales by factors of two. A minimum 15% uncertainty is applied to cover uncertainty due to the high-p_{T} region. We validate our background model by comparing to the ATLAS results [34] with $m_{ll} \in [76, 106]$ GeV and $\not{E}_{\mathrm{T}} > 150$, 250, 350, 450 GeV; our

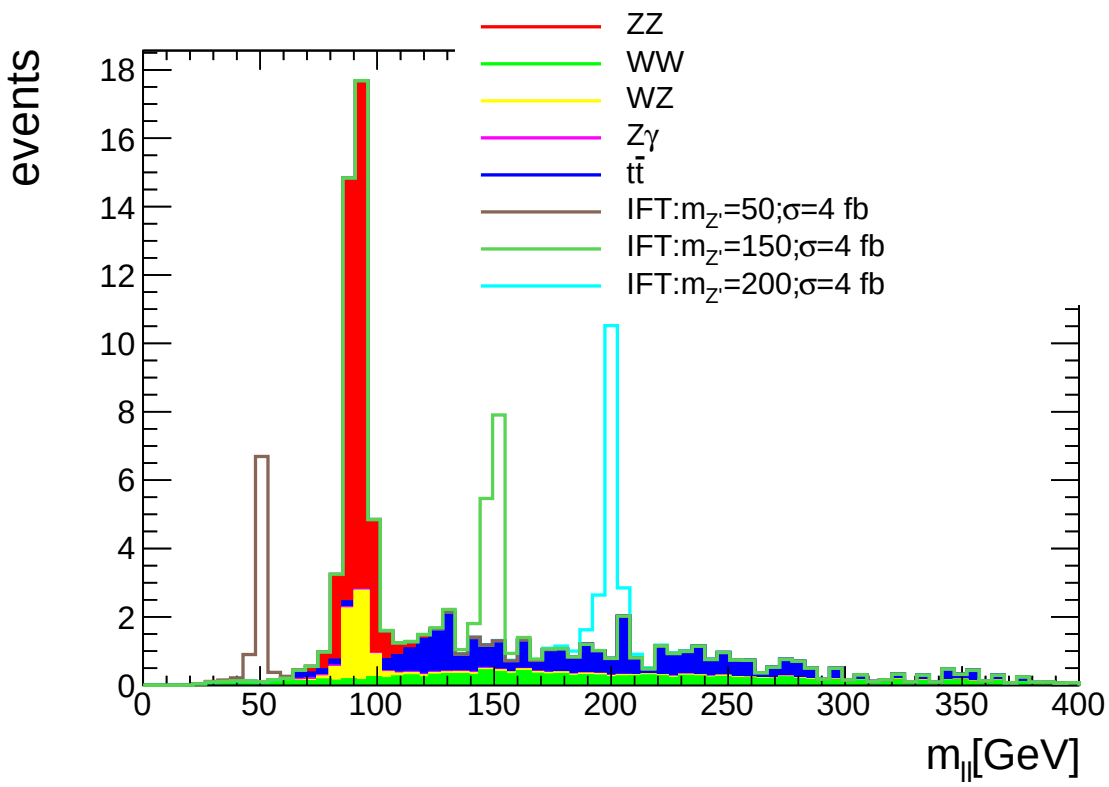

Figure 4.7: Distribution of reconstructed $m_{\ell\ell}$ in the $\mu^+\mu^- + \not{E}_{\mathrm{T}}$ final state, for the expected background as well as a signal example. The IFT label refers to the inelastic EFT model. Events are required to satisfy the preselection as well as have $\not{E}_{\mathrm{T}} > 100$ GeV and $p_{\ell\ell} > 80$ GeV, but no $m_{\ell\ell}$ selection is applied.

estimates agree within uncertainties. In Fig. 4.7, distributions of $m_{\ell\ell}$ are shown with the expected background.

As in the dijet case, large missing transverse momentum is required to suppress the large $\ell\ell$ backgrounds; the requirement $\not{E}_{\mathrm{T}} > 100$ is found to give the strongest expected limits across all models and masses. The efficiency of the selection is shown in Fig 4.8 and detailed in Table 4.2 for various Z' and dark matter masses.

Upper limits are calculated in counting experiments, using a profile likelihood ratio [166] with the CLs technique [167, 91]. Limits on the production cross section of $\sigma(pp \to Z'\chi\bar{\chi} \to \mu^+\mu^-\chi\bar{\chi})$ are shown in Fig. 4.8.

Table 4.2: Signal efficiency and expected background yields for several Z' masses in the $\mu^+\mu^- + \not{E}_{\mathrm{T}}$ final state with $\not{E}_{\mathrm{T}} > 100$ GeV. In each model, the masses are are chosen to be that of the heavy spectrum case.

	$m_{Z'}$ [GeV]		
	50	200	400
Model	Signal Efficiencies		
Dark Higgs	0.06	0.13	0.17
Light Vector	0.01	0.14	0.18
Inelastic EFT	0.09	0.16	0.18
Process	Background Estimates		
ZZ	0.4	–	–
WZ	0.1	0.3	0.1
WW	0.4	2.1	0.9
$Z\gamma^*$	0.3	0.1	–
$t\bar{t}$	0.3	6.1	0.3
Total Background	1.6	8.6	1.3

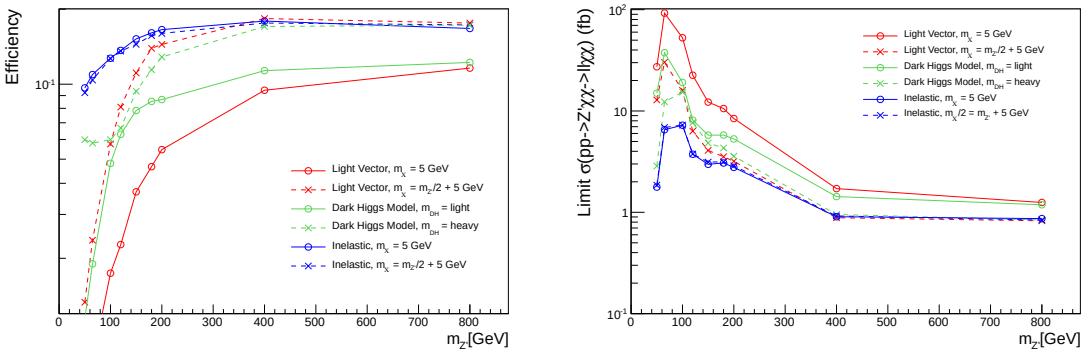

Figure 4.8: (*Left*) Efficiency of the $\mu^+\mu^- + \not{E}_{\mathrm{T}}$ selection described in the text as a function of the Z' mass, for two choices of mass spectra in each of the three models considered. (*Right*) 95% CL upper limits on the production of $(Z' \to \mu^+\mu^-) + \not{E}_{\mathrm{T}}$ as a function of the Z' mass.

4.5 Discussion

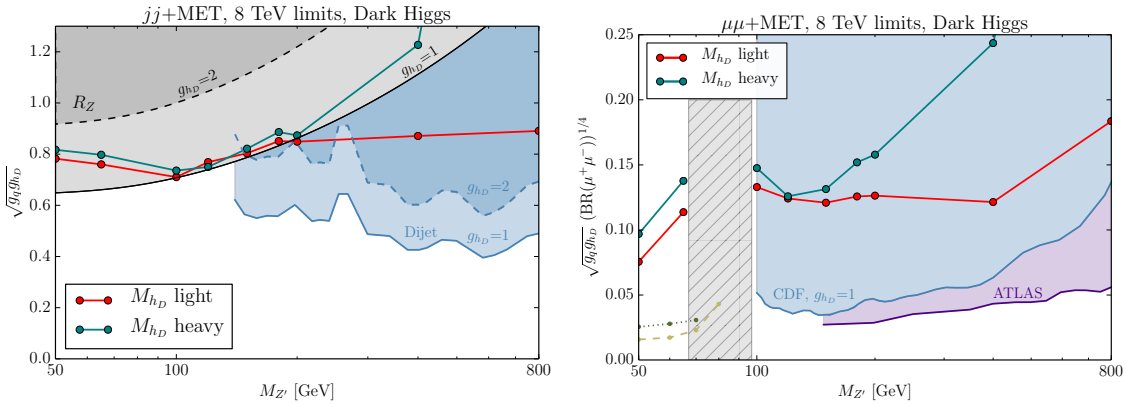

Figure 4.9: Expected upper limits at 95% CL on the product of couplings $g_q g_{h_D}$ as a function of $M_{Z'}$ for the dark Higgs model, for 8 TeV pp collisions in two different mass benchmarks. Left, the sensitivity of the $jj + \not{E}_{\mathrm{T}}$ channel is compared to the constraint on the hadronic Z width (labelled R_Z), shown in black for $g_{h_D} = 1$ (solid) and $g_{h_D} = 2$ (dashed), as well as direct dijet resonance searches [63] for a new Z'. Right, the sensitivity of the $\mu\mu + \not{E}_{\mathrm{T}}$ channel is compared to various dimuon resonance searches at CDF [70] and ATLAS [71], all shown for $g_{h_D} = 1$. The low-mass dimuon limits are interpreted from the results of Ref. [75]: both 7 TeV recast limits (dotted) and 8 TeV sensitivity projections (dashed) are shown. We do not consider masses in the grey shaded region due to the extremely large Drell-Yan background near the Z mass.

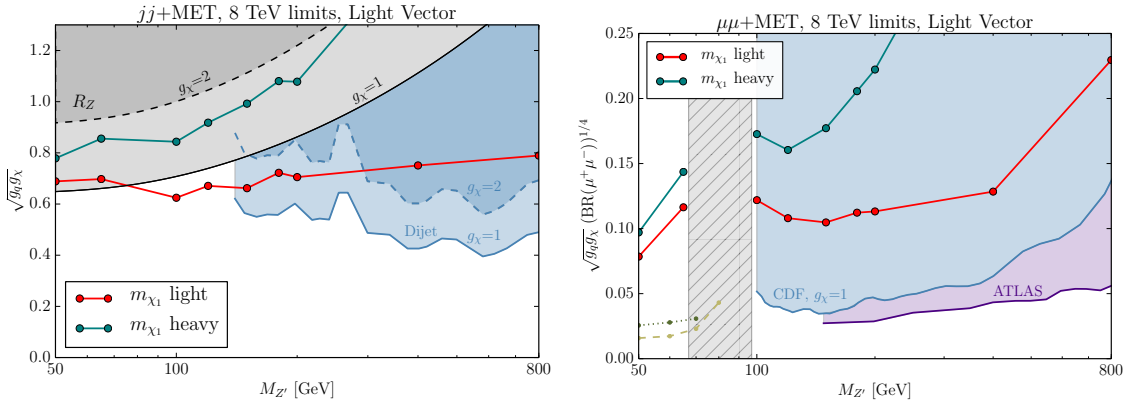

Figure 4.10: Expected upper limits at 95% CL on the product of couplings $g_q g_{h_D}$ as a function of $M_{Z'}$ in the Light Vector model, for 8 TeV pp collisions in two different mass benchmarks. The dijet and dilepton resonance limits are the same as those in Fig. 4.9, with $g_\chi = 1$ for all dilepton resonance limts.

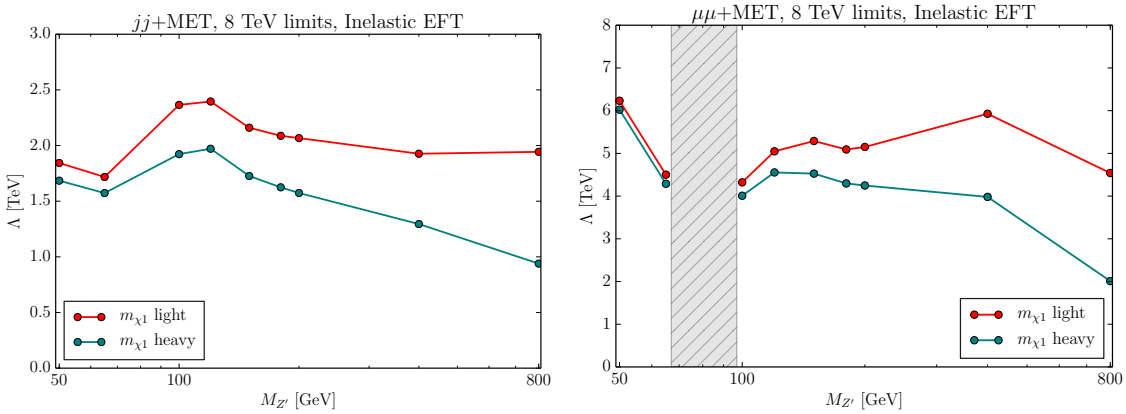

Figure 4.11: Expected lower bound at 95% CL on Λ from in the Inelastic EFT model, for 8 TeV pp collisions in two different mass benchmarks. The branching ratio of the Z' to jets and muons is taken to be 100% in each case.

The kinematic distributions in $\not{E}_{\mathrm{T}}$ and invariant masses of the different models are shown in Figs. 4.3 and 4.6. In both the dark Higgs and light vector models, the intermediate $s-$channel Z' is off-shell, and so the $\not{E}_{\mathrm{T}}$ spectra are typically softer than in the inelastic EFT model and primarily determined by total mass in the final state. As a result, the high $\not{E}_{\mathrm{T}}$ tail can look similar for different Z' masses, if the other masses are correspondingly adjusted. Note that for the dark Higgs model, the $\not{E}_{\mathrm{T}}$ spectra depends on the mass of the dark Higgs and Z', and not directly on the dark matter mass, while for the light vector model the spectra depend on the total mass in the $\chi_1\chi_2$ final state as well as on their splitting.

In the inelastic EFT model, production goes through a higher dimension operator, leading to harder $\not{E}_{\mathrm{T}}$ spectra and less sensitivity to the masses in the final state. Note that the high $\not{E}_{\mathrm{T}}$ tail in the $M_{Z'} = 50$ GeV case has an additional suppression, however, since such highly boosted low-mass Z' are unlikely to be resolved as two individual jets. Another effect that becomes important is the size of the splitting $m_{\chi_2} - m_{\chi_1}$ compared to $M_{Z'}$: when the χ_1 is very light and the splitting is very to close to $M_{Z'}$, the p_{T} of χ_2 is transferred nearly entirely to the Z' and consequently the $\not{E}_{\mathrm{T}}$ spectrum is harder. This corresponds to the case in Eq. 4.8. Conversely, less p_{T} is transfered to the Z' as the splitting is increased and as χ_1 becomes heavier, as in Eq. 4.9. The effect competes against the increase in missing transverse momentum with larger m_{χ_2}, m_{χ_1}. For the cases shown here, as we increase the dark matter masses, we also scale the splitting up accordingly. As a result, for a given Z', the $\not{E}_{\mathrm{T}}$ distribution does not change much for the two different mass spectra we consider.

4.5.1 Model Constraints

We evaluate the sensitivity of the first LHC run to each of the models presented in this chapter. The results are shown in Figs. 4.9-4.11, considering both dijet and dilepton resonances in the mass range $M_{Z'} = 50 - 800$ GeV. For each final state, we show results assuming a

100% branching ratio of the Z' to dijets or to dimuons according to our signal regions. For the dimuon final states, we do not consider the mass range $M_{Z'} \in (65, 100)$ GeV since there is a significant Drell-Yan background at these invariant masses, as shown in Fig. 4.7.

As discussed in the Constraints section, there are strong constraints on electron couplings to the Z', which severely limits the Z' branching ratio to electrons in the dark Higgs and light vector models. For uniformity in our presentation of results we have therefore considered only the muonic final state. The combined dimuon and di-electron result would be somewhat stronger in the case that the Z' decays to both flavors equally, as in the inelastic EFT model.

Constraints for the dark Higgs model are shown in Fig. 4.9, for each of the two choices of dark Higgs mass given in Eqs. 4.4-4.5. The predicted cross section for the $Z' + \not{E}_{\mathrm{T}}$ signal is proportional to $g_{h_D}^2 g_q^2$. For $M_{Z'} < 200$ GeV, the constraints for the two M_{h_D} cases are similar. The lighter M_{h_D} case has a larger cross section, but at the cost of a softer $\not{E}_{\mathrm{T}}$ spectrum and hence reduced selection efficiency, as shown in Fig. 4.5 and Fig. 4.8. Above $M_{Z'} = 200$ GeV, the limits on the heavy M_{h_D} scenario become significantly weaker due to the rapidly decreasing production cross sections.

The missing transverse momentum searches are compared in each case with the corresponding direct dijet or dilepton resonance searches from various hadron colliders. Since the $Z'+\not{E}_{\mathrm{T}}$ limits depend on an additional model parameter g_{h_D}, we show the resonance search limits for a reference value of $g_{h_D} = 1$; if this coupling were stronger, these limits would be relatively weaker. As can be seen, for $M_{Z'} > 150(100)$ GeV in the dijet (dilepton) case, the direct resonance searches give stronger constraints on the model.

At low $M_{Z'}$, constraints from the experimental collaborations are not available. However, we compare the dimuon results with the low mass dimuon resonance study in Ref. [75], finding that their recast limits of 7 TeV data would still be stronger than that from $Z' + \not{E}_{\mathrm{T}}$. Although a $\not{E}_{\mathrm{T}}$ search helps reduce backgrounds, the statistics for the signal are also lower: in

this model the mono-Z' signal requires an off-shell intermediate Z' and the production of an additional particle (the dark Higgs) in association with the Z', thus leading to a suppression of $\sim 10^3$ in the rate even for the "light" M_{h_D} case.

We find the most relevance for this signal model in the context of leptophobic Z's with mass below $\sim$ 150 GeV, where there is a gap in existing dijet resonance studies. As discussed in the Constraints section, there is an indirect constraint since a light Z' would modify the hadronic Z width, which we show in Fig. 4.9 for $g_{h_D} = 1$ and $g_{h_D} = 2$. An LHC associated Z' search [49] offers the best prospects for robust constraints competitive with the $Z' + \not{E}_{\mathrm{T}}$ results in this mass range.

The limits in the light vector model are shown in Fig. 4.10, and the behavior is qualitatively similar. In addition, we make the analogous assumptions as in the dark Higgs results described above, with the resonance search results shown for $g_\chi = 1$. We find that the dijet resonance plus $\not{E}_{\mathrm{T}}$ performs more favorably here, having the best sensitivity to the light m_{χ_1} scenario below $M_{Z'} \approx 200 - 300$ GeV. However, the dimuon plus missing transverse momentum search would again be weaker than a direct dimuon search in the entire mass range.

Finally, the inelastic EFT model limits are shown in Fig. 4.11. We constrain Λ, the scale of the operator leading to dark matter production, for each of the two channels. Since the Z' can be very weakly coupled in this model, the dijet and dimuon resonance limits above do not apply and by construction, the $Z' + \not{E}_{\mathrm{T}}$ search provides the best constraint. This model is especially interesting for the dimuon mode, where limits on Λ reach roughly 5 TeV, or around 3 TeV if rescaled to $\mathrm{Br}(\mu^+\mu^-) = 0.12$.

We also compare the results of our Z' plus missing transverse momentum search to constraints derived using existing $\not{E}_{\mathrm{T}}$-based searches for new physics beyond the standard model. For the dijet resonance plus missing transverse momentum case, the monojet search region

would be sensitive to our models since up to two jets are allowed. However, by focusing on specific m_{jj} windows, our analysis has far lower backgrounds. We also compare with the multijet plus missing transverse momentum SUSY search [92]: we find the SUSY study is less sensitive to our models, since it requires a much larger amount of visible and missing transverse momentum in order to optimize for a signal from new heavy colored particles. In the dilepton resonance case, we compare with the chargino search [95]. Here we find a fair amount of overlap in the signal regions, leading to comparable sensitivity to our models; for a more detailed discussion of the bounds obtained from applying the chargino search, see [57].

4.6 Conclusions

We have presented a new collider signal for dark matter: missing transverse momentum and a dijet or dilepton resonance. This work adds to the existing mono-X and simplified models of missing transverse momentum signals, expanding the coverage of LHC searches to new dark sector physics that may be difficult to observe in other channels. In this chapter, we introduce several simplified models for a Z' produced in association with the dark matter, determine the sensitivity of the current LHC dataset to these models, and compare with other collider searches for Z's.

When the Z' plus dark matter production relies on the Z' couplings to quarks, we find that a mono-Z' channel is more sensitive than dijet resonance searches only below $M_{Z'}$ of a few hundred GeV. In this mass range, there are currently no published results searching for a resonance from a hadronically decaying Z', and the requirement of $\not{E}_{\mathrm{T}}$ can significantly reduce the QCD dijet background. On the other hand, in these same models, when the Z' can also decay to leptons then a direct dilepton resonance search is expected to be a more powerful constraint on the model in the entire Z' mass range.

The Z' can also be produced in the decay of dark sector states, which are coupled to quarks through an effective contact interaction. Then the Z' may be weakly coupled to SM states, easily satisfying other direct collider constraints. Such a model would be challenging to observe in other missing transverse momentum searches, but give rise to a mono-Z' signal. As the first run of the LHC has shown, there is need for a broad range of dark matter signals to explore the many possibilities for the dark sector and to take full advantage of the data.

Chapter 5

ATLAS Mono V/Z' Search

5.1 Introduction

In this chapter, a search for DM particles produced in association with a hadronically decaying W or Z boson (mono-W/Z search) is performed for specific DM models, including DM production via invisible Higgs boson decays. The analysis uses LHC pp collision data at a centre-of-mass energy of 13 TeV collected by the ATLAS experiment in 2015 and 2016, corresponding to a total integrated luminosity of 36.1 fb^{-1}. The results are also expressed in terms of upper limits on visible cross sections, allowing the reinterpretation of the search results in alternative models. In addition to the mono-W/Z search, the as yet unexplored hypothesis of DM production in association with a potentially new vector boson Z' [94] is studied using the same collision data (mono-Z' search). Compared to the analysis presented in Ref. [243], the results are obtained from a larger data sample, and event selection and definition of the signal regions are further optimized, including new signal regions based on the tagging of jets from heavy-flavour hadrons and on jet topologies. Event topologies with two well separated jets from the vector boson decay are studied (referred to as the *resolved*

topology), as well as topologies with one large-radius jet from a highly boosted vector boson (referred to as the *merged topology*).

5.2 Signal models

Two signal models are used to describe DM production in the mono-W/Z final state. The first is a *simplified vector-mediator model*, illustrated by the Feynman diagram in Figure 5.1, in which a pair of Dirac DM particles is produced via an s-channel exchange of a vector mediator (Z') [96, 97]. There are four free parameters in this model: the DM and the mediator masses (m_χ and $m_{Z'}$, respectively), and the mediator couplings to the SM and DM particles (g_{SM} and g_{DM}, respectively). The minimal total mediator decay width is assumed, allowing only vector mediator decays into DM or quarks. Its value is determined by the choice of the coupling values g_{SM} and g_{DM} [97] and it is much smaller than the mediator mass. The second is a model with *invisible Higgs boson decays* in which a Higgs boson H produced in SM Higgs boson production processes decays into a pair of DM particles which escape detection. The production process with a final state closest to the mono-W/Z signature is associated production with a hadronically decaying W or Z boson (VH production, see Figure 5.1). The WH and ZH signals are predominantly produced via quark–antiquark annihilation ($q\bar{q} \to VH$), with an additional ZH contribution from gluon–gluon fusion ($gg \to ZH$). The production of a Higgs boson via gluon–gluon fusion (ggH) or vector boson fusion (VBF) followed by the Higgs boson decay into DM particles can also lead to events with large $E_{\mathrm{T}}^{\mathrm{miss}}$ and two or more jets. Especially the ggH signal has a contribution comparable to or even stronger than the VH process, since its cross section is about 20 times larger and the jets originating from initial state radiation are more central than in the VBF process. The free parameter of this model is the branching ratio $\mathcal{B}_{H\to\mathrm{inv.}}$. The cross sections for the different Higgs boson production modes are taken to be given by the SM predictions.

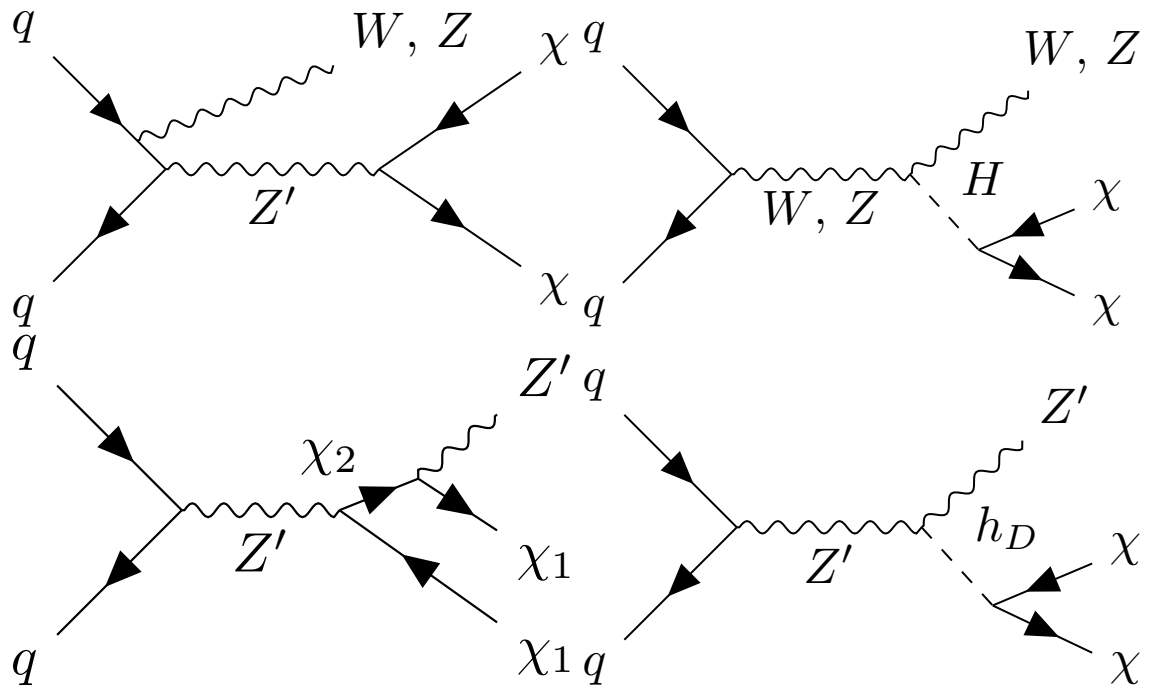

Figure 5.1: Examples of dark matter particle (χ) pair-production (top left) in association with a W or Z boson in a simplified model with a vector mediator Z' between the dark sector and the SM [96]; (top right) via decay of the Higgs boson H produced in association with the vector boson [98, 99, 100, 101, 102]; (bottom left) in association with a final-state Z' boson via an additional heavy dark-sector fermion (χ_2) [94] or (bottom right) via a dark-sector Higgs boson (h_{D}) [94].

Two signal models describe DM production in the mono-Z' final state [94]. Both models contain a Z' boson in the final state; the Z' boson is allowed to decay only hadronically. The $Z' \to t\bar{t}$ decay channel, kinematically allowed for very heavy Z' resonances, is expected to contribute only negligibly to the selected signal events and therefore the branching ratio $\mathcal{B}_{Z' \to t\bar{t}}$ is set to zero. In the first model, the so-called *dark-fermion model*, the intermediate Z' boson couples to a heavier dark-sector fermion χ_2 as well as the lighter DM candidate fermion χ_1, see Figure 5.1. The mass m_{χ_2} of the heavy fermion χ_2 is a free parameter of the model, in addition to the DM candidate mass m_{χ_1}, the mediator mass $m_{Z'}$, and the Z' couplings to $\chi_1\chi_2$ (g_{DM}) and to all SM particles (g_{SM}). The total Z' and χ_2 decay widths are determined by the choice of the mass and coupling parameter values, assuming that the only allowed decay modes are $\chi_2 \to Z'\chi_1$, $Z' \to q\bar{q}$ and $Z' \to \chi_2\chi_1$. Under these assumptions

the decay widths are small compared to the experimental dijet and large-radius-jet mass resolutions. In the second, so-called *dark-Higgs model*, a dark-sector Higgs boson h_{D} which decays to a $\chi\chi$ pair is radiated from the Z' boson as illustrated in Figure 5.1. The masses $m_{h_{\mathrm{D}}}$, m_{χ}, $m_{Z'}$ and the constants g_{SM} and g_{DM} are free parameters of the model. The latter is defined as the coupling of the dark Higgs boson h_{D} to the vector boson Z'. Similar to the dark-fermion model, the total decay widths of the Z' and h_{D} bosons are determined by the values of the mass and coupling parameters, assuming that the Z' boson can only decay into quarks or radiate an h_{D} boson. The dark Higgs boson is assumed to decay only into $\chi\chi$ or $Z'Z'^{(*)}$. The latter decay mode is suppressed for $m_{h_{\mathrm{D}}} < 2m_{Z'}$, which is the case for the parameter space considered in this chapter.

5.3 Simulated signal and background samples

All signal and background processes from hard-scatter pp collisions were modelled by simulating the detector response to particles produced with Monte Carlo (MC) event generators. The interaction of generated particles with the detector material was modelled with the GEANT4 [103, 104] package and the same particle reconstruction algorithms were employed in simulation as in the data. Additional pp interactions in the same and nearby bunch crossings (pile-up) were taken into account in simulation. The pile-up events were generated using PYTHIA 8.186 [105] with the A2 set of tuned parameters [106] and the MSTW2008LO set of parton distribution functions (PDF) [107]. The simulation samples were weighted to reproduce the observed distribution of the mean number of interactions per bunch crossing in the data.

The mono-W/Z signal processes within the simplified Z' vector-mediator model, as well as all mono-Z' signal processes, were modelled at leading-order (LO) accuracy with the MadGraph5_aMC@NLO v2.2.2 generator [108] interfaced to the PYTHIA 8.186 and PYTHIA 8.210

parton shower models, respectively. The A14 set of tuned parameters [109] was used together with the NNPDF23lo PDF set [110] for these signal samples. The mono-W/Z signal samples within the simplified vector-mediator model were generated in a grid of mediator and DM particle masses, with coupling values set to $g_{\mathrm{SM}} = 0.25$ and $g_{\mathrm{DM}} = 1$ following the 'V1' scenario from Ref. [111]. The mediator mass $m_{Z'}$ and the DM particle mass m_{χ} range from 10 GeV to 10 TeV and from 1 GeV to 1 TeV respectively. Two samples with $m_{\chi} = 1$ GeV were used to evaluate the impact of theory uncertainties on the signal, one with a mediator mass of 300 GeV and the other with a mediator mass of 600 GeV. The mono-Z' samples were simulated for mediator masses between 50 GeV and 500 GeV, with the g_{DM} coupling value set to $g_{\mathrm{DM}} = 1$. Following the current experimental constraints from dijet resonance searches [112, 113, 114, 115], in particular those for the mediator mass range below about 500 GeV studied in this analysis, the g_{SM} coupling value was set to 0.1. For this choice of the couplings, the width of the Z' boson is negligible compared to the experimental resolution, allowing limits to be set on the coupling product $g_{\mathrm{SM}} \cdot g_{\mathrm{DM}}$. For each choice of $m_{Z'}$, two signal samples were simulated in both mono-Z' models, each with a different choice of masses m_{χ_2} or $m_{h_{\mathrm{D}}}$ of intermediate dark-sector particles as summarized in Table 5.1. Out of the two samples for a given $m_{Z'}$ value, the one with a lower (higher) mass of the intermediate dark-sector particle is referred to as the 'light dark sector' ('heavy dark sector') scenario. The mass m_{χ} in the dark-Higgs model was set to 5 GeV, since it can be assumed that the kinematic properties are determined by the masses $m_{Z'}$ and $m_{h_{\mathrm{D}}}$ unless the mass m_{χ} is too large.

Processes in the mono-W/Z final state involving invisible Higgs boson decays originate from the VH, ggH and VBF SM Higgs boson production mechanisms and were all generated with the Powheg-Box v2 [116, 117, 118] generator interfaced to Pythia 8.212 for the parton shower, hadronization and the underlying event modelling. The detailed description of all generated production processes together with the corresponding cross-section calculations can be found in Refs. [119, 120]. The Higgs boson mass in these samples was set to

Table 5.1: Particle mass settings in the simulated mono-Z' samples for a given mediator mass $m_{Z'}$.

Scenario	Dark-fermion model	Dark-Higgs model
Light dark sector	$m_{\chi_1} = 5$ GeV $m_{\chi_2} = m_{\chi_1} + m_{Z'} + 25$ GeV	$m_\chi = 5$ GeV $m_{h_\mathrm{D}} = \begin{cases} m_{Z'} & , \ m_{Z'} < 125 \text{ GeV} \\ 125 \text{ GeV} & , \ m_{Z'} > 125 \text{ GeV} \end{cases}$
Heavy dark sector	$m_{\chi_1} = m_{Z'}/2$ $m_{\chi_2} = 2m_{Z'}$	$m_\chi = 5$ GeV $m_{h_\mathrm{D}} = \begin{cases} 125 \text{ GeV} & , \ m_{Z'} < 125 \text{ GeV} \\ m_{Z'} & , \ m_{Z'} > 125 \text{ GeV} \end{cases}$

$m_H = 125$ GeV and the Higgs boson was decayed through the $H \to ZZ^* \to \nu\nu\nu\nu$ process to emulate the decay of the Higgs boson into invisible particles with a branching ratio of $\mathcal{B}_{H\to\text{inv.}} = 100\%$.

The major sources of background are the production of top-quark pairs ($t\bar{t}$) and the production of W and Z bosons in association with jets (V+jets, where $V \equiv W$ or Z). The event rates and the shape of the final discriminant observables for these processes are constrained with data from dedicated control regions. Other small background contributions include diboson (WW, WZ and ZZ) and single top-quark production. Their contribution is estimated from simulation.

Events containing leptonically decaying W or Z bosons with associated jets were simulated using the Sherpa 2.2.1 generator [121], with matrix elements calculated for up to two partons at next-to-leading order (NLO) and four partons at LO using Comix [122] and OpenLoops [123] and merged with the Sherpa parton shower [124] using the ME+PS@NLO prescription [125]. The NNPDF3.0 next-to-next-to-leading order (NNLO) PDF set [110] was used in conjunction with dedicated parton shower tuning developed by the Sherpa authors. The inclusive cross section was calculated up to NNLO in QCD [126].

For the generation of $t\bar{t}$ events, Powheg-Box v2 was used with the CT10 PDF set [127]

in the NLO matrix element calculations. Electroweak t-channel, s-channel and Wt-channel single-top-quark events were generated with POWHEG-BOX v1. This event generator uses the four-flavour scheme for the NLO matrix element calculations together with the fixed four-flavour PDF set CT10f4 [127]. For all top-quark processes, top-quark spin correlations are preserved (for t-channel top-quark production, top quarks were decayed using MADSPIN [128]). The parton shower, hadronization, and the underlying event were simulated using PYTHIA 6.428 [129] with the CTEQ6L1 PDF set [130] and the corresponding Perugia 2012 set of tuned parameters [131]. The top-quark mass was set to 172.5 GeV. The EVTGEN 1.2.0 program [132] was used for the properties of b- and c-hadron decays. The inclusive $t\bar{t}$ cross section was calculated up to NNLO with soft gluon resummation at next-to-next-to-leading-logarithm (NNLL) accuracy [133]. Single top-quark production cross sections were calculated at NLO accuracy [134, 134, 135, 136, 137].

Diboson events with one of the bosons decaying hadronically and the other leptonically were generated with the SHERPA 2.1.1 event generator. Matrix elements were calculated for up to one (ZZ) or zero (WW, WZ) additional partons at NLO and up to three additional partons at LO using COMIX and OPENLOOPS, and merged with the SHERPA parton shower according to the ME+PS@NLO prescription. The CT10 PDF set was used in conjunction with dedicated parton shower tuning developed by the SHERPA authors. The event generator cross sections at NLO were used in this case. In addition, the Sherpa diboson sample cross section is scaled to account for the cross section change when switching to the G_μ scheme for the electroweak parameters, resulting in an effective value of $\alpha \approx 1/132$.

5.4 Object reconstruction and identification

The selection of mono-W/Z and mono-Z' candidate signal events and events in dedicated one-muon and two-lepton (electron or muon) control regions relies on the reconstruction and

identification of jets, electrons and muons, as well as on the reconstruction of the missing transverse momentum. These are described in the following.

Three types of jets are employed in the search. They are reconstructed from noise-suppressed topological calorimeter energy clusters [138] (*"small-R"* and *"large-R"* jets) or inner detector tracks (*"track"* jets) using the anti-k_t jet clustering algorithm [203, 206] with different values of the radius parameter R.

Small-R jets (j) with radius parameter $R = 0.4$ are used to identify vector bosons with a relatively low boost. Central jets (forward jets) within $|\eta| < 2.5$ ($2.5 \leq |\eta| < 4.5$) are required to satisfy $p_{\mathrm{T}} > 20$ GeV ($p_{\mathrm{T}} > 30$ GeV). The small-R jets satisfying $p_{\mathrm{T}} < 60$ GeV and $|\eta| < 2.4$ are required to be associated with the primary vertex using the jet-vertex-tagger discriminant [141] in order to reject jets originating from pile-up vertices. The vertex with the highest $\sum p_{\mathrm{T}}^2$ of reconstructed tracks is selected as the primary vertex. Jet energy scale and resolution, as well as the corresponding systematic uncertainties, are determined with simulation and data at $\sqrt{s} = 13$ TeV [142, 143]. Jets within $|\eta| < 2.5$ containing b-hadrons are identified using the MV2c10 b-tagging algorithm [144, 145, 146] at an operating point with a 70% b-tagging efficiency measured in simulated $t\bar{t}$ events.

Large-R jets (J) [147, 148] are reconstructed with a radius parameter of $R = 1.0$ to allow the detection of merged particle jets from a boosted vector boson decay. The trimming algorithm [204] is applied to remove the energy deposits from pile-up, the underlying event and soft radiation, by reclustering the large-R jet constituents into sub-jets with radius parameter $R = 0.2$. The sub-jets with transverse momenta below 5% of the original jet transverse momentum are removed from the large-R jet. The jet mass is calculated as the resolution-weighted mean of the mass measured using only calorimeter information and the track-assisted mass measurement [150]. Large-R jets are required to satisfy $p_{\mathrm{T}} > 200$ GeV and $|\eta| < 2.0$. In the mono-W/Z search, these jets are tagged as originating from a hadronic W- or Z-boson decay using p_{T}-dependent requirements on the jet mass and substructure

variable $D_2^{(\beta=1)}$ [151, 152]. The latter is used to select jets with two distinct concentrations of energy within the large-R jet [153, 154]. The jet mass and $D_2^{(\beta=1)}$ selection criteria are adjusted as a function of jet p_{T} to select W or Z bosons with a constant efficiency of 50% measured in simulated events. In the mono-Z' search, large-R jets are tagged as originating from the hadronic decay of a Z' boson using a jet-mass requirement and requiring $D_2^{(\beta=1)}$ <1.2, chosen to optimize the search sensitivity. The momenta of both the large-R and small-R jets are corrected for energy losses in passive material and for the non-compensating response of the calorimeter. Small-R jets are also corrected for the average additional energy due to pile-up interactions.

Track jets with radius parameter $R = 0.2$ [155] are used to identify large-R jets containing b-hadrons [156]. Inner detector tracks originating from the primary vertex, selected by impact parameter requirements, are used in the track jet reconstruction. Track jets are required to satisfy $p_{\mathrm{T}} > 10$ GeV and $|\eta| < 2.5$, and are matched to the large-R jets via ghost-association [157]. As for the small-R jets, the track jets containing b-hadrons are identified using the MV2c10 algorithm at a working point with 70% efficiency.

Simulated jets are labelled according to the flavour of the hadrons with $p_{\mathrm{T}} > 5$ GeV which are found within a cone of size $\Delta R \equiv \sqrt{(\Delta\phi)^2 + (\Delta\eta)^2} = 0.3$ around the jet axis. If a b-hadron is found, the jet is labelled as a b-jet. If no b-hadron, but a c-hadron is found, the jet is labelled as a c-jet. Otherwise the jet is labelled as a light jet (l) originating from u-, d-, or s-quarks or gluons. Simulated V+jets events are categorized according to this particle-level labelling into three separate categories: V + heavy flavour (V+HF) events, $V + cl$ events and V + light flavour (V+LF) events. The first category consists of $V + bb$, $V + bc$, $V + cc$ and $V + bl$ components, while the last one is given by the $V + ll$ component alone. In the very rare case that after the final selection only one jet is present in addition to the V boson, the missing jet is labelled as a light jet.

Electron candidates are reconstructed from energy clusters in the electromagnetic calorimeter

that are associated to an inner detector track. The electron candidates are identified using a likelihood-based procedure [158, 159] in combination with additional track hit requirements. All electrons, including those employed for the electron veto in the signal and in the one-muon and two-muon control regions, must satisfy the 'loose' likelihood criteria. An additional, more stringent criterion is applied in the two-electron control region, requiring that at least one of the electrons passes the 'medium' likelihood criteria. Each electron is required to have $p_{\mathrm{T}} > 7$ GeV, and $|\eta| < 2.47$, with their energy calibrated as described in Ref. [160, 161]. To suppress the jets misidentified as electrons, electron isolation is required, defined as an upper limit on the scalar sum of the p_{T}^{i} of the tracks i (excluding the track associated to the electron candidate) within a cone of size $\Delta R = 0.2$ around the electron, $(\sum p_{\mathrm{T}}^{i})^{\Delta R=0.2}$, relative to electron p_{T}. The p_{T}- and η-dependent limits corresponding to an isolation efficiency of 99% are applied. In addition, to suppress electrons not originating from the primary vertex, requirements are set on the longitudinal impact parameter, $|z_0 \sin\theta| < 0.5$ mm, and the transverse impact parameter significance, $|d_0|/\sigma(d_0) < 5$.

Muon candidates are primarily reconstructed from a combined fit to inner detector hits and muon spectrometer segments [162]. In the central detector region ($|\eta| < 0.1$) lacking muon spectrometer coverage, muons are also identified by matching a reconstructed inner detector track to calorimeter energy deposits consistent with a minimum ionizing particle. Two identification working points with different purity are used. All muons, including those employed for the muon veto in the signal and in the two-electron control regions, must satisfy the 'loose' criteria. In addition, the muon in the one-muon control region and at least one of the two muons in the two-muon control region must pass the 'medium' selection criteria. Each muon is required to have $p_{\mathrm{T}} > 7$ GeV and $|\eta| < 2.7$ and satisfy the impact parameter criteria $|z_0 \sin\theta| < 0.5$ mm and $|d_0|/\sigma(d_0) < 3$. All muons are required to be isolated by requiring an upper threshold on the scalar sum $(\sum p_{\mathrm{T}}^{i})^{\Delta R=0.3}$ relative to the muon p_{T} that corresponds to a 99% isolation efficiency, similarly to the electrons. In the one-muon control region, tighter isolation criteria with $(\sum p_{\mathrm{T}}^{i})^{\Delta R=0.3}/p_{\mathrm{T}} < 0.06$ are applied. In both cases, the

muon p_{T} is subtracted from the scalar sum.

The vector missing transverse momentum $E_{\mathrm{T}}^{\mathrm{miss}}$ is calculated as the negative vector sum of the transverse momenta of calibrated small-R jets and leptons, together with the tracks which are associated to the primary interaction vertex but not associated to any of these physics objects [163]. A closely related quantity, $E_{\mathrm{T}}^{\mathrm{miss(no\ lepton)}}$, is calculated in the same way but excluding the reconstructed muons or electrons. The missing transverse momentum is given by the magnitude of these vectors, $E_{\mathrm{T}}^{\mathrm{miss}} = |E_{\mathrm{T}}^{\mathrm{miss}}|$ and $E_{\mathrm{T}}^{\mathrm{miss(no\ lepton)}} = |E_{\mathrm{T}}^{\mathrm{miss(no\ lepton)}}|$. In addition, the track-based missing transverse momentum vector, $p_{\mathrm{T}}^{\mathrm{miss}}$, and similarly $p_{\mathrm{T}}^{\mathrm{miss(no\ lepton)}}$, is calculated as the negative vector sum of the transverse momenta of tracks with $p_{\mathrm{T}} > 0.5$ GeV and $|\eta| < 2.5$ originating from the primary vertex.

5.5 Event selection and categorization

Events studied in this analysis are accepted by a combination of $E_{\mathrm{T}}^{\mathrm{miss}}$ triggers with thresholds between 70 GeV and 110 GeV, depending on the data-taking periods. The trigger efficiency is measured in data using events with large $E_{\mathrm{T}}^{\mathrm{miss}}$ accepted by muon triggers. The triggers are found to be fully efficient for $E_{\mathrm{T}}^{\mathrm{miss}} > 200$ GeV and the inefficiency at lower $E_{\mathrm{T}}^{\mathrm{miss}}$ values and the corresponding uncertainty are taken into account. At least one collision vertex with at least two associated tracks is required in each event, and for the signal region selection a veto is imposed on all events with loose electrons or muons in the final state. Depending on the Lorentz boost of the vector boson, two distinct event topologies are considered: a *merged topology* where the decay products of the vector boson are reconstructed as a single large-R jet, and a *resolved topology* where they are reconstructed as individual small-R jets. Each event is first passed through the merged-topology selection and, if it fails, it is passed through the resolved-topology selection. Thus, there is no overlap of events between the two final-state topologies. For the mono-Z' search, the categorization into merged and

resolved event topologies is only performed for the mediator mass hypothesis of $m_{Z'}$ below 100 GeV. For heavier mediator masses, the angular separation of jets from the Z' boson decay is expected to be larger than the size of a large-R jet. Thus, only the resolved-topology selection criteria are applied in this case.

The mono-W/Z and mono-Z' event selection criteria applied for each of the two topologies are summarized in Table 5.2. The criteria have been optimized to obtain the maximum expected signal significance. In the merged (resolved) event topology, at least one large-R jet (at least two small-R jets) and $E_{\mathrm{T}}^{\mathrm{miss}}$ values above 250 GeV (above 150 GeV) are required in the final state. In order to suppress the $t\bar{t}$ and V+jets background with heavy-flavour jets, all events with merged topology containing b-tagged track jets not associated to the large-R jet via ghost-association are rejected. In the resolved topology, all events with more than two b-tagged small-R jets are rejected. The highest-p_{T} large-R jet in an event is considered as the candidate for a hadronically decaying vector boson in the merged topology. Similarly, in the resolved topology the two highest-p_{T} (leading) b-tagged small-R jets are selected as the candidate for a hadronically decaying W or Z boson and, if there are fewer than two b-jets in the final state, the highest-p_{T} remaining jets are used to form the hadronic W or Z boson decay candidate. Additional criteria are applied in both merged and resolved topologies to suppress the contribution from multijet events. Since the vector bosons in signal events are recoiling against the dark matter particles, a threshold is applied on the azimuthal separation between the $E_{\mathrm{T}}^{\mathrm{miss}}$ vector and the highest-p_{T} large-R jet (system of the two highest-p_{T} jets) in the merged (resolved) topology, $\Delta\phi(E_{\mathrm{T}}^{\mathrm{miss}}, J \text{ or } jj) > 120^{\mathrm{o}}$. Also, the angles between $E_{\mathrm{T}}^{\mathrm{miss}}$ and each of the up to three highest-p_{T} small-R jets should be sufficiently large, $\min\left[\Delta\phi(E_{\mathrm{T}}^{\mathrm{miss}}, j)\right] > 20^{\mathrm{o}}$, in order to suppress events with a significant $E_{\mathrm{T}}^{\mathrm{miss}}$ contribution from mismeasured jets. Events with a large $E_{\mathrm{T}}^{\mathrm{miss}}$ value originating from calorimeter mismeasurements are additionally suppressed by the requirement of a non-vanishing track-based missing transverse momentum, $p_{\mathrm{T}}^{\mathrm{miss}} > 30$ GeV, and a requirement on the azimuthal separation between the calorimeter-based and track-based missing trans-

verse momenta, $\Delta\phi(E_{\mathrm{T}}^{\mathrm{miss}}, p_{\mathrm{T}}^{\mathrm{miss}}) < 90^{\mathrm{o}}$. The $p_{\mathrm{T}}^{\mathrm{miss}}$ requirements also reduce non-collision background from beam halo or beam–gas interactions that produce signal in time with the colliding proton bunches. Such events are characterized mainly by energy deposits in the calorimeters in the absence of track activity. In the categories with two b-tagged jets the non-collision background is negligible and the expected discovery significance is higher without the $p_{\mathrm{T}}^{\mathrm{miss}}$ requirement, which is not applied. Further criteria are imposed on events with the resolved topology. The leading jet is required to have $p_{\mathrm{T}}^{j_1} > 45$ GeV. To improve the modelling of the trigger efficiency with MC events, the scalar sum of the transverse momenta of all jets is required to be $\sum p_{\mathrm{T}}^{j_i} > 120$ (150) GeV in events with two (at least three) jets.

After these general requirements, the events are classified according to the number of b-tagged jets into events with exactly zero ($0b$), one ($1b$) and two ($2b$) b-tagged jets to improve the signal-to-background ratio and the sensitivity to $Z \to bb$ decays. Small-R jets (track jets) are used for the b-tagging in the resolved (merged) category. Further selection criteria defining the final signal regions are introduced separately for the mono-W/Z and mono-Z' searches.

For the mono-W/Z search, the events in the $0b$ and $1b$ categories with merged topology are further classified into high-purity (HP) and low-purity (LP) regions; the former category consists of events satisfying the p_{T}-dependent requirements on the jet substructure variable $D_2^{(\beta=1)}$, allowing an improved discrimination for jets containing $V \to q\bar{q}$ decays, while the latter one selects all the remaining signal events. In the signal region with resolved topology, the angular separation ΔR_{jj} between the two leading jets is required to be smaller than 1.4 (1.25) in the $0b$ and $1b$ ($2b$) categories. Finally, a mass window requirement is imposed on the vector boson candidate in each of the eight resulting signal categories. In the $0b$ and $1b$ merged-topology categories, a mass requirement depending on the large-R jet p_{T} is applied. The large-R jet mass and $D_2^{(\beta=1)}$ requirements have been optimized within a dedicated study of the W/Z tagger performance [148, 147, 164]. In the $2b$ merged-topology category, in

which the signal is expected to come predominantly from $Z \to bb$ decays, a mass window requirement of 75 GeV $< m_J <$ 100 GeV is applied. The large-R jet substructure variable $D_2^{(\beta=1)}$ is not considered in this channel in order to obtain a higher signal efficiency and higher expected discovery significance. In the resolved $0b$ and $1b$ ($2b$) categories, the mass of the dijet system composed of the two leading jets is required to be 65 GeV $< m_{jj} <$ 105 GeV (65 GeV $< m_{jj} <$ 100 GeV). For the mono-Z' search, a similar classification by the b-tagging multiplicity, and by the substructure variable $D_2^{(\beta=1)}$ into high- and low-purity regions in the merged-topology category, is performed, using slightly different requirements on the substructure of the large-R jet. A p_{T}-independent requirement on the substructure variable $D_2^{(\beta=1)} < 1.2$ is used in signal regions with merged topology, as this is found to provide the maximum expected signal significance. Additional criteria also differ from the criteria applied in the mono-W/Z search. No criteria are applied on the ΔR_{jj} variable in events with the resolved topology, since the high-mass Z' bosons in dark-fermion or dark-Higgs models are less boosted than W or Z bosons in the simplified vector-mediator model, leading to a larger angular separation of jets from the Z' boson decays. The requirements on the mass of the Z' candidate are optimized for each event category as summarized in Table 5.2.

For both the mono-W/Z and the mono-Z' search, the $E_{\mathrm{T}}^{\mathrm{miss}}$ distribution in each event category is used as the final discriminant in the statistical interpretation of the data, since for the models with very large $E_{\mathrm{T}}^{\mathrm{miss}}$ values a better sensitivity can be achieved compared to the V-candidate mass discriminant. The $E_{\mathrm{T}}^{\mathrm{miss}}$ distributions after the full selection, as well as the m_J and m_{jj} distributions before the mass window requirement, are shown for various signal models in Figures 5.2 and 5.3.

Figure 5.4 shows the product $(\mathcal{A} \times \varepsilon)_{\mathrm{total}}$ of the signal acceptance $\mathcal{A}$ and selection efficiency ε for the simplified vector-mediator model and for the dark-fermion and dark-Higgs mono-Z' signal models after the full event selection. This product is defined as the number of signal events satisfying the full set of selection criteria, divided by the total number of generated

Table 5.2: Event selection criteria in the mono-W/Z and mono-Z' signal regions with merged and resolved event topologies. The symbols "j" and "J" denote the reconstructed small-R and large-R jets, respectively. The abbreviations HP and LP denote respectively the high- and low-purity signal regions with merged topology, as defined by the cut on the large-R jet substructure variable $D_2^{(\beta=1)}$.

	Merged topology	**Resolved topology**
General requirements		
$E_{\mathrm{T}}^{\mathrm{miss}}$	> 250 GeV	> 150 GeV
Jets, leptons	$\geq 1J$, 0ℓ	$\geq 2j$, 0ℓ
b-jets	no b-tagged track jets outside of J	≤ 2 b-tagged small-R jets
Multijet suppression	$\Delta\phi(E_{\mathrm{T}}^{\mathrm{miss}}, J \text{ or } jj) > 120^{\mathrm{o}}$ $\min_{i\in\{1,2,3\}} \left[\Delta\phi(E_{\mathrm{T}}^{\mathrm{miss}}, j_i)\right] > 20^{\mathrm{o}}$ $p_{\mathrm{T}}^{\mathrm{miss}} > 30$ GeV or ≥ 2 b-jets $\Delta\phi(E_{\mathrm{T}}^{\mathrm{miss}}, p_{\mathrm{T}}^{\mathrm{miss}}) < 90^{\mathrm{o}}$	
Signal properties		$p_{\mathrm{T}}^{j_1} > 45$ GeV $\sum p_{\mathrm{T}}^{j_i} > 120$ (150) GeV for 2 (≥ 3) jets

Mono-W/Z signal regions

	$0b$ **HP**	$0b$ **LP**	$1b$ **HP**	$1b$ **LP**	$2b$	$0b$	$1b$	$2b$
ΔR_{jj}	–	–	–	–	–	< 1.4	< 1.4	< 1.25
$D_2^{(\beta=1)}$ p_{T}^J-dep.	pass	fail	pass	fail	–	–	–	–
Mass requirement [GeV]	m_J W/Z tagger requirement				m_J [75, 100]	m_{jj} [65, 105]		m_{jj} [65, 100]

Mono-Z' signal regions

	$0b$ **HP**	$0b$ **LP**	$1b$ **HP**	$1b$ **LP**	$2b$	$0b$	$1b$	$2b$
$D_2^{(\beta=1)}$ <1.2	pass	fail	pass	fail	–	–	–	–
Mass requirement [GeV]	For $m_{Z'} < 100$ GeV: $[0.85m_{Z'}, m_{Z'} + 10]$ / $[0.75m_{Z'}, m_{Z'} + 10]$ For $m_{Z'} \geq 100$ GeV: no merged-topology selection applied					For $m_{Z'} < 200$ GeV: $[0.85m_{Z'}, m_{Z'} + 10]$ / $[0.75m_{Z'}, m_{Z'} + 10]$ For $m_{Z'} \geq 200$ GeV: $[0.85m_{Z'}, m_{Z'} + 20]$ / $[0.80m_{Z'}, m_{Z'} + 20]$		

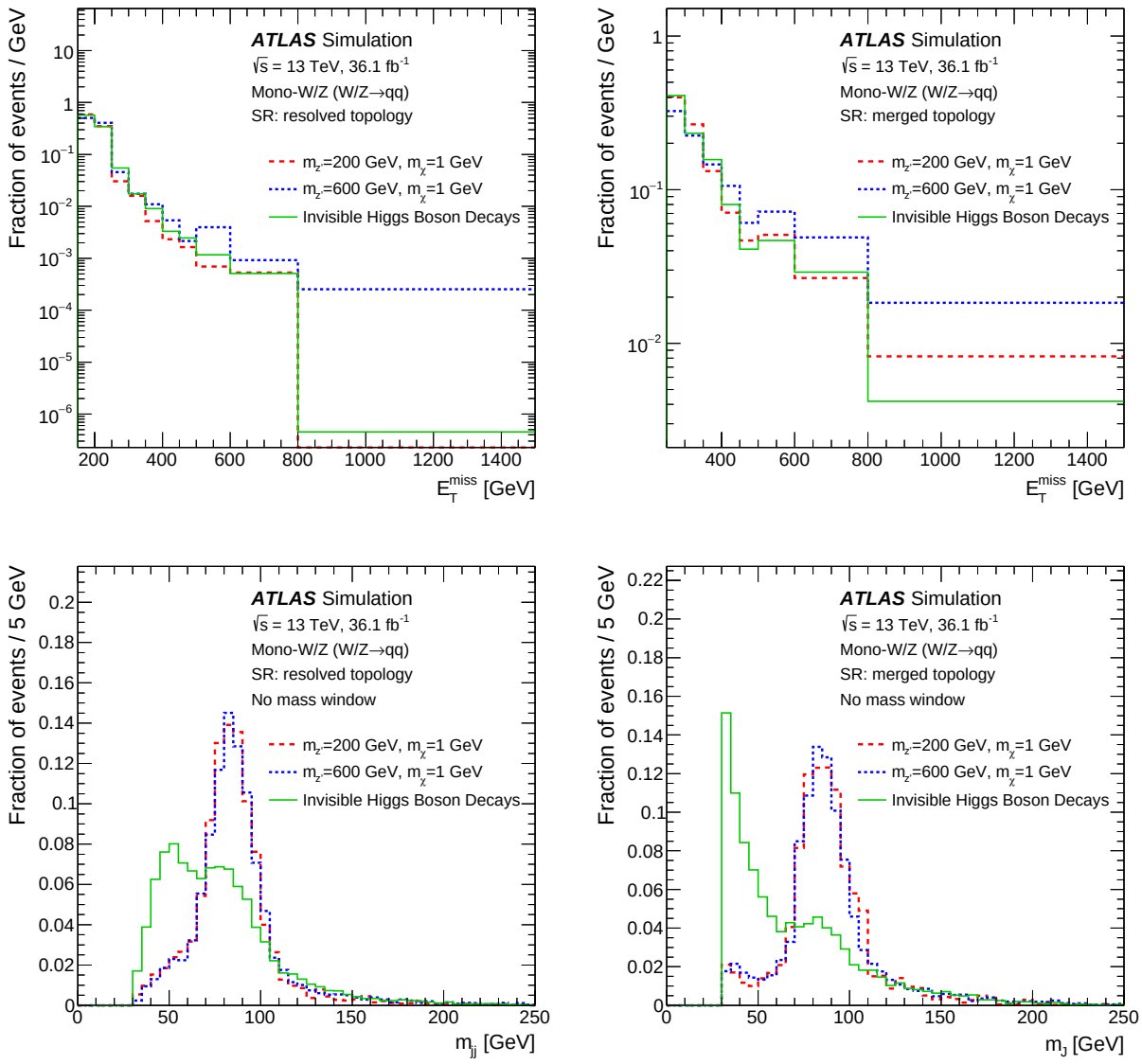

Figure 5.2: Expected distributions of missing transverse momentum, $E_{\mathrm{T}}^{\mathrm{miss}}$, normalized to unit area, for the simplified vector-mediator model and invisible Higgs boson decays after the full selection in the (a) resolved and (b) merged event topologies, and the expected invariant mass distributions (c) m_{jj} in the resolved and (d) m_J in the merged event topologies, before the mass window requirement. The signal contributions from each resolved (merged) category are summed together. The invisible Higgs boson decays include a large contribution from ggH events, which results in the observed mass distribution.

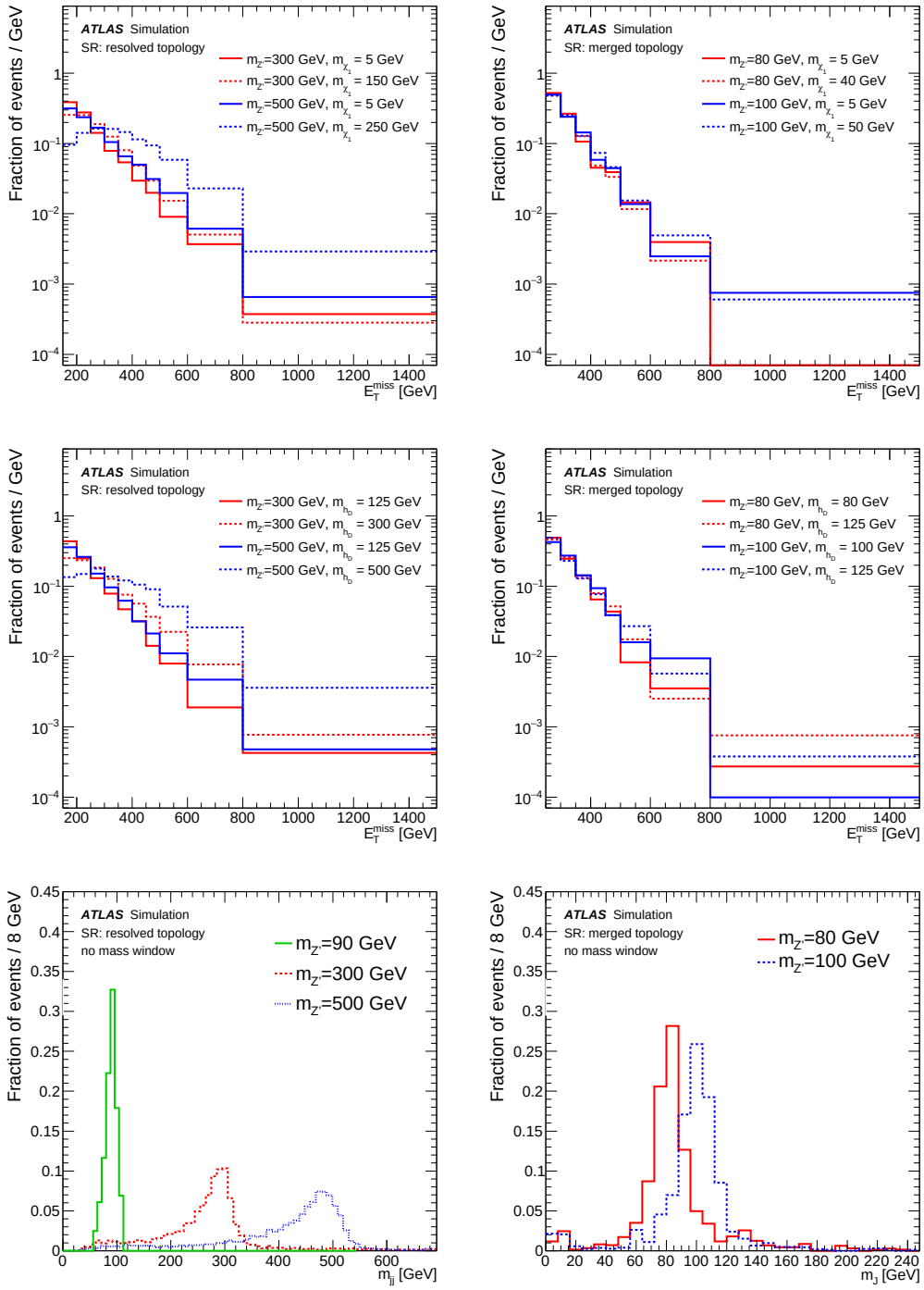

Figure 5.3: Expected distributions of missing transverse momentum, $E_{\mathrm{T}}^{\mathrm{miss}}$, normalized to unit area, after the full selection for the dark-fermion mono-Z' model in the (a) resolved and (b) merged event topologies, the dark-Higgs mono-Z' model in the (c) resolved and (d) merged event topologies, as well as the expected invariant mass distribution (e) m_{jj} in the resolved and (f) m_J in the merged event topologies for the dark-fermion mono-Z' model in the light dark-sector scenario before the mass window requirement. Similar mass distributions are also observed in the simulation of the other mono-Z' models.

signal events. For all signal models, the main efficiency loss is caused by the minimum $E_{\mathrm{T}}^{\mathrm{miss}}$ requirement.

In the simplified vector-mediator model, the $(\mathcal{A} \times \varepsilon)_{\mathrm{total}}$, obtained by summing up signal contributions from all event categories, increases from 1% for low to 15% for high mediator mass due to the increase of the missing transverse momentum in the final state.

Similarly, for the mono-Z' signal models, the $(\mathcal{A} \times \varepsilon)_{\mathrm{total}}$ increases with increasing mediator mass from 2% to 15% (from a few % to up to 40%) in scenarios with a light (heavy) dark sector. The $(\mathcal{A} \times \varepsilon)_{\mathrm{total}}$ for invisible Higgs boson decays is 0.5% when summing over all signal regions. About 58% of that signal originates from ggH, 35% from VH and 7% from VBF production processes, with $(\mathcal{A} \times \varepsilon)_{\mathrm{total}}$ values of 0.3%, 5.7% and 0.5%, respectively.

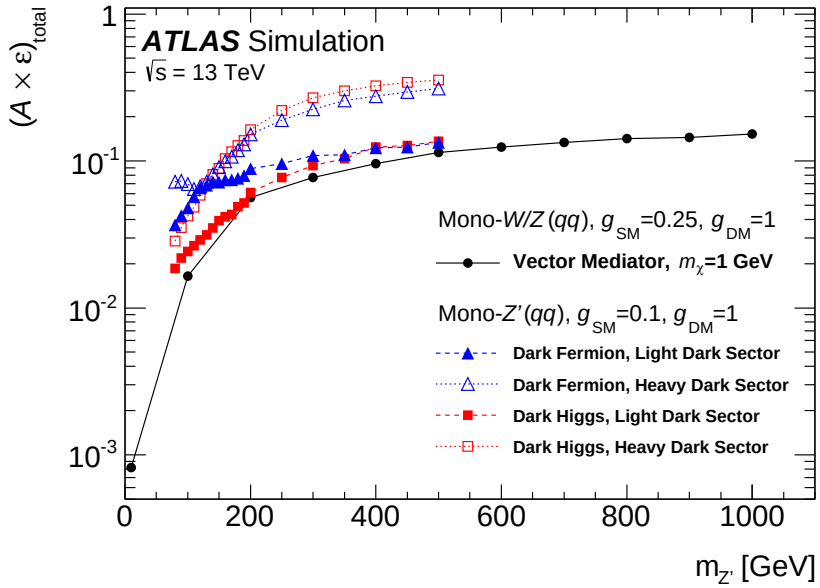

Figure 5.4: The product of acceptance and efficiency $(\mathcal{A} \times \varepsilon)_{\mathrm{total}}$, defined as the number of signal events satisfying the full set of selection criteria, divided by the total number of generated signal events, for the combined mono-W and mono-Z signal of the simplified vector-mediator model and for the mono-Z' dark-fermion and dark-Higgs signal models, shown in dependence on the mediator mass $m_{Z'}$. For a given model, the signal contributions from each category are summed together. The lines are drawn to guide the eye.

The number of signal events in a given signal-region category, relative to the total number of

signal events selected in all signal categories, depends on the signal model and mediator mass. The largest fraction is expected in the $0b$ category with resolved topology, where it ranges from 40% to 80%. This is followed by the $0b$-HP and $0b$-LP merged-topology categories with 10% to 20% of signal events in each of the two. In the mono-Z' signal models, the $1b$ and $2b$ categories with resolved topology contain about 7% to 10% of the total signal contribution. The signal contributions in every other category are below 5%.

5.6 Background estimation

The dominant background contribution in the signal region originates from $t\bar{t}$ and V+jets production. In the latter case, the biggest contributions are from decays of Z bosons into neutrinos ($Z \to \nu\nu$) and $W \to \tau\nu$, together with $W \to (e\nu, \mu\nu)$ with non-identified electrons and muons. The normalization of the $t\bar{t}$ and V+jets background processes and the corresponding shapes of the final $E_{\mathrm{T}}^{\mathrm{miss}}$ discriminant are constrained using two dedicated background-enriched data control regions with leptons in the final state. The multijet background contribution is estimated by employing additional multijet-enriched control regions. Events in each control region are selected using criteria similar to, while at the same time disjoint from, those in the signal region. Events are also categorized into merged and resolved topologies, each divided into three categories with different b-tagged jet multiplicities. No requirement is imposed on the large-R jet substructure or ΔR_{jj} and therefore there is no further classification of the merged-topology events into low- and high-purity control regions, as is the case for the signal regions. The remaining small contributions from diboson and single-top-quark production are determined from simulation.

The two control regions with one and two leptons in the final state are defined to constrain the W+jets and Z+jets background respectively, together with the $t\bar{t}$ contribution in the one lepton control region. The latter process is dominant in $2b$ control-region categories.

The *one-lepton control region* is defined by requiring no 'loose' electrons and exactly one muon with 'medium' identification, $p_{\mathrm{T}} > 25$ GeV and satisfying 'tight' isolation criteria. Events are collected by $E_{\mathrm{T}}^{\mathrm{miss}}$ triggers, as these triggers enhance most efficiently contributions from events with a signal-like topology. The *two-lepton control region* uses events passing a single-lepton trigger. One of the two reconstructed leptons has to be matched to the corresponding trigger lepton. A pair of 'loose' muons or electrons with invariant dilepton mass 66 GeV $< m_{\ell\ell} <$ 116 GeV is required in the final state. At least one of the two leptons is required to have $p_{\mathrm{T}} > 25$ GeV and to satisfy the stricter 'medium' identification criteria. To emulate the missing transverse momentum from non-reconstructed leptons (neutrinos) in W (Z) boson decays, the $E_{\mathrm{T}}^{\mathrm{miss(no\ lepton)}}$ and $p_{\mathrm{T}}^{\mathrm{miss(no\ lepton)}}$ variables are used instead of $E_{\mathrm{T}}^{\mathrm{miss}}$ and $p_{\mathrm{T}}^{\mathrm{miss}}$, respectively, for the event selection in the one-lepton and two-lepton control regions. The $E_{\mathrm{T}}^{\mathrm{miss(no\ lepton)}}$ distribution is employed in the statistical interpretation as the final discriminant in these control regions. The control-region data are also used to confirm the good modelling of other discriminant variables such as the invariant mass of the vector boson candidate and the large-R jet substructure variable $D_2^{(\beta=1)}$ in events with signal-like topology.

The multijet background contribution is estimated separately for each signal region category from a *multijet control region* selected by inverting the most effective requirement used to discriminate against multijet events in the signal region, i.e. by requiring $\min[\Delta\phi(\boldsymbol{E}_{\mathrm{T}}^{\mathrm{miss}}, j)] \equiv \min[\Delta\phi] < 20^{\mathrm{o}}$. The $E_{\mathrm{T}}^{\mathrm{miss}}$ distribution observed in this region is used as an expected multijet background shape after a simulation-based subtraction of a small contribution from non-multijet background. To account for the inversion of the $\min[\Delta\phi]$ requirement, the distribution is scaled by the corresponding normalization scale factor. This normalization scale factor is determined in an equivalent control region, but with both the $\min[\Delta\phi]$ and $\Delta\phi(\boldsymbol{E}_{\mathrm{T}}^{\mathrm{miss}}, \boldsymbol{p}_{\mathrm{T}}^{\mathrm{miss}})$ requiremens removed and the mass window criterion inverted to select only events in the mass sidebands. In this new control region, the $E_{\mathrm{T}}^{\mathrm{miss}}$ distribution from events with $\min[\Delta\phi] < 20^{\mathrm{o}}$ is fitted to the data with $\min[\Delta\phi] > 20^{\mathrm{o}}$, together with other background

contributions, and the resulting normalization factor is applied to the $E_{\mathrm{T}}^{\mathrm{miss}}$ distribution from the multijet control region. For the mono-W/Z search, the high-mass sideband is used, ranging from the upper mass window bound to 250 GeV. Since ΔR_{jj} and $\Delta\phi_{jj}$ criteria are not applied in the mono-Z' search, the event topology in the high-mass sideband is in general not close enough to the topology of the signal region. Therefore, the low-mass sideband is used for the estimate of the multijet contribution in the mono-Z' search. The sideband mass range depends on the mass of the Z' boson: the upper sideband bound is set to the lower bound of the signal region mass window and the size of the sideband is the same as the size of the mass window in the signal region. The multijet contribution is estimated to contribute up to a few percent of the total background yield depending on the signal category. The contribution from the multijet background in the one-lepton and two-lepton control regions is negligible.

For the mono-W/Z searches, all background contributions are additionally constrained by the *mass sideband regions* in the zero-lepton final state. These regions are defined by the same selection criteria, except for the requirements on the large-R jet and dijet mass values, which are required to be above the signal mass window and below 250 GeV. Events in this region are topologically and kinematically very similar to those in the full signal region, with a similar background composition. The corresponding sideband regions are also introduced for the one-lepton and the two-lepton control regions. While there is no signal contamination expected in the one-lepton and two-lepton control regions, the signal contribution in the zero-lepton mass sideband region is not negligible. Compared to the total signal contribution in the signal region described in the previous section, about 20% of additional signal events are expected in the sidebands in the case of the simplified vector-mediator model. For the invisible Higgs boson decays, the original signal contribution is increased by about 35% after including the sideband region, dominated by the ggH production process. No sideband regions are employed for the mono-Z' searches. Since the hypothesized mass of the Z' boson is a free parameter, the zero-lepton sideband regions cannot be considered free from signal

contamination.

The final estimate of background contributions is obtained from a simultaneous fit of the expected final discriminants to data in all signal, sideband and control regions. The signal contributions in the mass sideband regions are taken into account in the fit.

5.7 Systematic uncertainties

Several experimental and theoretical systematic uncertainties affect the results of the analysis. Their impact is evaluated in each bin of an $E_{\mathrm{T}}^{\mathrm{miss}}$ distribution. In this section, the impact of different sources of uncertainty on the expected signal and background yields is summarized, while the overall impact on the final results is discussed in the next section.

Theoretical uncertainties in the signal yield due to variations of the QCD renormalization and factorization scale, uncertainties in the parton distribution functions, and the underlying event and parton shower description, are estimated to be about 10–15% for the simplified vector-mediator model. For the invisible decays of the Higgs boson produced via VH and ggH processes, the theory uncertainties affect the signal yields by 5% and 10% respectively for the resolved event topology and are about two times larger for the merged topology. No systematic uncertainty in the VBF signal is considered, since it has a negligible impact on the final results. No theoretical uncertainty is considered for the mono-Z' signals, since it is negligible compared to the experimental uncertainties.

A number of theoretical modelling systematic uncertainties are considered for the background processes, affecting mostly the expected shape of the $E_{\mathrm{T}}^{\mathrm{miss}}$ distribution. These uncertainties are estimated following the studies of Ref. [120] and are briefly summarized here. The uncertainties in the V+jets background contribution come mainly from limited knowledge of the jet flavour composition in terms of the V+HF categorization, as well as

the modelling of the vector boson transverse momentum (p_{T}^{V}) and dijet mass (m_{jj}) distributions. The former are evaluated by means of scale variations in the generated SHERPA samples. In addition, the difference between the SHERPA nominal sample and an alternative MadGraph5_aMC@NLO v2.2.2 sample produced with a different matrix-element generator is added in quadrature to yield the total uncertainty. The uncertainty in the modelling of the p_{T}^{V} and m_{jj} distributions is obtained from the comparison of simulated events with dedicated control-region data, as well as comparisons with alternative generator predictions. For $t\bar{t}$ production, uncertainties in the shapes of the top-quark transverse momentum distribution, and the m_{jj} and p_{T}^{V} distributions of the V boson candidate, are considered by comparing the nominal simulated sample to alternative samples with different parton shower, matrix element generation and tuning parameters. A similar procedure is applied for the diboson and single-top-quark backgrounds. While the overall V+jets and $t\bar{t}$ normalization is determined from the fit to data, the comparison between different generators is also employed to assign a normalization uncertainty to single-top-quark and diboson production since their contributions are estimated from simulation.

An uncertainty of 100% is assigned to the multijet normalization in both the mono-W/Z and mono-Z' searches due to the statistical uncertainty in the control data, the impact of non-multijet background and the extrapolation from multijet control regions to signal regions. The shapes of the multijet background distributions are subject to an uncertainty of the order of 10%, depending on the amount of non-multijet background in each signal region.

In both the mono-W/Z and mono-Z' searches, the largest source of experimental systematic uncertainty in the merged topology is the modelling of the large-R jet properties. The large-R jet mass scale and resolution uncertainty [153, 154, 164] has an impact of up to 5% on the expected background yields, and up to 5%, 10% and 15% on the signal yields from invisible Higgs boson decays, the simplified vector-mediator model and mono-Z' models respectively. The uncertainty in the large-R jet energy resolution affects the simplified vector-mediator

signal by 3% and background by 1%. The impact on the mono-Z' signal and the signal from invisible Higgs boson decays is at the sub-percent level. The uncertainty in the scale of the $D_2^{(\beta=1)}$ substructure parameter affects the migration between the high-purity and low-purity regions, with a 5–10% (2–5%) impact on the background (mono-W/Z and mono-Z' signal) yields. The combined impact of all other large-R jet uncertainties is below a few percent. The combined impact of large-R jet uncertainties on events within the resolved-topology categories is negligible for the mono-W/Z search and below 2% for the mono-Z' searches. The small-R jet uncertainties are dominated by the energy scale and resolution uncertainties. The small-R jet energy scale uncertainty has an up to 10% (up to 6%) impact on the background (signal) yields. The uncertainty in the small-R jet energy resolution has a 2–5% impact on the signal yields. The corresponding impact of this uncertainty on the background yield is at a sub-percent level in the mass window around the W- and Z-boson mass, growing to around 1.5% for the mono-Z' search in the mass window around $m_{Z'} = 500$ GeV. The b-tagging calibration uncertainty affects the migration of signal and background events between categories with different b-tag multiplicities by up to 10%. The uncertainty in the missing transverse momentum component which is not associated with any of the selected objects with high transverse momentum affects the background (signal) yields by about 1–3% (2–10%). The uncertainties in the trigger efficiency, lepton reconstruction and identification efficiency, as well as the lepton energy scale and resolution, affect the signal and background contributions only at a sub-percent level.

The uncertainty in the combined 2015+2016 integrated luminosity is 2.1%. It is derived, following a methodology similar to that detailed in Ref. [165], from a calibration of the luminosity scale using x–y beam-separation scans performed in August 2015 and May 2016.

5.8 Results

5.8.1 Statistical interpretation

A profile likelihood fit [166] is used in the interpretation of the data to search for dark matter production. The likelihood function used to fit the data is defined as the product of conditional probabilities P over binned distributions of discriminating observables in each event category j,

$$\mathcal{L}(\mu, \boldsymbol{\theta}) = \prod_{j}^{N_{\text{categories}}} \prod_{i}^{N_{\text{bins}}} P\left(N_{ij} \mid \mu S_{ij}(\boldsymbol{\theta}) + B_{ij}(\boldsymbol{\theta})\right) \prod_{k}^{N_{\text{nuisance}}} \mathcal{G}(\theta_k) \, .$$

The likelihood function depends on the signal strength μ, defined as the signal yield relative to the prediction from simulation, and on the vector of nuisance parameters $\boldsymbol{\theta}$ accounting for the background normalization and systematic uncertainties. The Poisson distributions P correspond to the observation of N_{ij} events in each bin i of the discriminating observable given the expectations for the background, $B_{ij}(\boldsymbol{\theta})$, and for the signal, $S_{ij}(\boldsymbol{\theta})$. A constraint on a nuisance parameter θ_k is represented by the Gaussian function $\mathcal{G}(\theta_k)$. The correlations between nuisance parameters across signal and background processes and categories are taken into account.

For the mono-W/Z search, the event categories include all eight zero-lepton signal regions, six one-lepton and six two-lepton control regions, as well as the corresponding sideband regions for each of these twenty categories. In comparison, no sideband regions are employed for the mono-Z' search and only categories with the resolved topology are considered for $m_{Z'} > 100$ GeV. In the zero-lepton signal and sideband regions, the $E_{\text{T}}^{\text{miss}}$ distribution is used as the discriminating variable since the signal process results in relatively large $E_{\text{T}}^{\text{miss}}$ values compared to the backgrounds. In order to constrain the backgrounds and the $E_{\text{T}}^{\text{miss}}$ shape in the signal region, the $E_{\text{T}}^{\text{miss(no lepton)}}$ variables are used in the fit in the

one- and two-lepton control regions. The normalizations of the W+HF, W+LF, Z+HF, Z+LF and $t\bar{t}$ background components are treated as unconstrained parameters in the fit, independent from each other and correlated across all event categories. The uncertainties in the flavour composition of the V+HF processes are taken into account following studies. The normalization of other background components is constrained according to their theory uncertainty. A possible difference between the normalization factors in events with resolved and merged topologies for the W+jets, Z+jets and $t\bar{t}$ processes due to systematic modelling effects is taken into account by means of two additional constrained nuisance parameters. The multijet contribution is only considered in the signal regions and the corresponding mass sidebands, with uncorrelated normalization factors in each category.

5.8.2 Measurement results

The normalization of the W+HF, W+LF and Z+LF background components obtained from a fit to the data under the background-only hypothesis is in a good agreement with the SM expectation, while the Z+HF ($t\bar{t}$) normalization is 30% higher (20% lower) than the expected SM value. In addition to the normalization factors, the final background event yields in each event category are also affected by the systematic uncertainties. For all backgrounds other than Z+HF and $t\bar{t}$, the number of background events obtained from the fit agrees well with the prediction from simulation in each event category individually. The observed number of events passing the final mono-W/Z signal selection is shown for each event category in Table 5.3 together with the expected background contributions obtained from the fit under the background-only hypothesis. The expectations for several signal points within the simplified vector-mediator model and for the invisible Higgs boson decays are shown in addition for comparison. Figures 5.5 and 5.6 show the corresponding distributions of the missing transverse momentum in the merged and resolved mono-W/Z signal regions, respectively. The background contributions which are illustrated here are obtained from a simultaneous fit

of the expected final discriminants to data with a background-only hypothesis in all signal, sideband and control regions. In this scenario the signal regions lead to a strong constraint of the total background estimate, which is relaxed with a floating signal contribution in the final fit.

Similarly, the observed and expected numbers of events passing the final mono-Z' selection are shown in Tables 5.4 and 5.5 for mediator masses $m_{Z'}$ of 90 GeV and 350 GeV respectively. The expected and observed numbers of background events for the $m_{Z'}$ hypothesis of 90 GeV are similar to those from the mono-W/Z search in all categories, except for the $2b$-tag category with resolved topology. There are about three times more events in that category for the mono-Z' search since no requirement on ΔR_{jj} is applied, as opposed to the strict requirement of $\Delta R_{jj} < 1.25$ employed in the mono-W/Z search. The distributions of the missing transverse momentum in each mono-Z' signal region for these mediator masses are shown in Figures 5.7 and 5.8.

The impact of the different sources of systematic uncertainty on the sensitivity of the mono-W/Z and mono-Z' searches is estimated by means of fits of the signal-plus-background model to hypothetical data comprized of these signals (with signal strength $\mu = 1$) plus expected background contributions. The resulting uncertainties on the signal strength μ serve as a measure of the analysis sensitivity and are summarized in Table 5.6. Tests of the background-only versus the signal-plus-background hypothesis using a profile likelihood test statistic show no significant deviation from the SM background expectation for any of the signal mass points, in both the mono-W/Z and mono-Z' searches. A modified frequentist method with the $\mathrm{CL_s}$ formalism [167] is used to set upper limits on the signal strength μ at 95% confidence level for all signal models.

Table 5.3: The expected and observed numbers of events for an integrated luminosity of 36.1 fb^{-1} and $\sqrt{s} = 13$ TeV, shown separately in each mono-W/Z signal region category. The background yields and uncertainties are shown after the profile likelihood fit to the data (with $\mu = 0$). The quoted background uncertainties include both the statistical and systematic contributions, while the uncertainty in the signal is statistical only. The uncertainties in the total background can be smaller than those in individual components due to anti-correlations of nuisance parameters.

			Merged topology		
Process	0b-HP	0b-LP	1b-HP	1b-LP	2b
Vector-mediator model,					
m_χ =1 GeV, $m_{Z'}$ =200 GeV	814 ± 48	759 ± 45	96 ± 18	99 ± 16	49.5 ± 4.3
m_χ =1 GeV, $m_{Z'}$ =600 GeV	280.9 ± 9.0	268.5 ± 8.8	34.7 ± 3.6	33.8 ± 3.1	15.38 ± 0.84
Invisible Higgs boson decays (m_H = 125 GeV, $\mathcal{B}_{H\to\text{inv.}}$ = 100%)					
VH	408.4 ± 2.1	299.3 ± 2.0	52.06 ± 0.85	44.06 ± 0.82	27.35 ± 0.52
ggH	184 ± 19	837 ± 35	11.7 ± 3.8	111 ± 30	12.3 ± 4.2
VBF	29.1 ± 2.5	96.0 ± 4.6	2.43 ± 0.36	5.83 ± 0.43	0.50 ± 0.07
W+jets	3170 ± 140	10120 ± 380	218 ± 28	890 ± 110	91 ± 12
Z+jets	4750 ± 200	15590 ± 590	475 ± 52	1640 ± 180	186 ± 12
$t\bar{t}$	775 ± 48	937 ± 60	629 ± 27	702 ± 34	50 ± 11
Single top-quark	159 ± 12	197 ± 13	89.7 ± 6.7	125.5 ± 8.7	16.1 ± 1.7
Diboson	770 ± 110	960 ± 140	88 ± 14	115 ± 18	54 ± 10
Multijet	12 ± 35	49 ± 140	3.7 ± 3.3	15 ± 13	9.3 ± 9.4
Total background	9642 ± 87	27850 ± 150	1502 ± 31	3490 ± 52	407 ± 15
Data	9627	27856	1502	3525	414

	Resolved topology		
Process	0b	1b	2b
Vector-mediator model,			
m_χ =1 GeV, $m_{Z'}$ =200 GeV	5050 ± 130	342 ± 29	136.7 ± 6.0
m_χ =1 GeV, $m_{Z'}$ =600 GeV	840 ± 16	59.9 ± 4.6	27.86 ± 0.94
Invisible Higgs boson decays (m_H = 125 GeV, $\mathcal{B}_{H\to\text{inv.}}$ = 100%)			
VH	2129.6 ± 6.4	171.7 ± 2.2	104.7 ± 1.2
ggH	4111 ± 78	178 ± 16	37 ± 11
VBF	514 ± 12	19.8 ± 2.3	2.33 ± 0.72
W+jets	117500 ± 4600	5000 ± 680	598 ± 98
Z+jets	135400 ± 5600	7710 ± 780	1219 ± 67
$t\bar{t}$	13800 ± 780	12070 ± 420	2046 ± 70
Single top-quark	2360 ± 140	1148 ± 71	222 ± 14
Diboson	6880 ± 950	514 ± 71	228 ± 34
Multijet	11900 ± 2300	1130 ± 370	290 ± 150
Total background	287770 ± 570	27580 ± 170	4601 ± 90
Data	287722	27586	4642

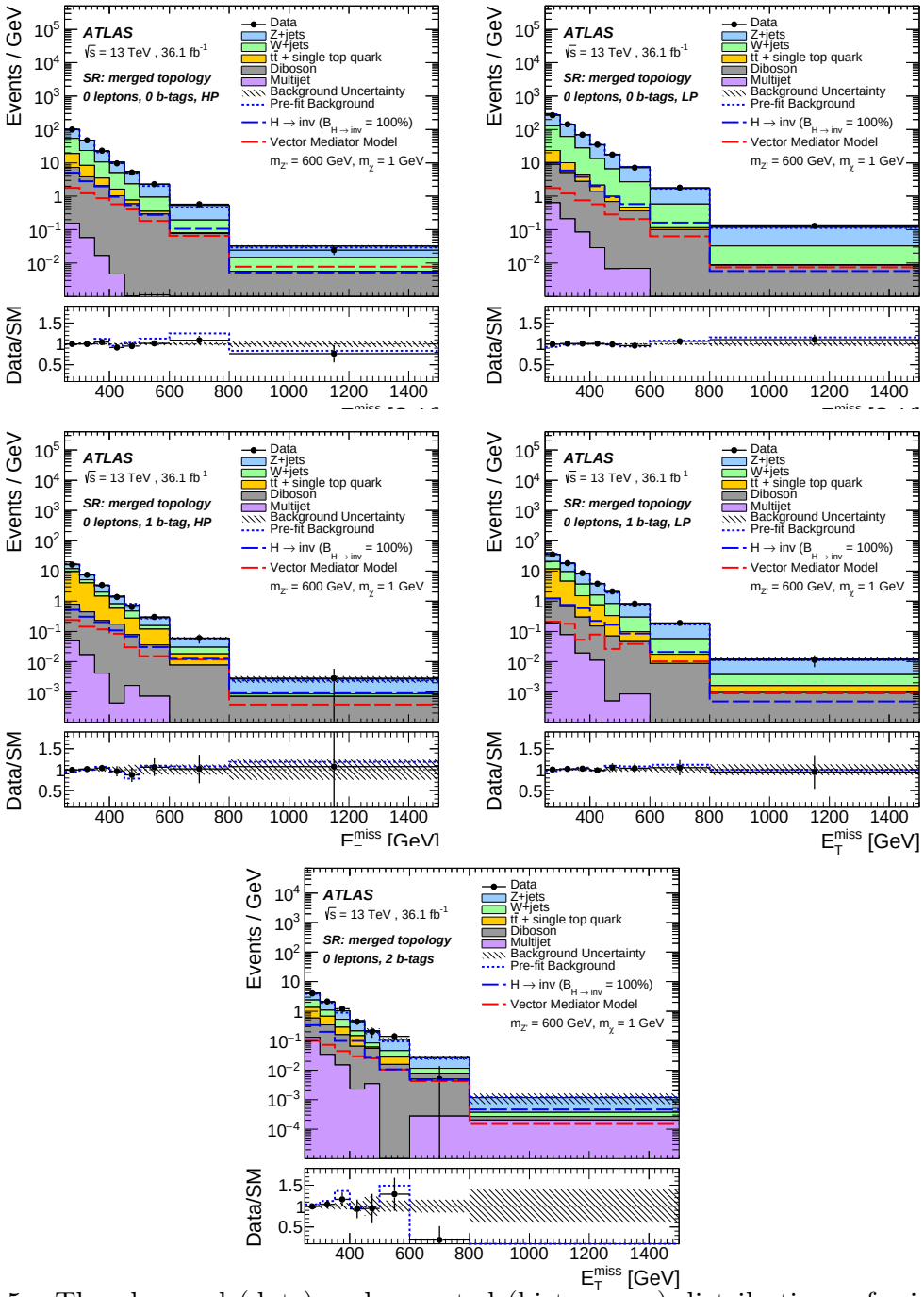

Figure 5.5: The observed (dots) and expected (histograms) distributions of missing transverse momentum, $E_{\mathrm{T}}^{\mathrm{miss}}$, obtained with 36.1 fb^{-1}of data at $\sqrt{s} = 13$ TeV in the mono-W/Z signal region with the merged event topology after the profile likelihood fit (with $\mu = 0$), shown separately for the (a) 0b-HP, (b) 0b-LP, (c) 1b-HP, (d) 1b-LP, and (e) 2b-tag event categories. The total background contribution before the fit to data is shown as a dotted blue line. The hatched area represents the total background uncertainty. The signal expectations for the simplified vector-mediator model with $m_{\chi} = 1$ GeV and $m_{Z'} = 600$ GeV (dashed red line) and for the invisible Higgs boson decays (dashed blue line) are shown for comparison. The inset at the bottom of each plot shows the ratio of the data to the total post-fit (dots) and pre-fit (dotted blue line) background expectation.

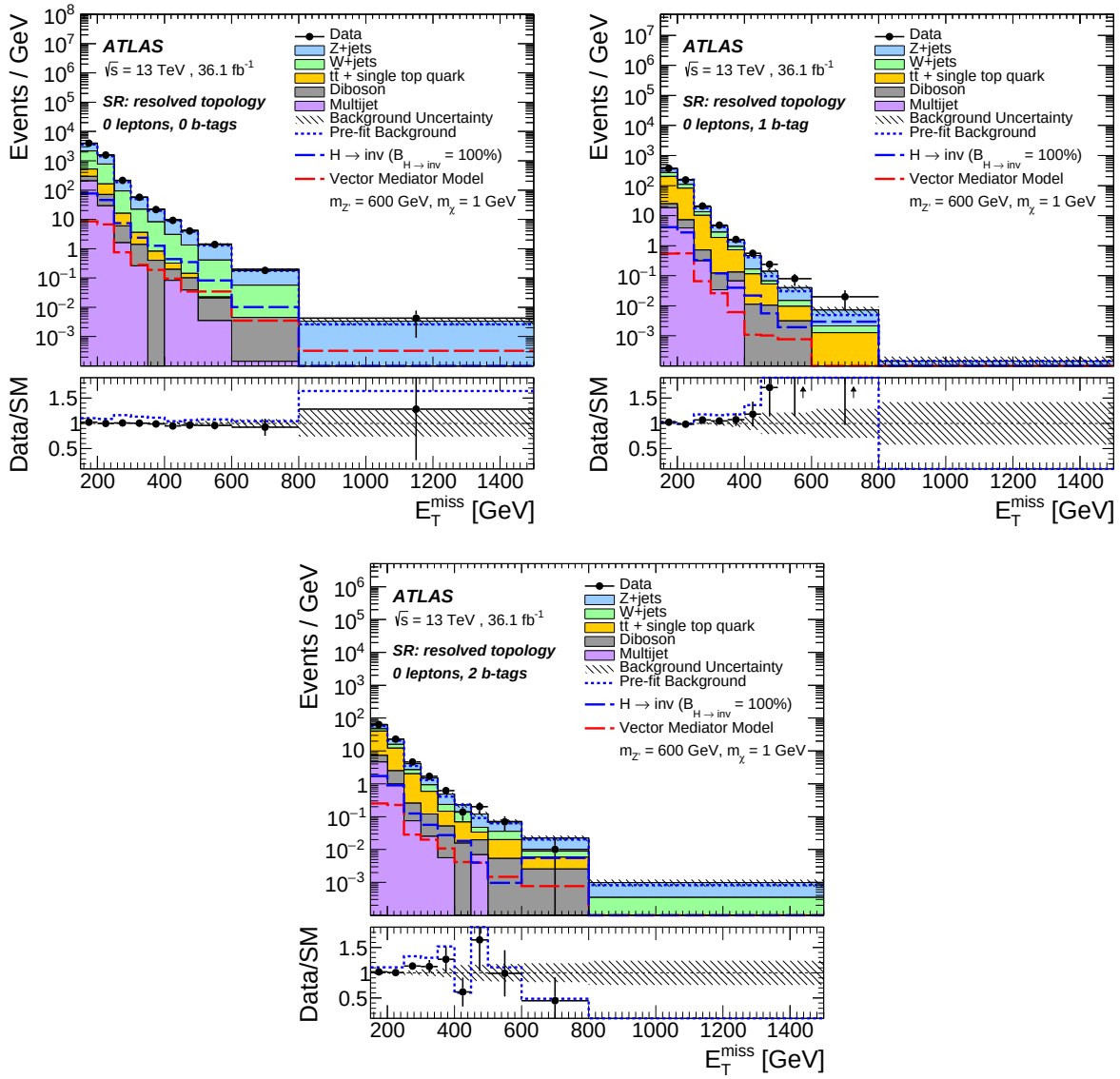

Figure 5.6: The observed (dots) and expected (histograms) distributions of missing transverse momentum, $E_{\mathrm{T}}^{\mathrm{miss}}$, obtained with 36.1 fb^{-1}of data at $\sqrt{s} = 13$ TeV in the mono-W/Z signal region with the resolved event topology after the profile likelihood fit (with $\mu = 0$), shown separately for the (a) 0b-, (b) 1b- and (c) 2b-tag categories. The total background contribution before the fit to data is shown as a dotted blue line. The hatched area represents the total background uncertainty. The signal expectations for the simplified vector-mediator model with $m_{\chi} = 1$ GeV and $m_{Z'} = 600$ GeV (dashed red line) and for the invisible Higgs boson decays (dashed blue line) are shown for comparison. The inset at the bottom of each plot shows the ratio of the data to the total post-fit (dots) and pre-fit (dotted blue line) background expectation.

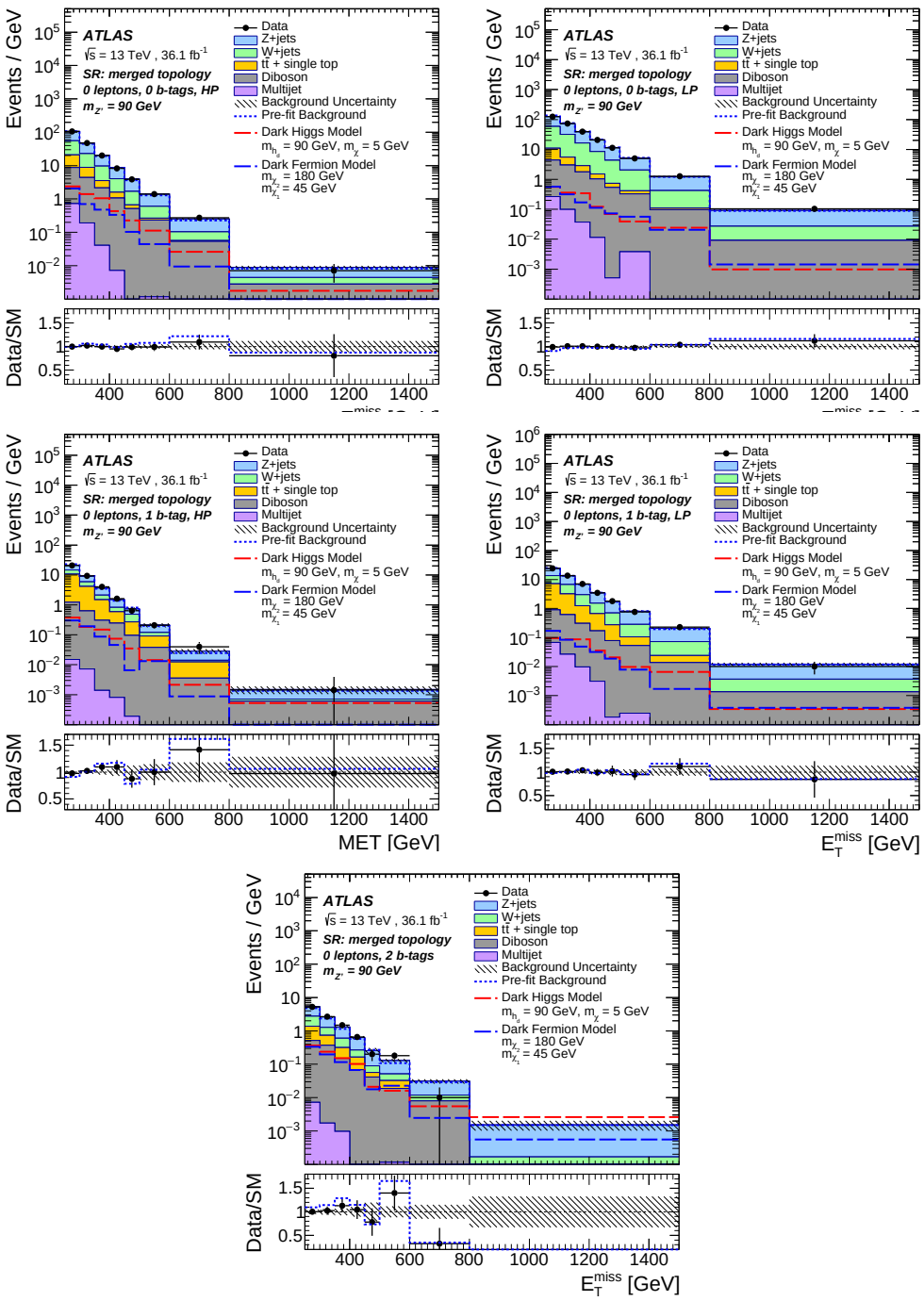

Figure 5.7: The observed (dots) and expected (histograms) distributions of missing transverse momentum, $E_{\mathrm{T}}^{\mathrm{miss}}$, obtained with 36.1 fb^{-1}of data at $\sqrt{s} = 13$ TeV in the mono-Z' signal region with $m_{Z'} = 90$ GeV and the merged event topology after the profile likelihood fit (with $\mu = 0$), shown separately for the (a) 0b-HP, (b) 0b-LP, (c) 1b-HP, (d) 1b-LP, and (e) 2b-tag event categories. The total background contribution before the fit to data is shown as a dotted blue line. The hatched area represents the total background uncertainty. The expectations for the selected dark-Higgs (dashed red line) and dark-fermion (dashed blue line) signal points are shown for comparison. The inset at the bottom of each plot shows the ratio of the data to the total post-fit (dots) and pre-fit (dotted blue line) background expectation.

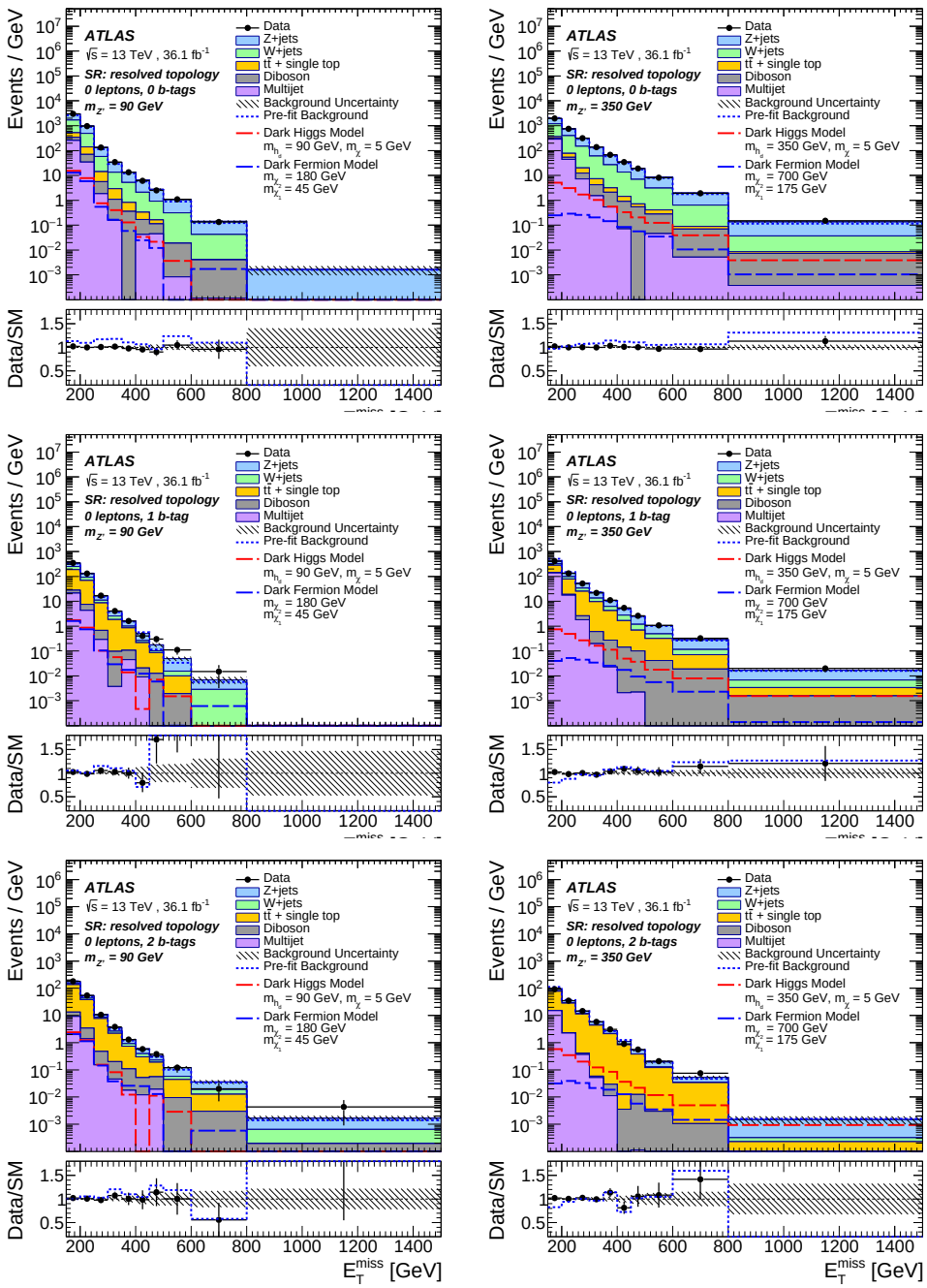

Figure 5.8: The observed (dots) and expected (histograms) distribution of missing transverse momentum, $E_{\mathrm{T}}^{\mathrm{miss}}$, obtained with 36.1 fb^{-1}of data at $\sqrt{s} = 13$ TeV in the mono-Z' signal region with the resolved event topology after the profile likelihood fit (with $\mu = 0$), shown separately for the (a,b) 0b, (c,d) 1b and (e,f) 2b-tag event categories. On the left-hand side, the mediator mass of 90 GeV and on the right-hand side of 350 GeV is assumed. The total background contribution before the fit to data is shown as a dotted blue line. The hatched area represents the total background uncertainty. The expectations for the selected dark-Higgs (dashed red line) and dark-fermion (dashed blue line) signal points are shown for comparison. The inset at the bottom of each plot shows the ratio of the data to the total post-fit (dots) and pre-fit (dotted blue line) background expectation.

Table 5.4: The expected and observed numbers of events for an integrated luminosity of 36.1 fb^{-1} and $\sqrt{s} = 13$ TeV, shown separately in each mono-Z' signal region category assuming $m_{Z'} = 90$ GeV. The background yields and uncertainties are shown after the profile likelihood fit to the data (with $\mu = 0$). The quoted background uncertainties include both the statistical and systematic contributions, while the uncertainty in the signal is statistical only. The uncertainties in the total background can be smaller than those in individual components due to anti-correlations of nuisance parameters.

			Merged topology		
Process	0b-HP	0b-LP	1b-HP	1b-LP	2b
Dark fermion, light sector	286 ± 54	125 ± 36	53 ± 23	26 ± 16	52 ± 23
Dark fermion, heavy sector	165 ± 18	71 ± 12	30.9 ± 7.7	18.6 ± 6.0	36.3 ± 8.4
Dark Higgs, light sector	253 ± 25	82 ± 14	37.7 ± 9.6	19.1 ± 6.9	45 ± 11
Dark Higgs, heavy sector	224 ± 14	75.9 ± 8.4	37.5 ± 5.9	21.2 ± 4.4	49.5 ± 6.8
W+jets	2960 ± 170	5180 ± 280	342 ± 52	680 ± 100	120 ± 120
Z+jets	4720 ± 190	7990 ± 310	628 ± 69	1280 ± 140	265 ± 22
$t\bar{t}$	780 ± 110	440 ± 59	646 ± 59	434 ± 49	59 ± 19
Single top-quark	161 ± 15	113 ± 14	93 ± 10	94.1 ± 8.9	17.8 ± 2.8
Diboson	830 ± 130	575 ± 95	129 ± 23	107 ± 18	61 ± 11
Multijet	48 ± 41	21 ± 66	1.2 ± 1.0	5.4 ± 5.1	0.52 ± 0.51
Total background	9498 ± 96	14310 ± 120	1840 ± 37	2600 ± 46	523 ± 19
Data	9516	14282	1845	2628	534
			Resolved topology		
Process	0b		1b		2b
Dark fermion, light sector	2060 ± 150		264 ± 52		228 ± 55
Dark fermion, heavy sector	976 ± 44		121 ± 15		164 ± 18
Dark Higgs, light sector	1206 ± 54		135 ± 18		197 ± 22
Dark Higgs, heavy sector	953 ± 30		112 ± 10		146 ± 12
W+jets	78400 ± 3400		4400 ± 690		1030 ± 190
Z+jets	91700 ± 3800		6970 ± 690		2140 ± 210
$t\bar{t}$	11170 ± 920		10590 ± 530		7760 ± 230
Single top-quark	1200 ± 170		1006 ± 74		602 ± 40
Diboson	6080 ± 930		514 ± 80		337 ± 55
Multijet	14700 ± 2500		1280 ± 540		540 ± 270
Total background	203990 ± 480		24770 ± 220		12400 ± 110
Data	203991		24783		12406

5.8.3 Constraints on invisible Higgs boson decays

In the search for invisible Higgs boson decays, an observed (expected) upper limit of 0.83 ($0.58^{+0.23}_{-0.16}$) is obtained at 95% CL on the branching ratio $\mathcal{B}_{H\to\text{inv.}}$, assuming the SM production cross sections and combining the contributions from VH, ggH and VBF production modes. The expected limit is a factor of about 1.5 better (while the observed is slightly

Table 5.5: The expected and observed numbers of events for an integrated luminosity of 36.1 fb^{-1} and $\sqrt{s} = 13$ TeV, shown separately in each mono-Z' signal region category assuming $m_{Z'} = 350$ GeV. The background yields and uncertainties are shown after the profile likelihood fit to the data (with $\mu = 0$). The quoted background uncertainties include both the statistical and systematic contributions, while the uncertainty in the signal is statistical only. The uncertainties in the total background can be smaller than those in individual components due to anti-correlations of nuisance parameters.

	Resolved topology		
Process	$0b$	$1b$	$2b$
Dark fermion, light sector	655 ± 14	104.2 ± 5.8	89.5 ± 5.3
Dark fermion, heavy sector	70.79 ± 0.79	12.45 ± 0.33	9.04 ± 0.28
Dark Higgs, light sector	639 ± 13	96.7 ± 4.9	72.3 ± 4.3
Dark Higgs, heavy sector	118.9 ± 1.4	19.62 ± 0.58	14.24 ± 0.50
W+jets	68300 ± 4300	4270 ± 1100	115 ± 84
Z+jets	72200 ± 3000	7230 ± 800	1160 ± 110
$t\bar{t}$	3900 ± 460	10320 ± 720	4920 ± 140
Single top-quark	752 ± 69	1530 ± 110	466 ± 35
Diboson	2000 ± 340	282 ± 47	14.6 ± 2.8
Multijet	17100 ± 2300	7870 ± 390	880 ± 140
Total background	164310 ± 650	31520 ± 250	7567 ± 85
Data	164386	31465	7597

worse) than the one reached by the previous analysis of Run 1 ATLAS data [168].

5.8.4 Constraints on the simplified vector-mediator model

In the context of the mono-W/Z simplified vector-mediator signal model, the exclusion limits on the signal strength are shown in Figure 5.9 and translated into limits on the dark matter and mediator masses (Figure 5.9) for Dirac DM particles and couplings $g_{\mathrm{SM}} = 0.25$ and $g_{\mathrm{DM}} = 1$. Since only a limited number of signal points were simulated, an interpolation procedure is employed to obtain the limits on the signal strength at other mass points in the $(m_\chi, m_{Z'})$ parameter plane. All signal processes with the same mediator mass $m_{Z'}$ and different m_χ values are assumed to have the same $(\mathcal{A}\times\varepsilon)_{\mathrm{total}}$ value as in the simulated sample

Table 5.6: Breakdown of expected signal strength uncertainties for several mono-W/Z and mono-Z' signal models, obtained for an integrated luminosity of 36.1 fb^{-1} and $\sqrt{s} = 13$ TeV. A dark matter mass of 1 GeV is used for the two vector-mediator signals. Each systematic uncertainty contribution is determined from the quadratic difference between the total uncertainty and the uncertainty obtained by neglecting the systematic uncertainty source in question. Only the largest systematic uncertainties are shown.

Source of uncertainty	Uncertainty on μ =1 [%]				
	Vector mediator, $m_{Z'}$ =		$H \rightarrow$invisible	Dark fermion, $m_{Z'}$ =	
	200 GeV	600 GeV	($\mathcal{B}_{H\rightarrow\text{inv.}} = 100\%$)	90 GeV	350 GeV
Large-R jets	9	20	17	23	–
Small-R jets	3	8	7	13	7
Electrons	4	9	6	7	6
Muons	6	7	7	15	11
$E_{\text{T}}^{\text{miss}}$	1	4	3	4	3
b-tagging (track jets)	4	4	4	8	–
b-tagging (small-R jets)	2	4	2	5	5
Luminosity	3	4	3	4	4
Multijet normalization	7	11	11	13	6
Diboson normalization	5	11	6	3	1
Z+jets normalization	5	9	4	15	9
W+jets normalization	3	4	2	8	6
$t\bar{t}$ normalization	3	1	0.3	8	5
Signal modelling	7	9	20	–	–
V+jets modelling	4	10	4	7	11
$t\bar{t}$ modelling	2	4	3	10	6
V+jets flavour composition	1	3	3	4	2
Diboson modelling	1	2	2	1	0.2
Background MC stat.	10	18	14	20	12
Total syst.	21	40	38	45	29
Data stat.	7	21	5	14	12
Total	22	45	39	47	32

with $m_\chi = 1$ GeV. This was verified to be a reliable approximation for $m_{Z'} > 2m_\chi$. Thus, the expected signal yield at a given mass point $(m_{Z'}, m_\chi)$ only depends on the cross section $\sigma^{(m_{Z'},m_\chi)}_{pp\to Z'\to\chi\chi}$ at that mass point. Under the narrow width approximation, this cross section can be expressed in terms of the cross section $\sigma^{(m_{Z'},m_\chi=1\text{ GeV})}_{pp\to Z'\to\chi\chi}$ and the branching ratio $\mathcal{B}^{m_\chi=1\text{ GeV}}_{Z'\to\chi\chi}$ at the simulated mass point with $m_\chi = 1$ GeV,

$$\sigma^{(m_{Z'},m_\chi)}_{pp\to Z'\to\chi\chi} = \sigma^{(m_{Z'},m_\chi=1\text{ GeV})}_{pp\to Z'\to\chi\chi} \cdot \frac{\mathcal{B}^{m_\chi}_{Z'\to\chi\chi}}{\mathcal{B}^{m_\chi=1\text{ GeV}}_{Z'\to\chi\chi}},$$

where the value of the branching ratio $\mathcal{B}^{m_\chi}_{Z'\to\chi\chi}$ is fully defined by the values of model parameters g_{DM}, g_{SM}, m_χ and $m_{Z'}$. For the given coupling choices, vector-mediator masses $m_{Z'}$ of up to 650 GeV are excluded at 95% CL for dark matter masses m_χ of up to 250 GeV, agreeing well with the expected exclusion of Z' masses of up to 700 GeV for m_χ of up to 230 GeV. The expected limits are improved by 15–30%, depending on the DM mass, compared to the analysis presented in Ref. [243].

5.8.5 Mono-W/Z constraints with reduced model dependence

In addition to the interpretation of the mono-W/Z search in terms of the simplified vector-mediator model and invisible Higgs boson decays, the analysis results are also expressed in terms of generic CL_s upper limits at 95% CL on the allowed visible cross section σ_{vis} of potential $W + \text{DM}$ or $Z + \text{DM}$ production. The limits on these two processes are evaluated separately to allow more flexibility in terms of possible reinterpretations, as new models might prefer one of these two final states. The exclusion limits are provided in the fiducial region that is defined by applying all signal region selection criteria except for the requirements on m_{jj} or m_J and the b-tagging multiplicity. With this definition, the exclusion limits on σ_{vis} apply to any processes which are characterized by a generic back-to-back topology with a W/Z boson recoiling against $E_{\text{T}}^{\text{miss}}$ from weakly interacting particles such as DM. The limits

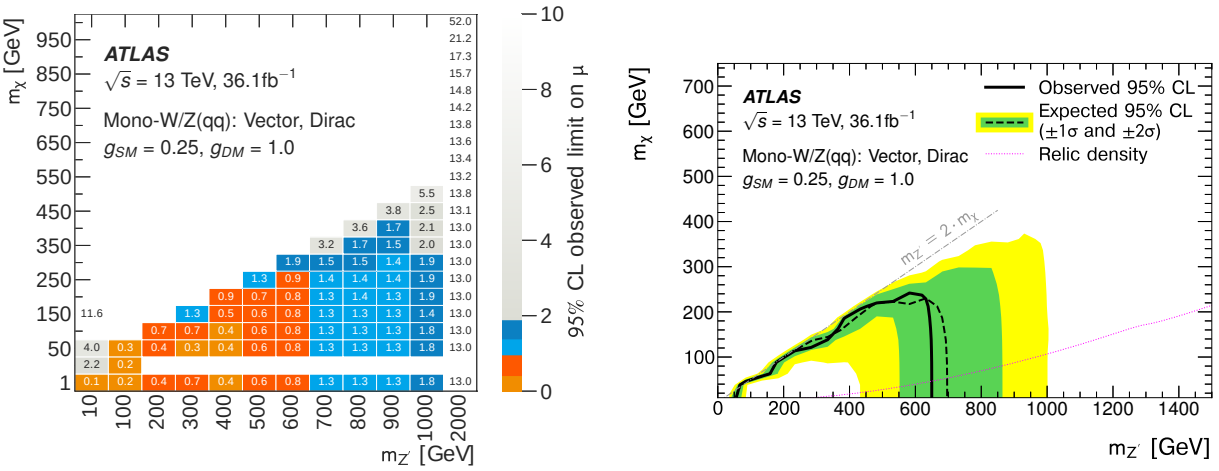

Figure 5.9: (a) Observed upper limits on the signal strength μ at 95% CL in the grid of the DM and mediator particle masses, (m_χ, $m_{Z'}$), for the combined mono-W and mono-Z search in the simplified vector-mediator model with Dirac DM particles and couplings $g_{\mathrm{SM}} = 0.25$ and $g_{\mathrm{DM}} = 1$. There are no interpolated points and thus no limit values listed for the mass point ($m_\chi = 100$ GeV, $m_{Z'} = 10$ GeV) and in the parameter region ($m_\chi = 10$ GeV, $m_{Z'} = 200$–2000 GeV). (b) The corresponding exclusion contours at 95% CL. The black solid (dashed) curve shows the observed (expected) limit. The dotted magenta curve corresponds to the set of points for which the expected relic density is consistent with the WMAP [169] and Planck [170] measurements ($\Omega h^2 = 0.12$), as computed with MadDM [171]. The region below the curve corresponds to higher predicted relic abundance than these measurements.

on σ_{vis} are given as a function of the $E_{\text{T}}^{\text{miss}}$ variable in order to avoid any additional model-dependent assumptions on the $E_{\text{T}}^{\text{miss}}$ distribution. Hence, the $E_{\text{T}}^{\text{miss}}$ bins in the zero-lepton region are treated independently of each other in the statistical interpretation of the data. A reduced number of bins is used for $E_{\text{T}}^{\text{miss}} > 300$ GeV to reduce the statistical uncertainty in the per-bin analysis. In all other aspects, the approach is identical to the mono-W/Z analysis described above. The mono-W/Z vector-mediator signal samples are used as a benchmark model to estimate the residual dependence of the σ_{vis} limits on the kinematic properties of events within a given $E_{\text{T}}^{\text{miss}}$ range and on the b-tagging multiplicity. For this, a wide range of $(m_{Z'}, m_{\chi})$ model parameters that yield a sizeable contribution of at least 500 simulated events in a given $E_{\text{T}}^{\text{miss}}$ range is considered. Corresponding variations of 15–50% (25–50%) in the expected limits on $\sigma_{\text{vis},\, W+\text{DM}}$ ($\sigma_{\text{vis},\, Z+\text{DM}}$) are found. The weakest σ_{vis} limit is quoted in a given range of reconstructed $E_{\text{T}}^{\text{miss}}$ in order to minimize the dependence on a benchmark model. The observed and expected limits on σ_{vis} in each $E_{\text{T}}^{\text{miss}}$ range are shown in Figure 5.10, with the numerical values summarized in Tables 5.7 and 5.8. As a general trend, the limits on $Z+\text{DM}$ production are somewhat stronger than those on $W+\text{DM}$ since the former contributes significantly to the $2b$ category that has the highest sensitivity due to having the lowest SM background.

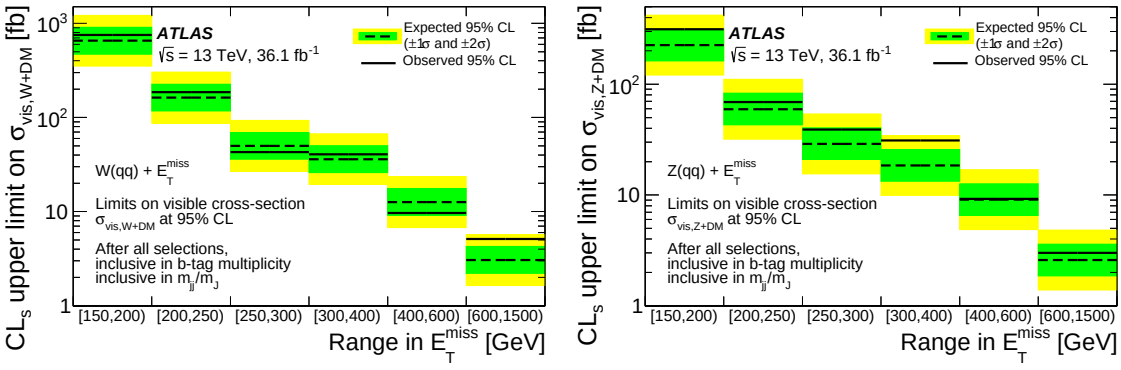

Figure 5.10: Upper limits at 95% CL on the visible cross section $\sigma_{\text{vis},\, W+\text{DM}}$ (left) and $\sigma_{\text{vis},\, Z+\text{DM}}$ (right) in the six $E_{\text{T}}^{\text{miss}}$ regions, after all selection requirements, but inclusive in the b-tag multiplicity and the W/Z candidate mass m_{jj}/m_J. The observed limits (solid line) are consistent with the expectations under the SM-only hypothesis (dashed line) within uncertainties (filled bands).

Table 5.7: The observed and expected exclusion limit at 95% CL on σ_{vis} for W + DM production for an integrated luminosity of 36.1 fb^{-1} and $\sqrt{s} = 13$ TeV, together with the corresponding product of acceptance and efficiency ($A \times \varepsilon$) for different regions of $E_{\text{T}}^{\text{miss}}$.

$E_{\text{T}}^{\text{miss}}$ range [GeV]	Upper limit at 95% CL [fb] $\sigma_{\text{vis}}^{\text{obs}}$	$\sigma_{\text{vis}}^{\text{exp}}$	-1σ	$+1\sigma$	$A \times \varepsilon$
W+DM, $W \to q'q$					
[150, 200]	750	650	470	910	20%
[200, 250]	185	163	117	226	20%
[250, 300]	43	50	36	69	30%
[300, 400]	41	36	26	50	45%
[400, 600]	9.7	12.6	9.1	17.6	55%
[600, 1500]	5.1	3.1	2.2	4.3	55%

Table 5.8: The observed and expected exclusion limit at 95% CL on σ_{vis} for Z + DM production for an integrated luminosity of 36.1 fb^{-1} and $\sqrt{s} = 13$ TeV, together with the corresponding product of acceptance and efficiency ($A \times \varepsilon$) for different regions of $E_{\text{T}}^{\text{miss}}$.

$E_{\text{T}}^{\text{miss}}$ range [GeV]	Upper limit at 95% CL [fb] $\sigma_{\text{vis}}^{\text{obs}}$	$\sigma_{\text{vis}}^{\text{exp}}$	-1σ	$+1\sigma$	$A \times \varepsilon$
Z+DM, $Z \to q\bar{q}$					
[150, 200]	313	225	162	314	20%
[200, 250]	69	60	43	83	20%
[250, 300]	39	29	21	40	30%
[300, 400]	31.1	18.5	13.3	25.7	45%
[400, 600]	9.2	9.1	6.5	12.6	50%
[600, 1500]	3.0	2.6	1.9	3.6	55%

The observable σ_{vis} can be interpreted as

$$\begin{aligned}
\sigma_{\text{vis, }W+\text{DM}}(E_{\text{T}}^{\text{miss}}) &\equiv \sigma_{W+\text{DM}}(E_{\text{T}}^{\text{miss}}) \times \mathcal{B}_{W\to q'q} \times (A \times \varepsilon)(E_{\text{T}}^{\text{miss}}) \quad \text{for } W + \text{DM events}\,, \\
\sigma_{\text{vis, }Z+\text{DM}}(E_{\text{T}}^{\text{miss}}) &\equiv \sigma_{Z+\text{DM}}(E_{\text{T}}^{\text{miss}}) \times \mathcal{B}_{Z\to q\bar{q}} \times (A \times \varepsilon)(E_{\text{T}}^{\text{miss}}) \quad \text{for } Z + \text{DM events}\,,
\end{aligned}$$

where $\sigma_{W+\text{DM}}$ ($\sigma_{Z+\text{DM}}$) is the production cross section for W+DM (Z+DM) events in a given $E_{\text{T}}^{\text{miss}}$ range, $\mathcal{B}_{W\to q'q}$ ($\mathcal{B}_{Z\to q\bar{q}}$) is the branching ratio for the hadronic W (Z) boson decay, and $(A \times \varepsilon)(E_{\text{T}}^{\text{miss}})$ is the product of the kinematic acceptance and the experimental efficiency. This product represents the fraction of simulated $W/Z + \text{DM}$ events in a given $E_{\text{T}}^{\text{miss}}$ range at parton level[1] that fall into the same $E_{\text{T}}^{\text{miss}}$ range at detector level after reconstruction, and pass the event selection criteria applied to determine σ_{vis}. To allow a generic interpretation, the requirements on m_{jj}/m_J or b-tagging are not included in the latter. The product $(A \times \varepsilon)(E_{\text{T}}^{\text{miss}})$ in a given $E_{\text{T}}^{\text{miss}}$ range has been evaluated for each simulated vector-mediator signal and the lowest of these values, rounded down in steps of 5%, has been taken for the limit calculation. The values obtained for each $E_{\text{T}}^{\text{miss}}$ range are listed in Tables 5.7 and 5.8.

5.8.6 Constraints on mono-Z' models

For the mono-Z' models, the upper limits on the cross section times the branching ratio $\mathcal{B}_{Z'\to q'q}$ at 95% CL are shown in Figure 5.11 as a function of the mediator mass for both the dark-fermion and dark-Higgs models in the light and heavy dark-sector mass scenarios. The largest excess of the data above the expectation, corresponding to a local significance of 3σ, is observed for a hypothesized signal at $m_{Z'} = 350$ GeV within the dark fermion model in the heavy dark-sector scenario. Taking into account the look-elsewhere effect [172] with respect

[1] At parton level, $E_{\text{T}}^{\text{miss}}$ is defined as the vector sum of momenta of neutrinos and DM particles in the transverse detector plane.

to the 19 overlapping mass windows examined in the mono-Z' search, the excess corresponds to a global significance of 2.2σ. Cross-section exclusion limits for the dark-fermion model (dark-Higgs model) in the light and the heavy dark-sector scenario are in the range of 0.68–27 pb and 0.066–9.8 pb (0.80–5.5 pb and 0.064–2.4 pb) respectively, for Z' masses between 80 and 500 GeV. The corresponding observed and expected upper limits on the coupling

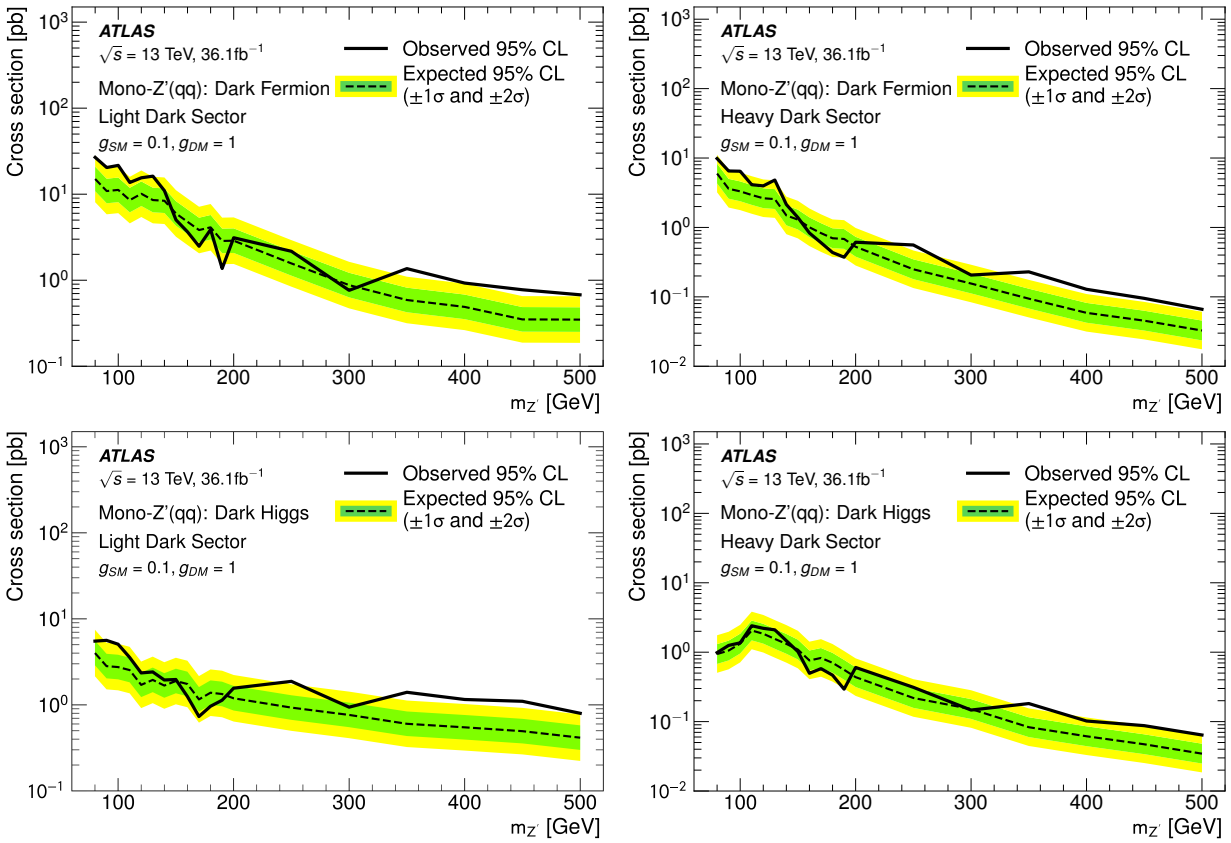

Figure 5.11: Upper limits at 95% CL on the cross section times the branching ratio $\mathcal{B}_{Z'\to q'q}$ in mono-Z' models as a function of the mediator mass, $m_{Z'}$, for the dark fermion model in the (a) light and (b) heavy dark-sector scenario, as well as the dark Higgs model in the (c) light and (d) heavy dark-sector scenario.

g_{SM} are shown in Figure 5.12, assuming $g_{\mathrm{DM}} = 1$.

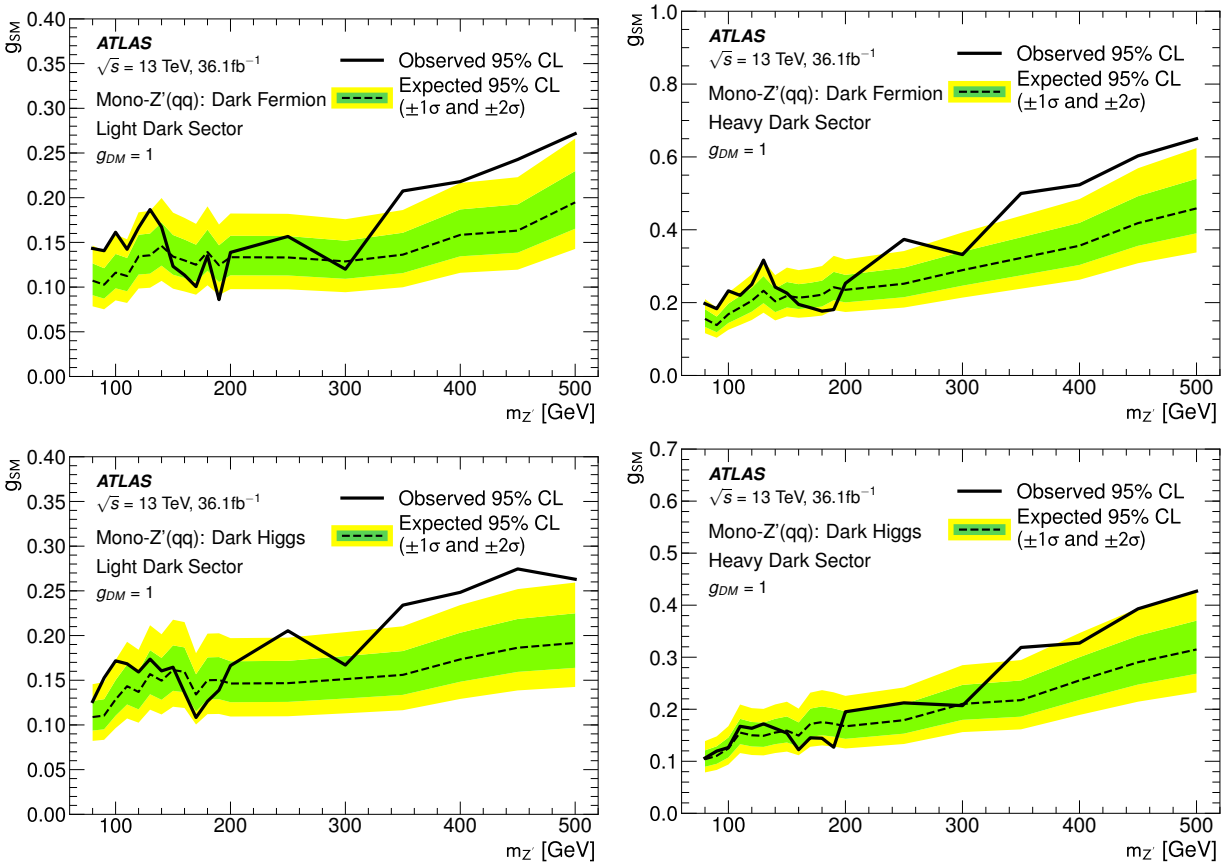

Figure 5.12: Upper limits at 95% CL on the product of couplings g_{SM} g_{DM} in mono-Z' models as a function of the mediator mass for the dark fermion model in the (a) light and (b) heavy dark-sector scenario, as well as the dark Higgs model in the (c) light and (d) heavy dark-sector scenario.

5.9 Summary

A search for dark matter was performed in events having a large-R jet or a pair of small-R jets compatible with a hadronic W or Z boson decay, and large $E_{\mathrm{T}}^{\mathrm{miss}}$. In addition, the as of yet unexplored hypothesis of a new vector boson Z' produced in association with dark matter is considered. This search uses the ATLAS dataset corresponding to an integrated luminosity of 36.1 fb^{-1} of $\sqrt{s} = 13$ TeV pp collisions collected at the LHC in 2015 and 2016. It improves on previous searches by virtue of the larger dataset and further optimization of the selection criteria and signal region definitions. The results are in agreement with the SM predictions and are translated into exclusion limits on DM-pair production.

Two simplified models are considered to describe DM production in the mono-W/Z final state. For the simplified vector-mediator model in which the DM is produced via an s-channel exchange of a vector mediator Z', masses $m_{Z'}$ of up to 650 GeV are excluded for dark matter masses m_{χ} of up to 250 GeV (assuming $g_{\mathrm{SM}} = 0.25$ and $g_{\mathrm{DM}} = 1.0$). This agrees well with the expected exclusion of $m_{Z'}$ values of up to 700 GeV for m_{χ} of up to 230 GeV. Limits are also placed on the visible cross section of non-SM events with large $E_{\mathrm{T}}^{\mathrm{miss}}$ and a W or a Z boson without extra model assumptions. In the search for invisible Higgs boson decays, an upper limit of 0.83 is observed at 95% CL on the branching ratio $\mathcal{B}_{H\to\mathrm{inv.}}$, while the corresponding expected limit is 0.58.

Two additional signal models, for DM production in association with the non-SM vector boson Z', are considered. In the dark-fermion model, the intermediate Z' boson couples to a heavier dark-sector fermion χ_2 as well as the lighter DM candidate fermion χ_1. In the dark-Higgs model, a dark-sector Higgs boson which decays to a $\chi\chi$ pair is radiated from the Z' boson. For coupling values of $g_{\mathrm{SM}} = 0.1$ and $g_{\mathrm{DM}} = 1.0$, two different choices of masses m_{χ_2} and m_{h_D} of intermediate dark-sector particles are considered. Cross-section exclusion limits for the dark-fermion model in the light and heavy dark-sector scenarios are in the range

of 0.68–27 pb and 0.066–9.8 pb respectively for Z' masses between 80 and 500 GeV. The corresponding limits for the dark-Higgs model in the light and heavy dark-sector scenario are 0.80–5.5 pb and 0.064–2.4 pb, respectively.

Chapter 6

Jet Substructure

6.1 Introduction

Collisions at the LHC occur at such high energies that even massive particles are produced at large enough velocities that their decay products become collimated. In the case of a hadronic decay of a boosted W boson ($W \to qq'$), the two jets produced from these two quarks then overlap in the detector, creating a single merged jet. The substructure of the jet's energy deposition can distinguish between jets which are due to a single hadronic particle or due to the decay of a massive object into multiple hadronic particles; this classification is known as jet "tagging" and is critical for understanding the nature of the particles produced in the collision [173].

This classification task has been the topic of intense research activity [174, 175, 176, 177]. The difficult nature of the problem has lead physicists to reduce the dimensionality of the problem by designing expert features [178, 179, 180, 181, 182, 183, 184, 185, 186, 187] which incorporate their domain knowledge. In the current state of the art applications, jets are either classified based on one of these features alone or by combining multiple designed fea-

tures with shallow machine learning classifiers such as boosted decision trees (BDTs). It is possible, however, that these designed expert features do not capture all of the available information [188, 189, 190], as the data are very high-dimensional and despite extensive theoretical progress in the microphysics of jet formation [191, 192, 193] and the existence of effective simulation tools [194, 195], there exists no complete analytical model for classification directly from theoretical principles, though see Ref. [196]. Therefore, approaches that use the higher-dimensional but lower-level detector information to learn this classification function may outperform those which rely on fewer high-level expert-designed features.

Measurements of the emanating particles can be projected onto a cylindrical detector and then unwrapped and considered as two-dimensional images, enabling the natural application of computer vision techniques. Recent work demonstrates encouraging results with shallow classification models trained on jet images [197, 198, 199]. Deep networks have shown additional promise in particle-level studies [200]. However, deep learning has not yet been applied to more realistic scenarios which include simulation of the detector response and resolution, and most importantly, the effect of unrelated simultaneous pp interactions, known as *pileup* which contributes significant energy depositions unrelated to the particles of interest.

In this chapter, we perform jet classification on images built from simulated detector response using deep neural network models with a combination of locally-connected and fully-connected layers. Our results demonstrate that deep networks can distinguish between detector clusters due to single or multiple jets without using domain knowledge, matching or exceeding the performance of shallow classifiers used to combine many expert features.

6.2 Theory

A typical application of jet classifiers is to discriminate single jets produced in quark or gluon fragmentation from two overlapping jets produced when a high-velocity W boson decays to a collimated pair of quarks. The goal is then to learn the classification function, or equivalently, the likelihood ratio:

$$\frac{P_{W\to qq}(\text{jet})}{P_{q/g}(\text{jet})}$$

In practice, there are two significant obstacles to calculating and applying this ratio.

First, while theoretical understanding of the processes involved has made significant progress, a formulation of this likelihood ratio from fundamental QCD principles is not yet available. However, there do exist effective models which have been successfully incorporated into widely used tools capable of generating simulated samples. Such samples can then be used to deduce the likelihood ratio, but the task is very difficult due to its high-dimensionality. Expert features with solid theoretical grounding exist to reduce the dimensionality of this problem, but it is unlikely that they capture all of the information, as the theoretical understanding is not complete and the concepts which motivate them do not include the detector effects or the impact of pileup interactions. The goal of this chapter is to attempt to capture as much of the information as possible and learn the classification function from simulated samples which include these effects, without making the simplifying theoretical assumptions necessary to construct expert features.

Second, the effective models used in simulation tools do not provide a perfectly accurate description of observed collider data. A classification function learned from simulated samples

is limited by the validity of those samples. While deep networks may provide a powerful method of deducing the classification function, expert features which encapsulate theoretical understanding of the process of jet formation are valuable in assessing the success and failure of these models. In this chapter, we use expert features as a benchmark to measure the performance of learning tools which access only the higher-dimensional lower-level data. We expect that deep networks may provide additional classification power in concert with the insight offered by expert features, and perhaps motivate the development of modifications to such features rather than blindly replacing them.

6.3 Data

Training samples for both classes were produced using realistic simulation tools widely used in particle physics.

Samples of boosted $W \to qq'$ were generated with a center of mass energy $\sqrt{s} = 14$ TeV using the diboson production and decay process $pp \to W^+W^- \to qqqq$ leading to two pairs of quarks; each pair of quarks are collimated and lead to a single jet. Samples of jets originating from single quarks and gluons were generated using the $pp \to qq, qg, gg$ process. In both cases, jets are generated in the range of $p_{\mathrm{T}} \in [300, 400]$ GeV.

Collisions and immediate decays were simulated with MADGRAPH5 [201] v2.2.3, showering and hadronization simulated with PYTHIA [194] v6.426 , and response of the detectors simulated with DELPHES [202] v3.2.0. The jet images are characterized by the energies deposited at different points on the approximately cylindrical calorimeter surface.

The classification of jets as due to $W \to qq'$ or single quarks and gluons is sensitive to the presence of additional in-time pp interactions, referred to as *pile-up* events. We overlay such interactions in the simulation chain, with an average number of interactions per event of

$\langle\mu\rangle = 50$, as an estimate of future ATLAS Run 2 data with the LHC delivering collisions at a 25ns bunch crossing interval. The impact of pile-up events on jet reconstruction can be mitigated using several techniques. After reconstructing jets with the anti-k_{T} [203] clustering algorithm using distance parameter $R = 1.2$, we apply a jet-trimming algorithm [204] which is designed to remove pileup while preserving the two-pronged jet substructure characteristic of boson decay. Jet trimming re-clusters the jet constituents using the k_{T} [205] algorithm into subjets of radius 0.2 and discards subjets with p_{T} less than 3% of the original jet. Then the final trimmed jet is built using the remaining subjets. Trimmed jets with 300 GeV$< p_{\mathrm{T}} <$400 GeV are selected, in order to ensure the minimum W boson velocity needed for collimated decays. In principle, the machine learning algorithms may be able to classify jets without such filtering; we leave this for future studies.

To compare our approach to the current state-of-the-art, we calculate six high-level jet variables commonly used in the literature; calculations are performed using FastJet [206] v3.1.2. First, the invariant mass of the trimmed jet is calculated. Then, the trimmed jet's constituents are used to calculate the other substructure variables, N-subjettiness [181, 207] $\tau_{21}^{\beta=1}$, and the energy correlation functions [182, 208] $C_2^{\beta=1}$, $C_2^{\beta=2}$, $D_2^{\beta=1}$, and $D_2^{\beta=2}$. A comprehensive summary of these six jet substructure variables can be found in Ref. [174]. Figures 6.1 shows the distribution of the variables for the two classes of jets, both with and without pileup conditions.

In this chapter, we investigate the power of classification of the jets directly from the lower-level but higher-dimensional calorimeter data, without the dimensional reduction provided by the variables above. The strategy follows that of well-established image classification tools by treating the distribution of energy in the calorimeter as an image. The images were preprocessed as in previous work by centering and rotating into a canonical orientation. The origin of the coordinate axis was set at the center of energy of each jet, then the image was rotated so that the principle axis θ is in the same direction for each jet, where θ is defined

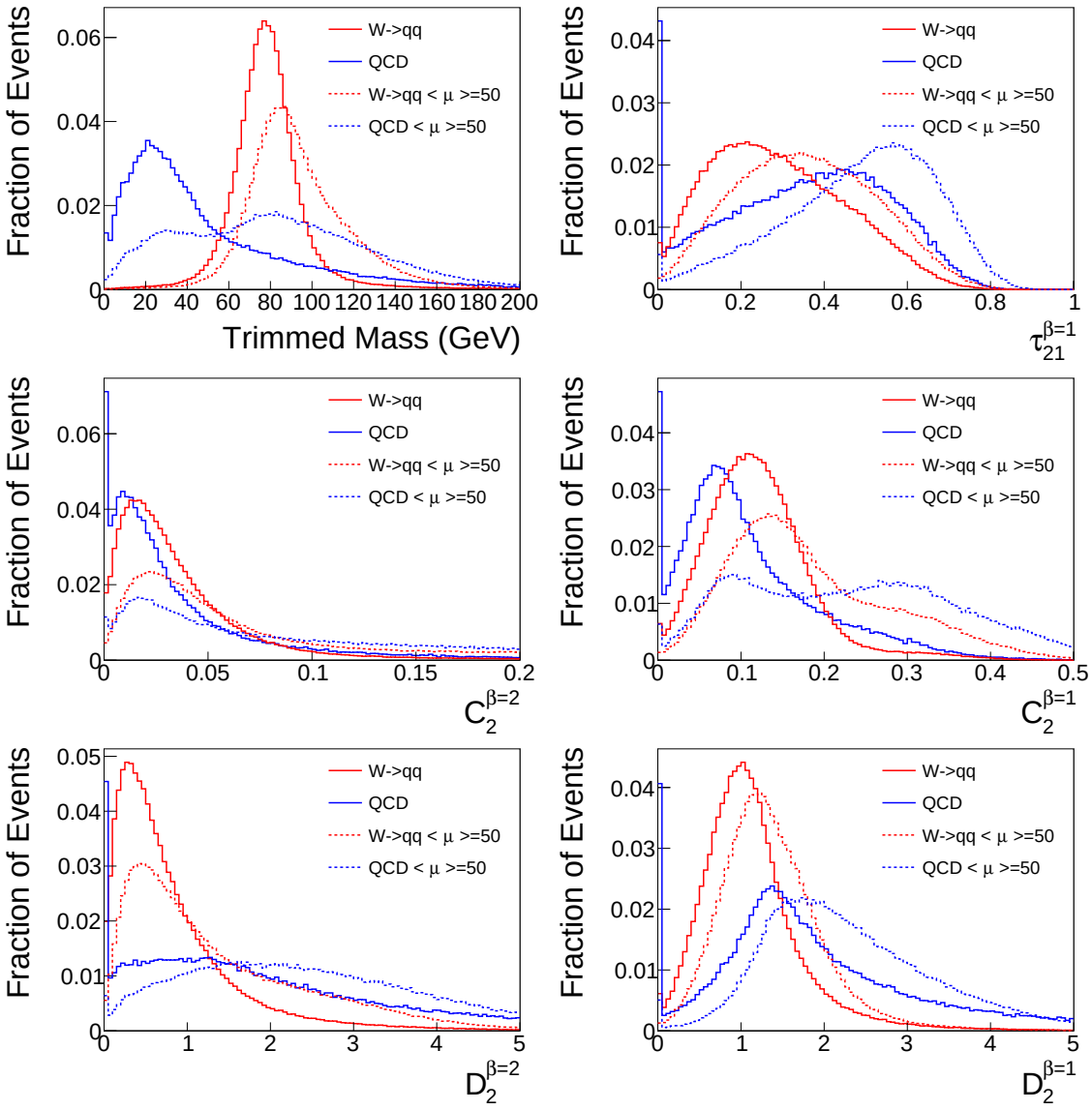

Figure 6.1: Distributions in simulated samples of high-level jet substructure variables widely used to discriminate between jets due to collimated decays of massive objects ($W \to qq$) and jets due to individual quarks or gluons (QCD). Two cases are shown: with and without the presence of additional in-time pp interactions, included at the level of an average of 50 such interactions per collision.

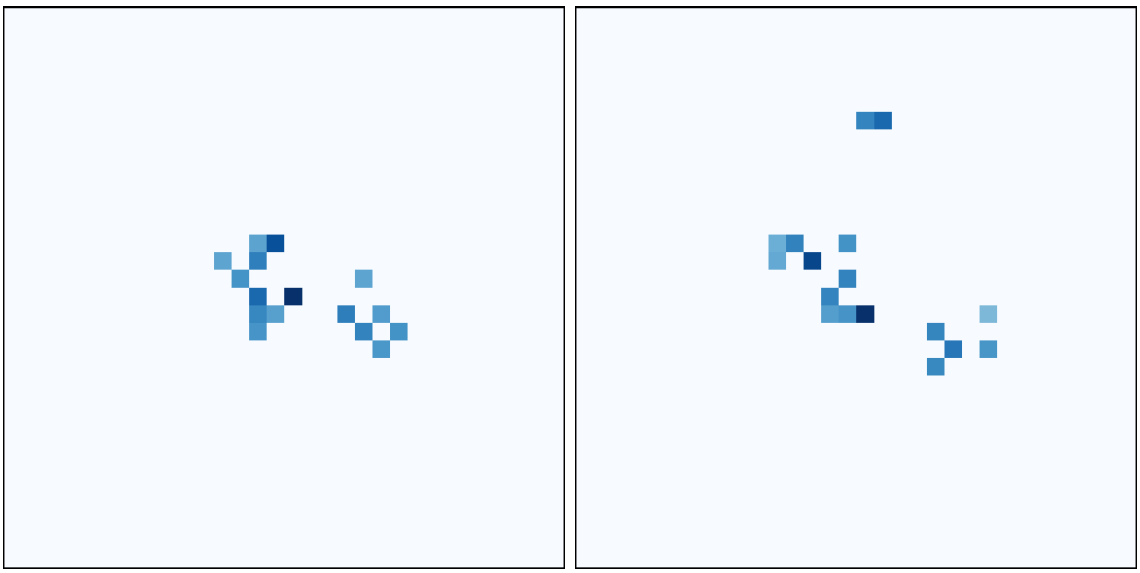

Figure 6.2: Typical jet images from class 1 (single QCD jet from q or g) on the left, and class 2 (two overlapping jets from $W \to qq'$) on the right, after preprocessing as described in the text.

as

$$\tan(\theta) = \sum_i \frac{\phi_i \times E_i}{R_i} \Big/ \sum_i \frac{\eta_i \times E_i}{R_i} \tag{6.1}$$

$$R_i = \sqrt{\eta_i^2 + \phi_i^2}. \tag{6.2}$$

Images are then reflected so that the maximum energy value is always in the top half of the image.

The jet energy deposits were centered and cropped to within a 3.0×3.0 radian window, then binned into pixels to form a 32×32 image, approximating the resolution of the calorimeter cells. When two calorimeter cells were detected within the same pixel, their energies were summed. Example individual jet images from each class are shown in Figure 6.2, and averages over many jets are shown in Figure 6.3.

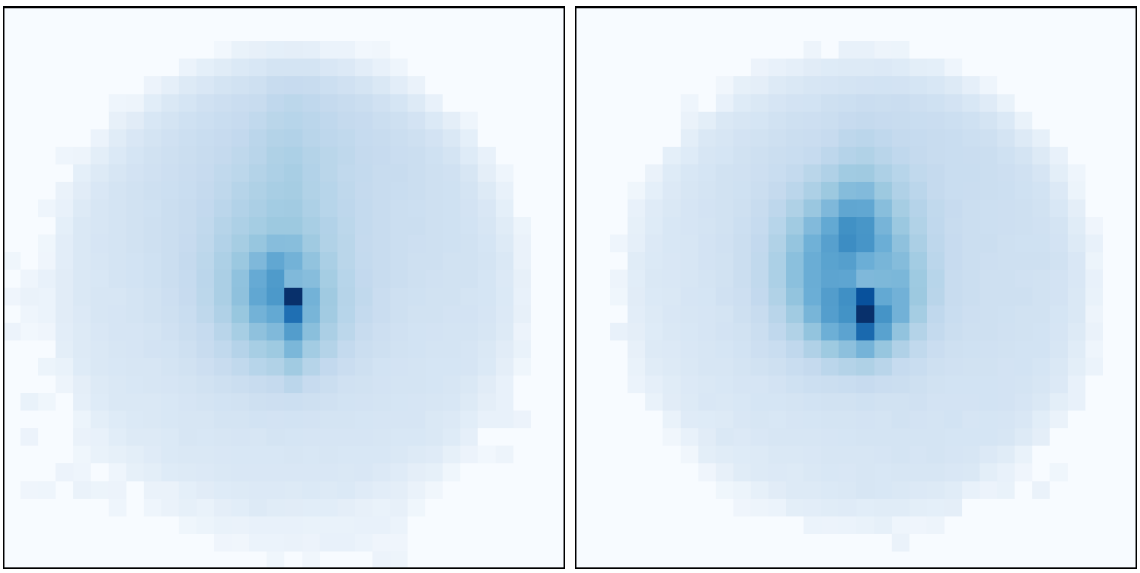

Figure 6.3: Average of 100,000 jet images from class 1 (single QCD jet from q or g) on the left, and class 2 (two overlapping jets from $W \to qq'$) on the right, after preprocessing.

6.4 Training

Deep neural networks were trained on the jet images and compared to the standard approach of BDTs trained on expert-designed variables that capture domain knowledge [174]. All classifiers were trained on a balanced training data set of 10 million examples, with 500 thousand of these used as a validation set. The best hyperparameters for each method were selected using the Spearmint Bayesian optimization algorithm [209] to optimize over the supports specified in Tables 6.1 and 6.2. The best models were then tested on a separate test set of 5 million examples.

Neural networks consisted of hidden layers of *tanh* units and a logistic output unit with cross-entropy loss. Weight updates were made using the ADAM optimizer [210] ($\beta_1 = 0.9, \beta_2 = 0.999, \epsilon = 1e-08$) with mini-batches of size 100. Weights were initialized from a normal distribution with the standard deviation suggested by Ref. [211]. The learning rate was initialized to 0.0001 and decreased by a factor of 0.9 every epoch. Training was stopped when the validation error failed to improve or after a maximum of 50 epochs. All

computations were performed using Keras [212] and Theano [213, 214] on NVidia Titan X processors. Convolutional networks were also explored, but as expected, the translational invariance provided by these architectures did not provide any performance boost.

We explore the use of locally-connected layers, where each neuron is only connected to a distinct 4-by-4 pixel region of the previous layer. This local connectivity constrains the network to learn spatially-localized features in the lower layers without assuming translational invariance, as in convolutional layers where the weights of the receptive fields are shared. Fully-connected layers were stacked on top of the locally-connected layers to aggregate information from different regions of the detector image. The network architecture — the number of layers of each type, plus the width of the fully-connected layers — was optimized using Spearmint. Out of the 25 network architectures explored on the no-pile-up task, the best had four locally-connected layers followed by four fully-connected layers of 425 units. This network has roughly 750,000 tunable parameters, while the best shallow network (one hidden layer of 1000 units) had over 1 million parameters. On the pile-up data, 19 different network architectures were tested; the best was again an 8-hidden-layer architecture, with 3 locally-connected layers, five fully-connected layers, and 500 hidden units in each layer.

BDTs were trained on the six high-level variables using Scikit-Learn [215]. The maximum depth of each estimator, the minimum number of examples required to constitute an internal node (parameterized as a fraction of the training set), and the learning rate were separately optimized for the datasets with and without pileup using Spearmint (110 and 140 experiments, respectively). The number of estimators was fixed to 500; when evaluating the marginal improvement of performance with the addition of each estimator, we observed that in the best model, performance plateaued after inclusion of less than 100 estimators. This suggests that the number of estimators was not limiting. The minimum number of examples required to form a leaf node was fixed to be one fourth of that required to constitute an internal node. In both cases, the best BDT classifier had a maximum tree depth of 49, a

minimum split requirement of 0.0021, and a learning rate of 0.07. The best BDT trained on the no-pileup data had approximately 700,000 tunable parameters, while the best BDT trained on the pileup data had approximately 750,000.

6.5 Results

Deep networks with locally-connected layers showed the best performance. For example, the best network with 5 hidden layers has two locally-connected layers followed by three fully-connected layers of 300 units each; this architecture performs better than a network of five fully-connected layers of 500 units each.

Final results are shown in Table 6.3. The metric used is the Area Under the Curve (AUC), calculated in signal efficiency versus background efficiency, where a larger AUC indicates better performance. In Fig 6.4, the signal efficiency is shown versus backround rejection, the inverse of background efficiency. In the case without pile-up, as studied in Ref. [200], the deep network modestly outperforms the physics domain variables, demonstrating first that successful classification can be performed without expert-designed features and that there is some loss of information in the dimensional reduction such features provide. See the discussion below, however, for comments on the continued importance of expert features.

Our results also demonstrate for the first time that such performance holds up under the more difficult and realistic conditions of many pileup interactions; indeed, the gap between the deep network and the expert variables in this case is more pronounced. This is likely due to the fact that the physics-inspired variables rest on arguments motivated by idealized pictures.

Table 6.1: Hyperparameter support for Bayesian optimization of deep neural network architectures. For the no-pileup case, networks with a single hidden layer were allowed to have up to 1000 units per layer, in order to remove the possibility of the deep networks performing better simply because they had more tunable parameters.

	Range		Optimum	
Hyperparameter	Min	Max	No pileup	Pileup
Hidden units per layer	100	500	425	500
Fully-connected layers	1	5	4	5
Locally-connected layers	0	5	4	3

Table 6.2: Hyperparameter support for BDTs trained on 6 high-level features, and the best combinations in 110 and 140 experiments, respectively, for the no-pileup and pileup tasks. Minimum leaf percent was constrained to be one fourth of the minimum split percent in all cases.

	Range		Optimum	
Hyperparameter	Min	Max	No pileup	Pileup
Tree depth	15	75	49	49
Learning rate	0.01	1.00	0.07	0.07
Minimum split percent	0.0001	0.1000	0.0021	0.0021

Table 6.3: Performance results for BDT and deep networks. Shown for each method are both the signal efficiency at background rejection of 10, as well as the Area Under the Curve (AUC), the integral of the background efficiency versus signal efficiency. For the neural networks, we report the mean and standard deviation of three networks trained with different random initializations.

	Performance	
Technique	Signal efficiency at bg. rejection=10	AUC
	No pileup	
BDT on derived features	86.5%	95.0%
Deep NN on images	$87.8\%_{(0.04\%)}$	$95.3\%_{(0.02\%)}$
	With pileup	
BDT on derived features	81.5%	93.2%
Deep NN on images	$84.3\%_{(0.02\%)}$	$94.0\%_{(0.01\%)}$

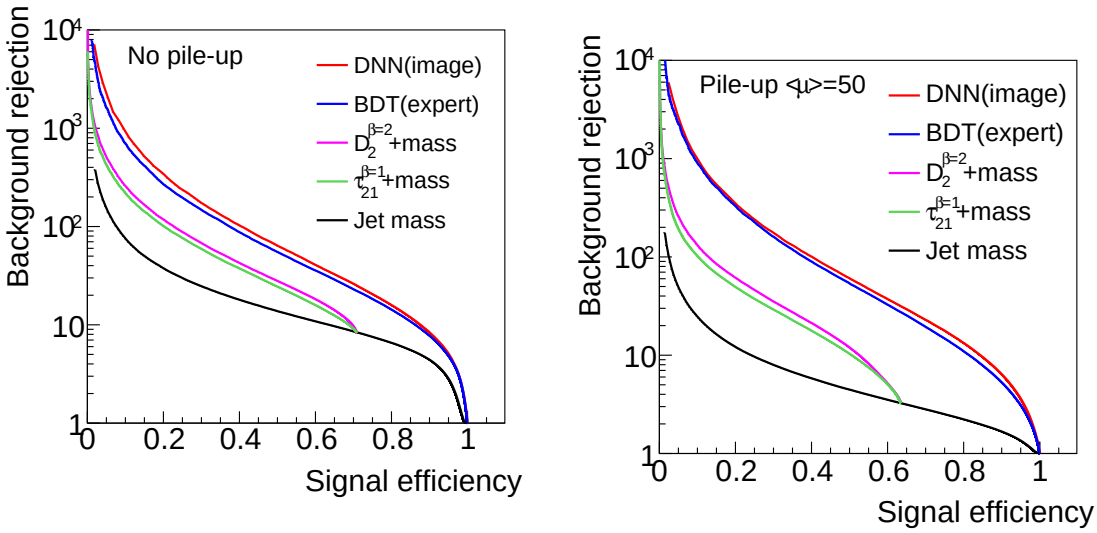

Figure 6.4: Signal efficiency versus background rejection (inverse of efficiency) for deep networks trained on the images and boosted decision trees trained on the expert features, both with (bottom) and without pile-up (top). Typical choices of signal efficiency in real applications are in the 0.5-0.7 range. Also shown are the performance of jet mass individually as well as two expert variables in conjunction with a mass window.

6.6 Interpretation

Current typical use in experimental analysis is the combination of the jet mass feature with τ_{21} or one of the energy correlation variables. Our results show that even a straightforward BDT-combination of all six of the high-level variables provides a large boost in comparison. In probing the power of deep learning, we then use as our benchmark this combination of the variables provided by the BDT.

The deep network has clearly managed to match or slightly exceed the performance of a combination of the state-of-the-art expert variables. Physicists working on the underlying theoretical questions may naturally be curious as to whether the deep network has learned a novel strategy for classification which could inform their studies, or rediscovered and further optimized the existing features.

While one cannot probe the motivation of the ML algorithm, it is possible to compare distributions of events categorized as signal-like by the different algorithms in order to understand how the classification is being accomplished. To compare distributions between different algorithms, we study simulated events with equivalent background rejection, see Figs. 6.5 and 6.6 for a comparison of the selected regions in the expert features for the two classifiers. The BDT preferentially selects events with values of the features close to the characteristic signal values and away from background-dominated values. The DNN, which has a modestly higher efficiency for the equivalent rejection, selects events near the same signal values, but in some cases can be seen to retains a slightly higher fraction of jets away from the signal-dominated region. The likely explanation is that the DNN has discovered the same signal-rich region identified by the expert features, but has in addition found avenues to optimize the performance and carve into the background-dominated region. Note that DNNs can also be trained to be independent of mass, by providing a range of mass in training, or training a network explicitly parameterized [216, 217] in mass.

6.7 Discussion

The signal from massive $W \to qq$ jets is typically obscured by a background from the copiously produced low-mass jets due to quarks or gluons. Highly efficient classification is critical, and even a small relative improvement in the classification accuracy can lead to a significant boost in the power of the collected data to make statistically significant discoveries. Operating the collider is very expensive, so particle physicists need tools that allow them to make the most of a fixed-size dataset. However, improving classifier performance becomes increasingly difficult as the accuracy of the classifier increases.

Physicists have spent significant time and effort designing features for jet-tagging classification tasks. These designed features are theoretically well motivated, but as their derivation

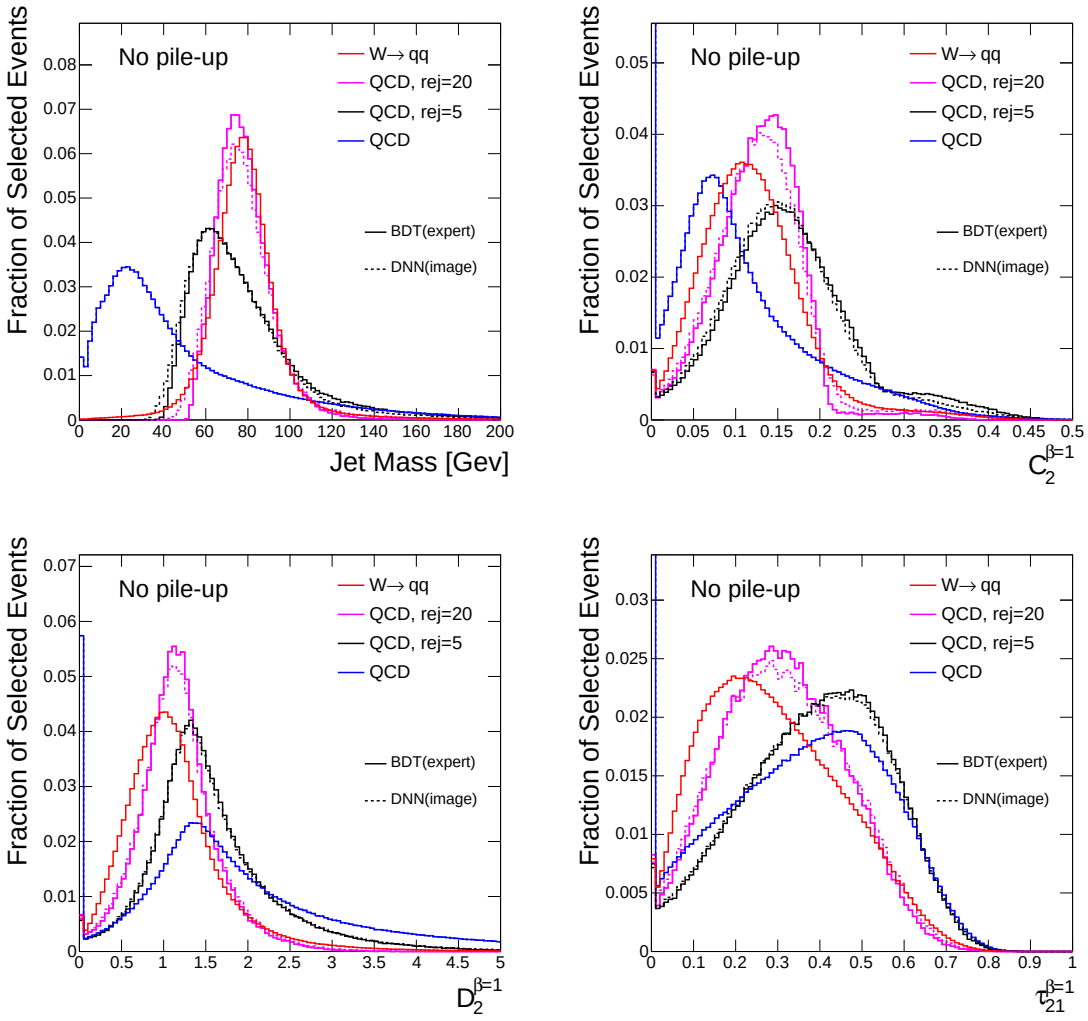

Figure 6.5: Distributions in simulated samples without pileup of high-level jet substructure variables for pure signal ($W \rightarrow qq$) and pure background (QCD) events. To explore the decision surface of the ML algorithms, also shown are background events with various levels of rejection for deep networks trained on the images and boosted decision trees trained on the expert features. Both algorithms preferentially select jets with values near the peak signal values. Note, however, that while the BDT has been supplied with these features as an input, the DNN has learned this on its own.

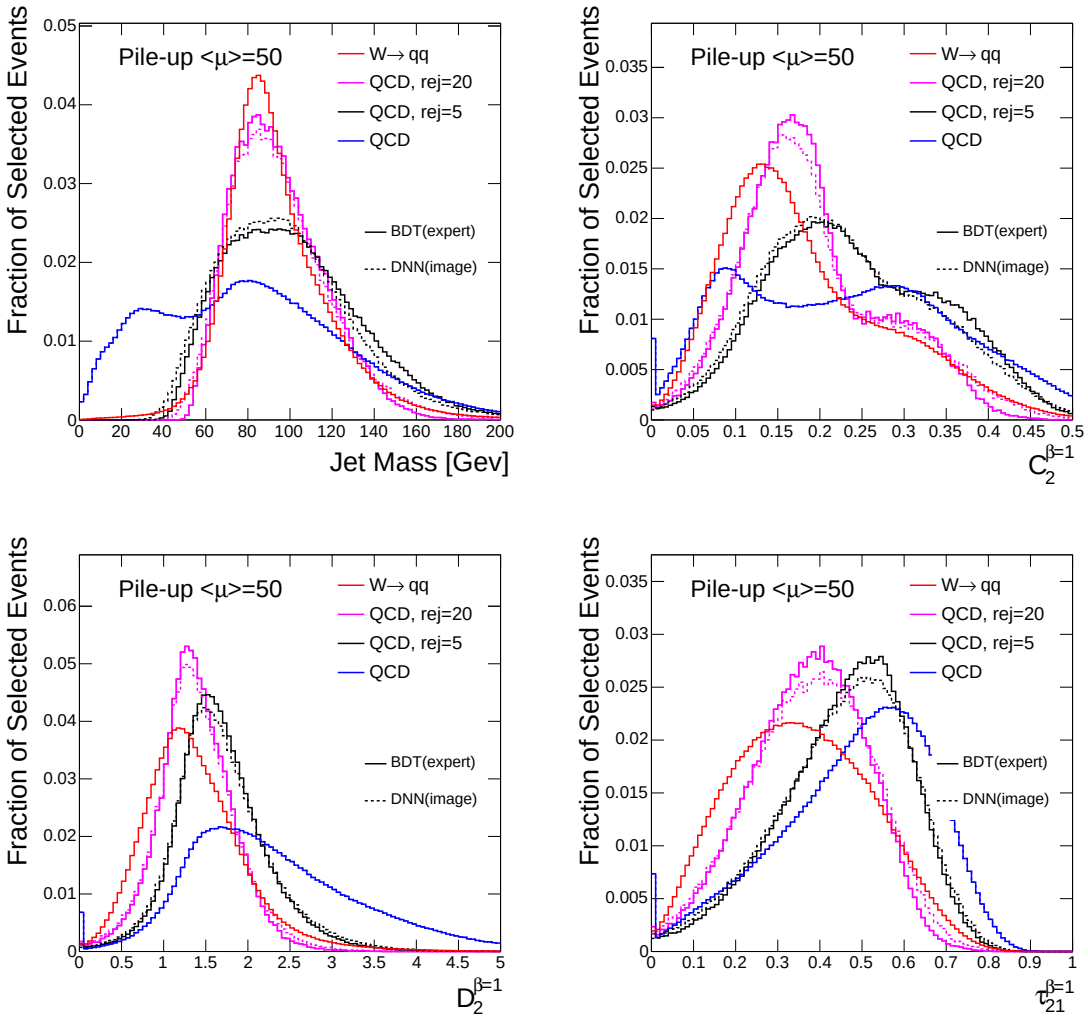

Figure 6.6: Distributions in simulated samples with pileup of high-level jet substructure variables for pure signal ($W \rightarrow qq$) and pure background (QCD) events. To explore the decision surface of the ML algorithms, also shown are background events with various levels of rejection for deep networks trained on the images and boosted decision trees trained on the expert features. Both algorithms preferentially select jets with values near the peak signal values. Note, however, that while the BDT has been supplied with these features as an input, the DNN has learned this on its own.

is based on a somewhat idealized description of the task (without detector or pileup effects), they cannot capture the totality of the information contained in the jet image. We report the first studies of the application of deep learning tools to the jet substructure problem to include simulation of detector and pileup effects.

Our experiments support two conclusions. First, that machine learning methods, particularly *deep* learning, can *automatically* extract the knowledge necessary for classification, in principle eliminating the exclusive reliance on expert features. The slight improvement in classification power offered by the deep network compared to the combination of expert features is likely due to the fact that the network has succeeded in discovering small optimizations of the expert features in order to account for the detector and pileup effects present in the simulated samples. This marks another demonstration of the power of deep networks to identify important features in high-dimensional problems. In practice, while deep network classification can boost jet tagging performance, expert features offer powerful insight [196] into the validity of the simulation models used to train these networks. We do not claim that these results make expert features obsolete. However, it suggests that deep networks can provide similar performance on a variety of related problems where the theoretical tools are not as mature. For example, current tools do not always include information from tracking detectors, nor do they offer performance parameterized [216, 217] in the mass of the decaying heavy state.

Second, we conclude that the current set of expert features when used in combination (via BDT or other shallow multi-variate approach) appear to capture nearly all of the relevant information in the high-dimensional low-level features describe by the jet image. The power of the networks described here is limited by the accuracy of these models, and expert features may be more robust to variation among the several existing simulation models [218]. In experimental applications, this reliance on simulation can be mitigated by using training samples from real collision data, where the labels are derived using orthogonal information.

Data in high energy physics can often be formulated as images. Thus, these results reported on the representative classification task of single q or g jets versus massive jets from $W \to qq'$ are very likely to apply to a broader set of similar tasks, such as classifying jets with three constituents, as in the case of top quark decay $t \to Wb \to qq'b$, or massive jets from other particles such as Higgs boson decays to bottom quark pairs. Note that in more realistic datasets, calorimeter information often contains depth information as well, such that the images are three-dimensional instead of two; however, this does not represent a difficult extrapolation for the machine learning algorithms. While the fundamental classification problems are very similar from a machine learning standpoint, the literature of expert features is somewhat less mature, further underlining the potential utility of the reported deep learning methods in these areas.

Future directions of research include studies of the robustness of such networks to systematic uncertainties in the input features and to change in the hadronization and showering model used in the simulated events.

Datasets used in this chapter containing millions of simulated collisions can be found in the UCI Machine Learning Repository [219].

Chapter 7

Muon Images

7.1 Introduction

Searches for resonances in the two-body invariant mass spectrum are a central element of the physics programs at every particle collider, including the Large Hadron Collider (LHC). These searches are motivated by the many extensions of the Standard Model which imply the existence of a heavy Z' boson, many of which decay leptonically, leading to di-electron or di-muon signatures.

One of the major backgrounds for di-muon searches come from muons produced in weak decays of heavy flavour quarks. That these muons are produced within a large decay chain of a jet means that these muons are surrounded by hadrons and are said to be "non-isolated". This contrasts from the "isolated" muons coming directly from a heavy Z' boson decay. The current state of the art technique used by these searches is a fairly simple single-variable cut on Isolation [229]:

$$Iso = \sum p_T^{\text{calo}} / p_T^{\text{muon}} \tag{7.1}$$

While this approach has benefits of simplicity and is a strong discriminant for high momentum muons, its performance weakens for low momentum muons below the typical range of a Standard Model Z boson resonance; see Fig 8 of Ref. [229]. This region of low pT di-muon resonances is also particularly important theoretically where a kinematically mixed Z' may have escaped detection at previous experiments [235].

Recent advances in machine learning techniques have shown significant results in image classification, applications in physics, and in jet physics, specially when using jet images [230, 231]. Since the background for isolated muons are jets, there are possible gains from applying the same ideas in this new context.

In this chapter, we use deep neural networks directly on muon images and compare it with state of the art techniques to see if there is more information available in the image, which can boost classification, and seek to interpret any new information in a physics context.

7.2 Approach

The metric we will use to compare performance is the Area Under the Curve (AUC) calculated using the signal (isolated muons) efficiency versus background (non-isolated muons) efficiency. Higher AUC indicated higher performance.

We will compare the performance of convolutional neural networks trained using "low level" information of raw calorimeter deposits (represented as pixelated "images") with the standard isolation. In addition, we expand on the typical one-variable approach to isolation by calculating several different isolation variables of different cone sizes and training a densely connected neural network using these "high level" variables. Isolation cones are always spaced uniformly from R=0 to the max R=0.4 (i.e. 4 isolation cones corresponds to R=(0.1,0.2,0.3,0.4)).

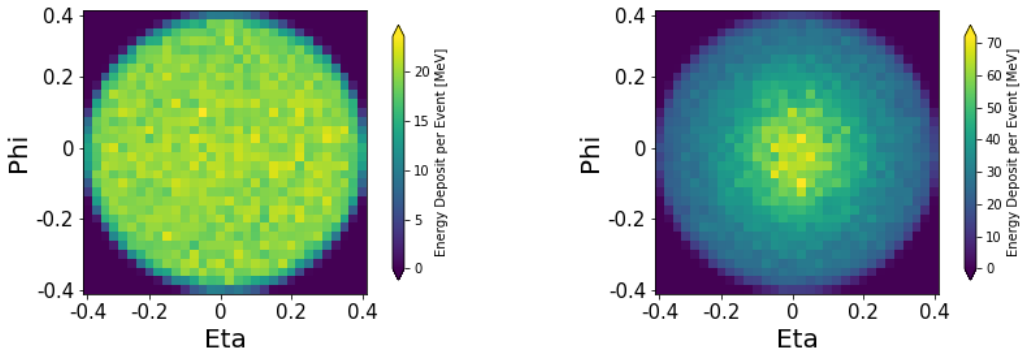

Figure 7.1: Average calorimeter images in the vicinity of reconstructed muons within a cone of $R = 0.4$. The color of each cell represents the sum of the E_T of the calorimeter deposits within the cell. Left are images from muons inside heavy boson decays, right are images from muons within b-quark jets.

In practice, the use of the high-dimensional muon image data to build a classifier is difficult due to validation of the approach in data and the determination of systematic uncertainties. Therefore, in this study, we will only use the image classifier to use as a benchmark which represents the best theoretically possible classifier. The goal will be to match or nearly match the performance of the calorimeter image networks using only a dense network trained on high-level observables. These high-level variables will be more interpretable and be more easily applied to ATLAS data from the LHC.

7.3 Data Generation

Samples of both signal isolated muons and background non-isolated muons are produced using common open source particle physics simulation tools.

Signal was generated using a sample of $pp \to Z' \to \mu\mu$ with a Z' mass of 20 GeV. Background was generated from $pp \to bb$. Both samples are generated at a center of mass energy $\sqrt{s} = 13\ TeV$ and only muons between $pT \in [10, 15]\ GeV$ are considered. Sample weights are applied while training the neural networks to account for the different shapes of the pT

spectrums. 100,000 signal and background events are generated. 70% of events are used for training the neural networks and the rest are reserved for testing.

Collisions and immediate decays are simulated with MADGRAPH5 [201], showering and hadronization with PYTHIA [194], and response of the detectors are simulated with DELPHES [202]. The muon images are characterized by the energies deposited at different points on the approximately cylindrical calorimeter surface.

The classification of these objects is sensitive to the presence of additional proton interactions, referred to as pile-up events. We overlay such interactions within the simulation with an average number of interactions per event of $< \mu >= 50$, as a future estimate of ATLAS data.

Only events where a muon is identified as a track in the muon spectrometer are used. Delphes default cuts on muon isolation are removed. In addition, we preprocess the calorimeter deposit images by centering the image on the coordinates of the identified muon and only include calorimeter deposits within a $\eta - \phi$ radius of $R < 0.4$ in order to only analyze the activity near the muon. Heat maps of the calorimeter energy deposits in $\eta - \phi$ space for both signal isolated muons and background non-isolated muons are shown in figure 7.1. The signal calorimeter deposits are uniform and can be attributed to pileup whereas the background deposits are radially symmetric with a dense core from the jet.

7.4 Neural Network Architecture

7.4.1 Low level images

The pixelated images were preprocessed to have zero mean and unit standard deviation. The muon image network structure begins with two convolutional layers with 32 rectified linear

units [236], followed by a 2x2 pooling layer, 2 more two convolutional layers with 64 rectified linear units, followed by another 2x2 pooling layer. Dropout [238] of 0.25 was used next for regularization. Afterwards 1 fully connected layer with 256 rectified linear units and a final layer with a sigmoid activation function to classify signal vs background. All weights were initialized using orthogonal weights [237]. Dropout [238] of 0.5 was used after every fully connected layer for regularization.

The models for isolation cones and EFP graphs had 3 fully connected layers with 200 rectified linear units and a final layer with sigmoid activation to make the classification. All weights were initialized using orthogonal weights.

All models were trained using stochastic gradient descent with binary cross-entropy loss for up to 20 epochs in Keras [239] using Tensorflow [240] back end.

7.4.2 High level variables

The high level variables are fed into a densely connected neural network from Keras with Tensorflow backend. In this architecture, three hidden layers are used with 200 units per layer and each using the rectifier activation function. The final layer uses the sigmoid activation function. In addition, the high level variables are preprocessed by subtracting the mean and dividing by the variance. The mean and variance are measured using the training dataset only. This method is commonly referred to as "standard scaling".

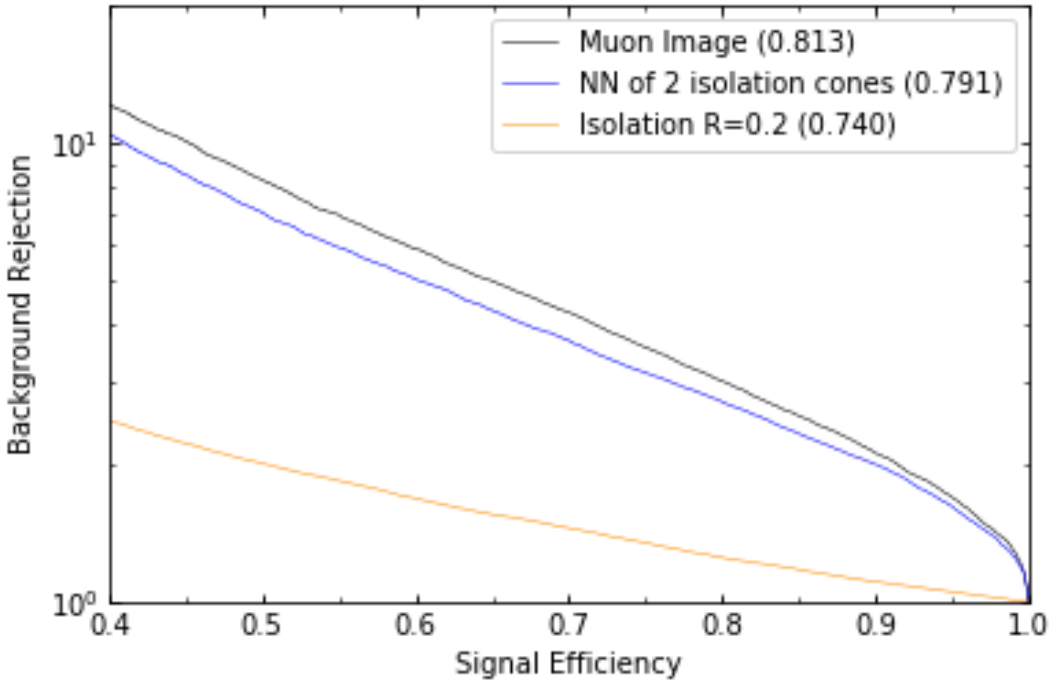

Figure 7.2: Signal efficiency versus background rejection (inverse of efficiency) for deep networks trained on muon images, shallow networks trained on a set of isolation cones and the most widely-used approach: a single isolation cone.

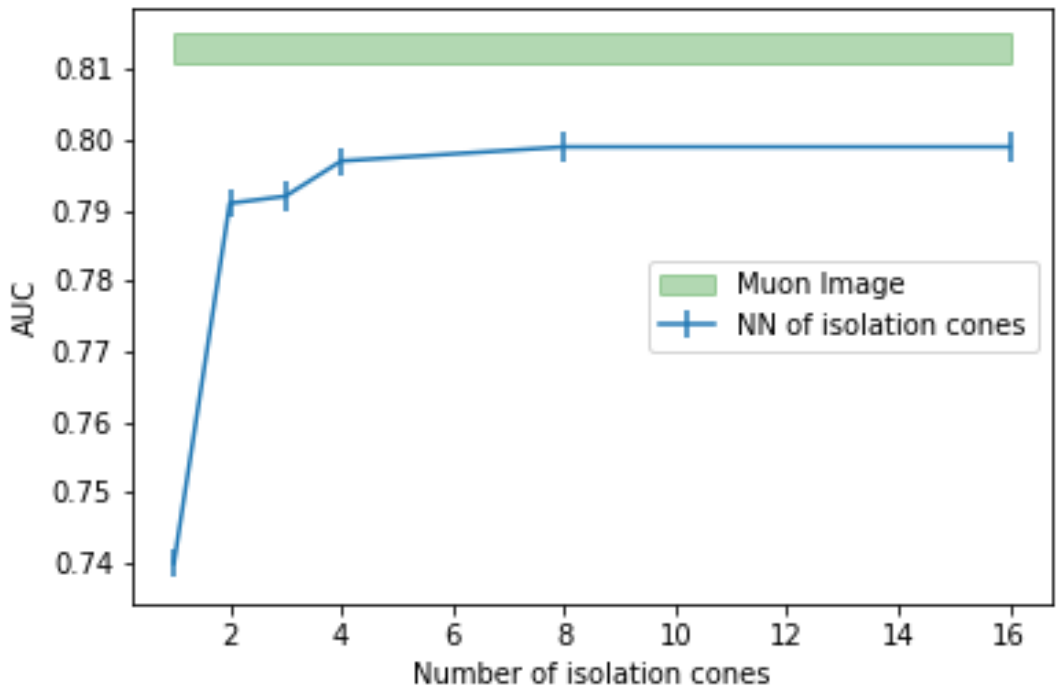

Figure 7.3: Comparison of classification performance using the metric AUC (Area Under the Curve of signal efficiency versus background efficiency, see Fig 7.2) between the deep networks trained on muon images and shallow networks with increasing numbers of isolation cones.

Table 7.1: Comparison of classification performance using the AUC (Area Under the Curve of signal efficiency versus background efficiency, see Fig 7.2) for various approaches. Statistical uncertainty in each case is ±0.002.

Network input	Network Structure	AUC
Muon Image	CNN	0.813
Eight Iso cones	Shallow NN	0.799
ISO with R=0.2	N/A	0.740

7.5 Results

7.5.1 Low Level compared to Isolation

The convolutional neural network trained with low-level muon images showed better performance than dense networks using the high-level isolation. The CNN measured an AUC of 0.813 with an uncertainty of 0.002 as measured by training 20 separate networks with random choices of training/testing sets. The uncertainty due to the initial conditions of the network was found to be negligible. A summary of the performances is given in Table 7.1 and Fig. 7.2.

Figure 7.3 compares the AUC of the CNN image with the neural networks trained using different densities of isolation cones. We observe that using just four isolation cones in a neural network significantly improves on the ATLAS standard of using just a single isolation cone of radius R=0.2. However, the performance gains from using increasingly many isolation cones quickly saturates. The difference between the CNN and the NN built from the isolation cones is statistically significant and we conclude that not all of the information contained in the images can be captured with isolation.

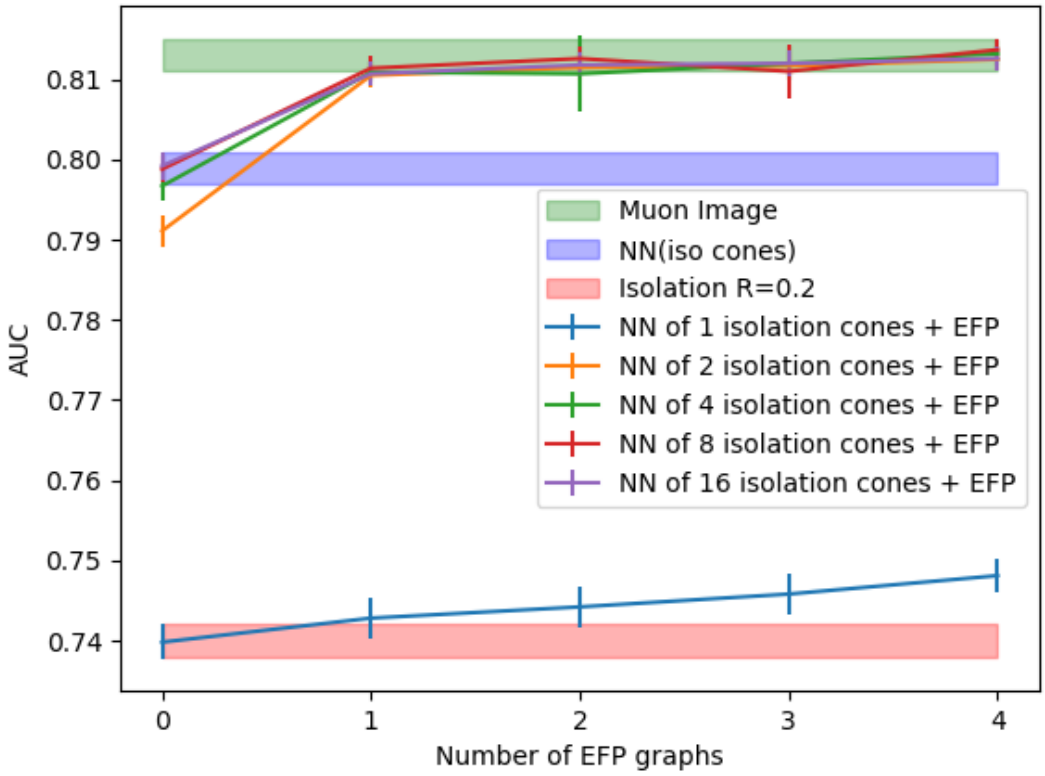

Figure 7.4: Comparison of classification performance using the metric AUC (Area Under the Curve of signal efficiency versus background efficiency, see Fig 7.2) between the deep networks trained on muon images and shallow networks with increasing numbers of EFP graphs. Kevin add N=1,2,4,8 iso + EFP

7.6 Results

7.6.1 Low Level compared to Isolation+EFP variables

In order to capture as much information as possible in as few observables as possible we expand our definition of the high level variables to include Energy Flow Polynomials (EFPs) [241]. Given that the background for this study is jets, EFPs are a natural place to search for extra information as they form a complete linear basis for jet substructure.

Analogous to our isolation study, we iteratively add EFPs to our high level densely connected

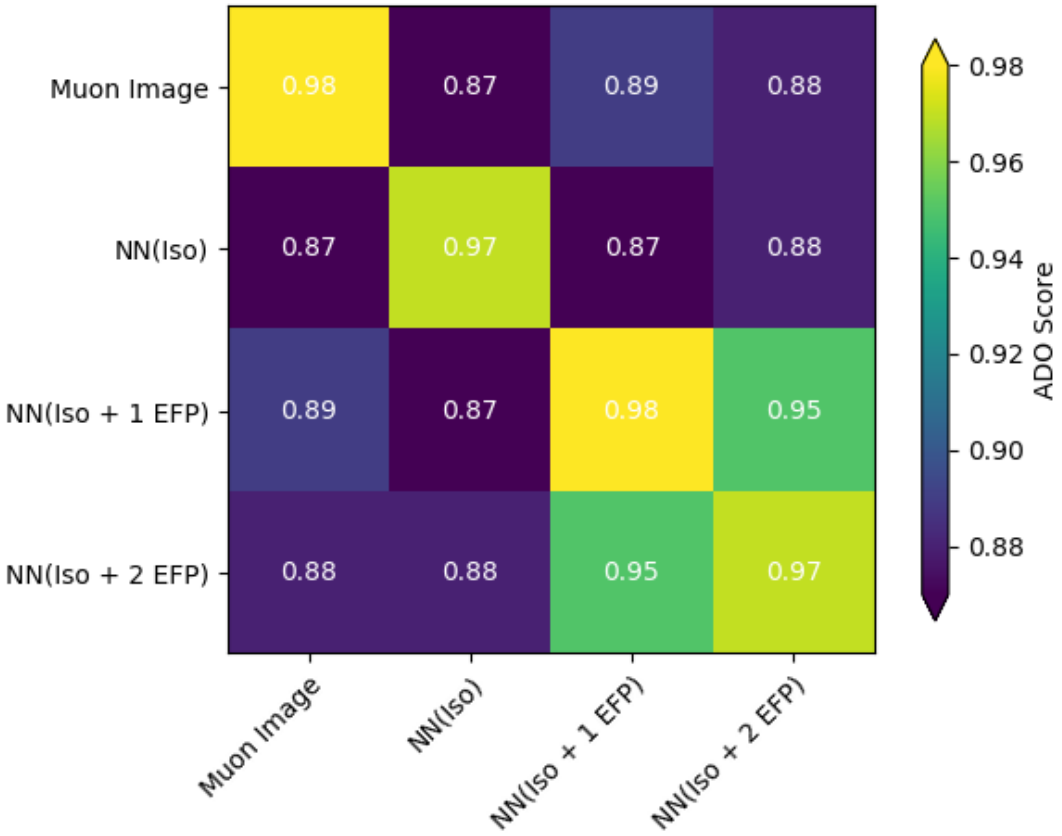

Figure 7.5: Discriminant ordering between different networks. A score of 1.0 indicates perfect similarity. The diagonal is measured as the DO between two networks trained with identical inputs but different initial conditions.

neural network. The order in which the EFP variables were added to the network was chosen in order to maximize the variance in the training dataset. Parameters for the EFPs, κ and β, were studied for both IR safe values ($\kappa = 1$,$\beta = 1$) and IR un-safe values ($\kappa = -1$,$\beta = 1$). Other choices of the parameters were studied but did not change the conclusions. The four most important EFPs were found to be D5q, D4f, D5p, and D4e and were all $\kappa = 1$ $\beta = 1$.

Figure 7.4 shows the effect of adding the EFPs to the high level network. Using just two EFPs we are able to match the performance of the CNN using muon image inputs. Like the isolation cones, the AUC quickly saturates.

To assess whether the muon image and the isolation+EFP networks are making the same classification decisions, we use the Average Decision Ordering metric [242], which measures how often two classifiers have the same relative signal-background ordering for pairs of input vectors. Figure 7.5 shows the discriminant ordering scores for the different high level and low level networks. This study suggests that while the AUC is matched by the high level network containing both isolation and EFPs, the high level network is still making dis-similar decisions from the low level network. Nevertheless, the high similarity between the 3 EFP network and 4 EFP network further supports that the information in the EFPs is saturated.

7.7 Conclusion

We have applied deep networks to images of low-level calorimeter deposits in order to estimate the amount of classification power available.

The performance of a convolutional neural network trained on muon calorimeter images is significantly greater than the benchmark approach, a single isolation cone at radius R=0.2. Additionally, the combination of just two isolation cones at different radii recovers the majority of that power, and the addition of an EFP observable closes the gap, see Fig. 7.6.

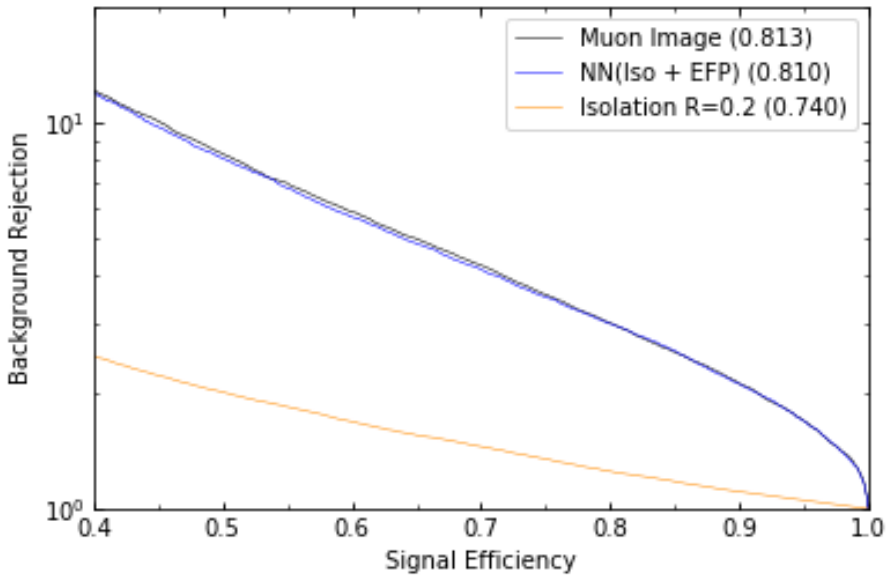

Figure 7.6: ROC curve comparing LL CNN with ATLAS state of the art isolation and our best HL network build from a combination of isolation and EFP

We hypothesize that added complexity with the angular information in the EFP observables contributes to the added information not captured in the isolation variables. Studies are ongoing to appear in a future publication.

These studies were performed in the low-p_{T} regime, where the background is more important. Similar results were obtained at higher muon p_{T}, though the gap between the single isolation cone and the muon image results was narrower.

Bibliography

[1] Symmetry Magazine, https://www.symmetrymagazine.org/standard-model/ (2019).

[2] E. Corbelli, and P. Salucci, Monthly Notices of the Royal Astronomical Society **311**, 441-447 (2000), astro-ph/9909252.

[3] Learner.org, https://www.learner.org/courses/physics/visual/visual.html?shortname=andromeda (2019).

[4] D. Clowe, et al., Astrophysical Journal Letters **648**, L109-L113 (2006), astro-ph/0608407.

[5] P.A.R. Ade,et al., Astron. Astrophys **594**, A13 (2016), arXiv:1502.01589.

[6] J.G. de Swart, et al., Nature Astronomy **1**, 59 (2017), arXiv:1703.00013.

[7] A. Kashlinsky, Astrophysical Journal **823**, (2016), arXiv:1605.04023.

[8] D. Hooper, et al. Physical Review D **70**, (2004), hep-ph/0402220.

[9] M. Drewes, International Journal of Modern Physics E **22**, (2013), arXiv:1303.6912.

[10] MiniBooNE Collaboration, Physical Review Letters **121**, (2018), arXiv:1805.12028.

[11] L. Evans, et al. JINST **3**, (2008),http://cds.cern.ch/record/1129806.

[12] ATLAS Collaboration, JINST **3**, (2008),http://cds.cern.ch/record/1129811.

[13] Collider, http://collider.physics.ox.ac.uk/detecting.html (2019).

[14] ATLAS Collaboration, Eur. Phys. J. C **76**, (2016),arXiv:1603.05598.

[15] ATLAS Collaboration, (2019),arXiv:1902.04655.

[16] ATLAS Collaboration, (2015),https://cds.cern.ch/record/2044564?ln=en.

[17] ATLAS Collaboration, Eur. Phys. J. C **77**, (2017),arXiv:1609.09324.

[18] Valerio Rossetti, *https* : *//indico.cern.ch/event*/278032/*contributions*/1623615/*attachments*/507531 (2014).

[19] P. Moreira, et al. in proceedings of Topical workshop on electronics for particle physics , (2007).

[20] J. Anderson, et al. in proceedings of Topical workshop on electronics for particle physics, (2016).

[21] J. Anderson, et al. in proceedings of 21st International Conference on Computing in High Energy and Nuclear Physics, (2015).

[22] G. Bertone, D. Hooper, and J. Silk, Phys.Rept. **405**, 279 (2005), hep-ph/0404175.

[23] M. Beltran, D. Hooper, E. W. Kolb, Z. A. Krusberg, and T. M. Tait, JHEP **1009**, 037 (2010), 1002.4137.

[24] P. J. Fox, R. Harnik, J. Kopp, and Y. Tsai, Phys.Rev. **D85**, 056011 (2012), 1109.4398.

[25] J. Goodman et al., Phys. Rev. **D82**, 116010 (2010), 1008.1783.

[26] A. Rajaraman, W. Shepherd, T. M. Tait, and A. M. Wijangco, Phys.Rev. **D84**, 095013 (2011), 1108.1196.

[27] G. Aad et al. (ATLAS) (2015), 1502.01518.

[28] V. Khachatryan et al. (CMS) (2014), 1408.3583.

[29] Y. Bai and T. M. Tait (2012), 1208.4361.

[30] G. Aad et al. (ATLAS Collaboration), Phys.Rev.Lett. **112**, 041802 (2014), 1309.4017.

[31] G. Aad et al. (ATLAS Collaboration) (2014), 1407.7494.

[32] V. Khachatryan et al. (CMS) (2014), 1408.2745.

[33] L. M. Carpenter, A. Nelson, C. Shimmin, T. M. Tait, and D. Whiteson, Phys.Rev. **D87**, 074005 (2013), 1212.3352.

[34] G. Aad et al. (ATLAS Collaboration), Phys.Rev. **D90**, 012004 (2014), 1404.0051.

[35] L. Carpenter, A. DiFranzo, M. Mulhearn, C. Shimmin, S. Tulin, et al., Phys.Rev. **D89**, 075017 (2014), 1312.2592.

[36] A. Berlin, T. Lin, and L.-T. Wang, JHEP **1406**, 078 (2014), 1402.7074.

[37] V. Khachatryan et al. (CMS) (2014), 1410.8812.

[38] G. Aad et al. (ATLAS), Phys.Rev. **D91**, 012008 (2015), 1411.1559.

[39] T. Lin, E. W. Kolb, and L.-T. Wang, Phys.Rev. **D88**, 063510 (2013), 1303.6638.

[40] U. Haisch and E. Re (2015), 1503.00691.

[41] C. Collaboration (CMS) (2014).

[42] G. Aad et al. (ATLAS Collaboration) (2014), 1410.4031.

[43] J. Abdallah, A. Ashkenazi, A. Boveia, G. Busoni, A. De Simone, et al. (2014), 1409.2893.

[44] S. Malik, C. McCabe, H. Araujo, O. Buchmueller, A. De Roeck, et al. (2014), 1409.4075.

[45] P. Langacker, Rev.Mod.Phys. **81**, 1199 (2009), 0801.1345.

[46] F. J. Petriello, S. Quackenbush, and K. M. Zurek, Phys.Rev. **D77**, 115020 (2008), 0803.4005.

[47] Y. Gershtein, F. Petriello, S. Quackenbush, and K. M. Zurek, Phys.Rev. **D78**, 095002 (2008), 0809.2849.

[48] H. An, X. Ji, and L.-T. Wang, JHEP **1207**, 182 (2012), 1202.2894.

[49] H. An, R. Huo, and L.-T. Wang, Phys.Dark Univ. **2**, 50 (2013), 1212.2221.

[50] M. T. Frandsen, F. Kahlhoefer, A. Preston, S. Sarkar, and K. Schmidt-Hoberg, JHEP **1207**, 123 (2012), 1204.3839.

[51] G. Arcadi, Y. Mambrini, M. H. G. Tytgat, and B. Zaldivar, JHEP **1403**, 134 (2014), 1401.0221.

[52] A. Alves, S. Profumo, and F. S. Queiroz, JHEP **1404**, 063 (2014), 1312.5281.

[53] G. Busoni, A. De Simone, J. Gramling, E. Morgante, and A. Riotto, JCAP **1406**, 060 (2014), 1402.1275.

[54] A. Alves, A. Berlin, S. Profumo, and F. S. Queiroz (2015), 1501.03490.

[55] M. Abdullah, E. Albin, A. DiFranzo, M. Frate, C. Pitcher, et al., Phys.Rev. **D89**, 095002 (2014), 1401.1462.

[56] Y. Bai, J. Bourbeau, and T. Lin (to appear).

[57] A. Gupta, R. Primulando, and P. Saraswat (to appear).

[58] T. R. Dulaney, P. Fileviez Perez, and M. B. Wise, Phys.Rev. **D83**, 023520 (2011), 1005.0617.

[59] M. L. Graesser, I. M. Shoemaker, and L. Vecchi (2011), 1107.2666.

[60] P. J. Fox, J. Liu, D. Tucker-Smith, and N. Weiner, Phys.Rev. **D84**, 115006 (2011), 1104.4127.

[61] B. Holdom, Phys.Lett. **B166**, 196 (1986).

[62] E. Izaguirre, B. Shuve, and I. Yavin, Phys.Rev.Lett. **114**, 041802 (2015), 1407.7037.

[63] B. A. Dobrescu and F. Yu, Phys.Rev. **D88**, 035021 (2013), 1306.2629.

[64] J. Alitti et al. (UA2 Collaboration), Nucl.Phys. **B400**, 3 (1993).

[65] J. Alitti et al. (UA2 Collaboration), Z.Phys. **C49**, 17 (1991).

[66] F. Abe et al. (CDF Collaboration), Phys.Rev. **D41**, 1722 (1990).

[67] G. Z. Krnjaic, Phys.Rev. **D85**, 014030 (2012), 1109.0648.

[68] J. Alcaraz et al. (ALEPH Collaboration, DELPHI Collaboration, L3 Collaboration, OPAL Collaboration, LEP Electroweak Working Group) (2006), hep-ex/0612034.

[69] W. Altmannshofer, S. Gori, M. Pospelov, and I. Yavin, Phys.Rev. **D89**, 095033 (2014), 1403.1269.

[70] T. Aaltonen et al. (CDF Collaboration), Phys.Rev.Lett. **102**, 091805 (2009), 0811.0053.

[71] G. Aad et al. (ATLAS Collaboration), Phys.Rev. **D90**, 052005 (2014), 1405.4123.

[72] V. Khachatryan et al. (CMS Collaboration) (2014), 1412.6302.

[73] The ATLAS Collaboration (2013), URL https://cds.cern.ch/record/1523695.

[74] V. Khachatryan et al. (CMS) (2014), 1410.6679.

[75] I. Hoenig, G. Samach, and D. Tucker-Smith (2014), 1408.1075.

[76] S. Chatrchyan et al. (CMS Collaboration), JHEP **1312**, 030 (2013), 1310.7291.

[77] C. D. Carone and H. Murayama, Phys.Rev.Lett. **74**, 3122 (1995), hep-ph/9411256.

[78] C. D. Carone and H. Murayama, Phys.Rev. **D52**, 484 (1995), hep-ph/9501220.

[79] K. Olive et al. (Particle Data Group), Chin.Phys. **C38**, 090001 (2014).

[80] A. Hook, E. Izaguirre, and J. G. Wacker, Adv.High Energy Phys. **2011**, 859762 (2011), 1006.0973.

[81] A. De Simone, G. F. Giudice, and A. Strumia, JHEP **1406**, 081 (2014), 1402.6287.

[82] M. J. Strassler and K. M. Zurek, Phys.Lett. **B651**, 374 (2007), hep-ph/0604261.

[83] T. Han, Z. Si, K. M. Zurek, and M. J. Strassler, JHEP **0807**, 008 (2008), 0712.2041.

[84] Y. Bai and Z. Han, Phys.Rev.Lett. **103**, 051801 (2009), 0902.0006.

[85] Y. F. Chan, M. Low, D. E. Morrissey, and A. P. Spray, JHEP **1205**, 155 (2012), 1112.2705.

[108] J. Alwall, R. Frederix, S. Frixione, V. Hirschi, F. Maltoni, et al., JHEP **1407**, 079 (2014), 1405.0301.

[129] T. Sjostrand, S. Mrenna, and P. Z. Skands, JHEP **0605**, 026 (2006), hep-ph/0603175.

[88] J. de Favereau et al. (DELPHES 3), JHEP **1402**, 057 (2014), 1307.6346.

[166] G. Cowan, K. Cranmer, E. Gross, and O. Vitells, Eur.Phys.J. **C71**, 1554 (2011), 1007.1727.

[167] A. L. Read, J.Phys. **G28**, 2693 (2002).

[91] T. Junk, Nucl.Instrum.Meth. **A434**, 435 (1999), hep-ex/9902006.

[92] G. Aad et al. (ATLAS Collaboration), JHEP **1409**, 176 (2014), 1405.7875.

[95] G. Aad et al. (ATLAS Collaboration), JHEP **1405**, 071 (2014), 1403.5294.

[94] Autran M., et al. Searches for dark matter in events with a resonance and missing transverse energy. Phys. Rev. D, 92:035007, 2015.

[95] G. Aad et al. (ATLAS Collaboration), Phys. Lett. B **763**, 253 (2016), 1608.02372.

[96] Buchmueller O., et al. Characterising dark matter searches at colliders and direct detection experiments: Vector mediators. JHEP, 01:037, 2015.

[97] Abercrombie D., et al. Dark Matter Benchmark Models for Early LHC Run-2 Searches: Report of the ATLAS/CMS Dark Matter Forum. (2015), arXic: 1507.00966

[98] Antoniadis I., et al. Phenomenology of a leptonic goldstino and invisible Higgs boson decays. Nucl. Phys. B, 707:215, 2005.

[99] Arkani-Hamed N., et al. Neutrino masses from large extra dimensions. Phys. Rev. D, 65:024032, 2001.

[100] Datta A., et al. Linear collider signals of an invisible Higgs boson in theories of large extra dimensions. Phys. Rev. D, 70:075003, 2004.

[101] Kanemura S., et al. Can WIMP dark matter overcome the nightmare scenario?. Phys. Rev. D, 82:055026, 2010.

[102] Djouadi A., et al. Implications of LHC searches for Higgs-portal dark matter. Phys. Lett. B, 709:65, 2012.

[103] Agostinelli S., et al. GEANT4: A Simulation toolkit. NIMA, 506:250, 2003.

[104] ATLAS Collaboration The ATLAS Simulation Infrastructure. Eur. Phys. J. C, 70:823, 2010.

[105] Sjostrand T., et al. A Brief Introduction to PYTHIA 8.1. Comput. Phys. Commun., 178:852, 2008.

[106] ATLAS Collaboration Summary of ATLAS Pythia 8 tunes. ATL-PHYS-PUB-2012-003, 2012.

[107] Martin A.D., et al. Parton distributions for the LHC. Eur. Phys. J. C, 63:189, 2009.

[108] Alwall J., et al. The automated computation of tree-level and next-to-leading order differential cross sections, and their matching to parton shower simulations. JHEP, 07:079, 2014.

[109] ATLAS Collaboration ATLAS Pythia 8 tunes to 7 TeV data. ATL-PHYS-PUB-2014-021, 2014.

[110] Ball R.D., et al. Parton distributions for the LHC Run II. JHEP, 04:040, 2015.

[111] Albert A., et al. Recommendations of the LHC Dark Matter Working Group: Comparing LHC searches for heavy mediators of dark matter production in visible and invisible decay channels. 2017, arXiv: 1703.05703.

[112] ATLAS Collaboration Search for light resonances decaying to boosted quark pairs and produced in association with a photon or a jet in proton–proton collisions at $\sqrt{s} = 13$ TeV with the ATLAS detector. 2018, arXiv: 1801.08769

[113] CMS Collaboration Search for low mass vector resonances decaying into quark–antiquark pairs in proton–proton collisions at $\sqrt{s} = 13$ TeV . JHEP, 01:097, 2018.

[114] ATLAS Collaboration Search for new phenomena in final states with an energetic jet and large missing transverse momentum in pp collisions at $\sqrt{s} = 13$ TeV using the ATLAS detector. Phys. Rev. D, 94:032005, 2016.

[115] CMS Collaboration Search for dijet resonances in proton–proton collisions at $\sqrt{s} = 13$ TeV and constraints on dark matter and other models. Phys. Lett. B, 769:520, 2017.

[116] Nason P., et al. A New method for combining NLO QCD with shower Monte Carlo algorithms. JHEP, 11:040, 2004.

[117] Frixione S., et al. Matching NLO QCD computations with Parton Shower simulations: the POWHEG method. JHEP, 11:070, 2007.

[118] Alioli S., et al. A general framework for implementing NLO calculations in shower Monte Carlo programs: the POWHEG BOX. JHEP, 06:043, 2010.

[119] ATLAS Collaboration JHEP, 10:132, 2017, arXiv: 1708.02810.

[120] ATLAS Collaboration JHEP, 12:024, 2017, arXiv: 1708.03299.

[121] Gleisberg T., et al. Event generation with SHERPA 1.1. JHEP, 02:007, 2009.

[122] Gleisberg T., et al. Comix, a new matrix element generator. JHEP, 12:039, 2008.

[123] Cascioli F., et al. Scattering Amplitudes with Open Loops. Phys. Rev. Lett., 108:111601, 2012.

[124] Schumann S., et al. A Parton shower algorithm based on Catani-Seymour dipole factorisation. JHEP, 03:038, 2008.

[125] Hoeche S., et al. QCD matrix elements + parton showers: The NLO case. JHEP, 04:027, 2013.

[126] Melnikov K., et al. Phys. Rev. D, 74:114017, 2006, arXiv: hep-ph/0609070.

[127] Lai H.-L., et al. New parton distributions for collider physics Phys. Rev. D, 82:074024, 2010.

[128] Artoisenet P., et al. Automatic spin-entangled decays of heavy resonances in Monte Carlo simulations JHEP, 03:015, 2013.

[129] Stostrand T., et al. PYTHIA 6.4 Physics and Manual JHEP, 05:026, 2006.

[130] Pumplin J., et al. New generation of parton distributions with uncertainties from global QCD analysis JHEP, 07:012, 2002.

[131] Skands P.Z., et al. Tuning Monte Carlo Generators: The Perugia Tunes Phys. Rev. D, 82:074018, 2010.

[132] Lange D.J. The EvtGen particle decay simulation package, NIMA, 462:152, 2001.

[133] Czakon M., et al. Phys. Rev. Lett., 110:252004, 2013, arXiv: 1303.6254 .

[134] Stelzer T., et al. Single top quark production via W - gluon fusion at next-to-leading order Phys. Rev. D, 56:5919, 1997.

[135] Stelzer T., et al. Single top quark production at hadron colliders Phys. Rev. D, 58:094021, 1998.

[136] Smith M.C., et al. QCD and Yukawa corrections to single top quark production via $q\bar{q} \to t\bar{b}$ Phys. Rev. D, 54:6696, 1996.

[137] Kidonakis N., et al. Top Quark Production DESY-PROC-2013-03, arXiv: 1311.0283.

[138] ATLAS Collaboration Topological cell clustering in the ATLAS calorimeters and its performance in LHC Run 1. Eur. Phys. J. C, 77:490, 2017.

[139] Cacciari M., et al. The anti-kt jet clustering algorithm JHEP, 04:063, 2008.

[140] Cacciari M., et al. FastJet User Manual Eur. Phys. J. C, 72:1896, 2012.

[141] ATLAS Collaboration Tagging and suppression of pileup jets with the ATLAS detector. ATLAS-CONF-2014-018, 2014.

[142] ATLAS Collaboration Jet energy scale measurements and their systematic uncertainties in proton–proton collisions at $\sqrt{s} = 13$ TeV with the ATLAS detector. Phys. Rev. D, 96:072002, 2017.

[143] ATLAS Collaboration Data-driven determination of the energy scale and resolution of jets reconstructed in the ATLAS calorimeters using dijet and multijet events at $\sqrt{s} =$ 8 TeV. ATLAS-CONF-2015-017, 2015.

[144] ATLAS Collaboration Performance of b-jet identification in the ATLAS experiment. JINST, 11:P04008, 2016.

[145] ATLAS Collaboration Optimisation of the ATLAS b-tagging performance for the 2016 LHC Run. ATL-PHYS-PUB-2016-012, 2016.

[146] ATLAS Collaboration Commissioning of the ATLAS b-tagging algorithms using $t\bar{t}$ events in early Run 2 data. ATL-PHYS-PUB-2015-039, 2015.

[147] ATLAS Collaboration Identification of Boosted, Hadronically Decaying W Bosons and Comparisons with ATLAS Data Taken at $\sqrt{s} = 8$ TeV. Eur. Phys. J. C, 76:154, 2016.

[148] ATLAS Collaboration Identification of Boosted, Hadronically-Decaying W and Z Bosons in $\sqrt{s} = 13$ TeV Monte Carlo Simulations for ATLAS,. ATL-PHYS-PUB-2015-033, 2015.

[149] Krohn D., et al. Jet Trimming JHEP, 02:084, 2010.

[150] ATLAS Collaboration Jet mass reconstruction with the ATLAS Detector in early Run 2 data. ATLAS-CONF-2016-035, 2016.

[151] Larkoski A.J, et al. Power Counting to Better Jet Observables JHEP, 12:009, 2014.

[152] Larkoski A.J, et al. Energy Correlation Functions for Jet Substructure, JHEP, 16:108, 2013.

[153] ATLAS Collaboration Performance of jet substructure techniques for large-R jets in proton–proton collisions at $\sqrt{s} = 7$ TeV using the ATLAS detector. JHEP, 09:076, 2013.

[154] ATLAS Collaboration Performance of jet substructure techniques in early $\sqrt{s} = 13$ TeV pp collisions with the ATLAS detector. ATLAS-CONF-2015-035, 2015.

[155] ATLAS Collaboration Flavor Tagging with Track-Jets in Boosted Topologies with the ATLAS Detector. ATL-PHYS-PUB-2014-013, 2014.

[156] ATLAS Collaboration Boosted Higgs $\rightarrow b\bar{b}$ Boson Identification with the ATLAS Detector at $\sqrt{s} = 13$ TeV. ATLAS-CONF-2016-039, 2016.

[157] Cacciari M., et al. The Catchment Area of Jets JHEP, 04:005, 2008.

[158] ATLAS Collaboration Electron efficiency measurements with the ATLAS detector using 2012 LHC proton–proton collision data. Eur. Phys. J. C, 77:195, 2017.

[159] ATLAS Collaboration Electron efficiency measurements with the ATLAS detector using the 2015 LHC proton–proton collision data. ATLAS-CONF-2016-024, 2016.

[160] ATLAS Collaboration Electron and photon energy calibration with the ATLAS detector using LHC Run 1 data. Eur. Phys. J. C, 74:3071, 2014.

[161] ATLAS Collaboration Electron and photon energy calibration with the ATLAS detector using data collected in 2015 at $\sqrt{s} = 13$ TeV. ATL-PHYS-PUB-2016-015, 2016.

[162] ATLAS Collaboration Muon reconstruction performance of the ATLAS detector in proton–proton collision data at $\sqrt{s} = 13$ TeV. Eur. Phys. J. C, 76:292, 2016.

[163] ATLAS Collaboration Performance of missing transverse momentum reconstruction with the ATLAS detector using proton-proton collisions at $\sqrt{s} = 13$ TeV. 2018, arXiv: 1802.08168.

[164] ATLAS Collaboration Performance of Top Quark and W Boson Tagging in Run 2 with ATLAS. ATLAS-CONF-2017-064, 2017.

[165] ATLAS Collaboration Luminosity determination in pp collisions at $\sqrt{s} = 8$ TeV using the ATLAS detector at the LHC. Eur. Phys. J. C, 76:653, 2016.

[166] Cowan G., et al. Asymptotic formulae for likelihood-based tests of new physics Eur. Phys. J. C, 71:1554, 2011.

[167] Read A.L., et al. Presentation of search results: The CL(s) technique J. Phys. G, 28:2693, 2002.

[168] ATLAS Collaboration Search for invisible decays of the Higgs boson produced in association with a hadronically decaying vector boson in pp collisions at $\sqrt{s} = 8$ TeV with the ATLAS detector. Eur. Phys. J. C, 75:337, 2015.

[169] WMAP Collaboration Nine-Year Wilkinson Microwave Anisotropy Probe (WMAP) Observations: Cosmological Parameter Results. Astrophys. J. Supp., 208:19, 2013.

[170] Planck Collaboration Planck 2015 results. I. Overview of products and scientific results. Astron. Astrophys., 594:A1, 2016.

[171] Backovic M., et al. Direct Detection of Dark Matter with MadDM v.2.0. Phys. Dark Univ., 9-10:37, 2015.

[172] Gross E., et al. Trial factors or the look elsewhere effect in high energy physics. Eur. Phys. J. C, 70:525, 2010.

[173] Jonathan M. Butterworth, Adam R. Davison, Mathieu Rubin, and Gavin P. Salam. Jet substructure as a new Higgs search channel at the LHC. *Phys.Rev.Lett.*, 100:242001, 2008.

[174] D. Adams, A. Arce, L. Asquith, M. Backovic, T. Barillari, et al. Towards an Understanding of the Correlations in Jet Substructure. 2015.

[175] A. Abdesselam et al. Boosted objects: A Probe of beyond the Standard Model physics. *Eur. Phys. J.*, C71:1661, 2011.

[176] A. Altheimer et al. Jet Substructure at the Tevatron and LHC: New results, new tools, new benchmarks. *J. Phys.*, G39:063001, 2012.

[177] A. Altheimer et al. Boosted objects and jet substructure at the LHC. Report of BOOST2012, held at IFIC Valencia, 23rd-27th of July 2012. *Eur. Phys. J.*, C74(3):2792, 2014.

[178] Tilman Plehn, Michael Spannowsky, Michihisa Takeuchi, and Dirk Zerwas. Stop Reconstruction with Tagged Tops. *JHEP*, 1010:078, 2010.

[179] David E. Kaplan, Keith Rehermann, Matthew D. Schwartz, and Brock Tweedie. Top Tagging: A Method for Identifying Boosted Hadronically Decaying Top Quarks. *Phys.Rev.Lett.*, 101:142001, 2008.

[180] Andrew J. Larkoski, Simone Marzani, Gregory Soyez, and Jesse Thaler. Soft Drop. *JHEP*, 1405:146, 2014.

[181] Jesse Thaler and Ken Van Tilburg. Identifying Boosted Objects with N-subjettiness. *JHEP*, 1103:015, 2011.

[182] Andrew J. Larkoski, Gavin P. Salam, and Jesse Thaler. Energy Correlation Functions for Jet Substructure. *JHEP*, 1306:108, 2013.

[183] J. Thaler D. Krohn and L.-T. Wang. Jet Trimming. *JHEP*, 1002:084, 2010.

[184] C. K. Vermilion S. D. Ellis and J. R. Walsh. Recombination Algorithms and Jet Substructure: Pruning as a Tool for Heavy Particle Searches. *Phys.Rev.*, D81:094023, 2010.

[185] S. Marzani M. Dasgupta, A. Fregoso and G. P. Salam. Towards an understanding of jet substructure. *JHEP*, 1309:029,, 2013.

[186] Mrinal Dasgupta, Alessandro Fregoso, Simone Marzani, and Alexander Powling. Jet substructure with analytical methods. *Eur. Phys. J.*, C73(11):2623, 2013.

[187] Mrinal Dasgupta, Alexander Powling, and Andrzej Siodmok. On jet substructure methods for signal jets. *JHEP*, 08:079, 2015.

[188] Pierre Baldi, Peter Sadowski, and Daniel Whiteson. Searching for exotic particles in high-energy physics with deep learning. *Nature Communications*, 5, July 2014.

[189] Pierre Baldi, Peter Sadowski, and Daniel Whiteson. Enhanced higgs boson to $\tau^+\tau^-$ search with deep learning. *Phys. Rev. Lett.*, 114:111801, Mar 2015.

[190] Peter Sadowski, Julian Collado, Daniel Whiteson, and Pierre Baldi. Deep Learning, Dark Knowledge, and Dark Matter. pages 81–87, 2014.

[191] Davison E. Soper and Michael Spannowsky. Finding physics signals with shower deconstruction. *Phys. Rev.*, D84:074002, 2011.

[192] Davison E. Soper and Michael Spannowsky. Finding top quarks with shower deconstruction. *Phys. Rev.*, D87:054012, 2013.

[193] Iain W. Stewart, Frank J. Tackmann, and Wouter J. Waalewijn. Dissecting Soft Radiation with Factorization. *Phys. Rev. Lett.*, 114(9):092001, 2015.

[194] T. Sjostrand et al. PYTHIA 6.4 physics and manual. *JHEP*, 05:026, 2006.

[195] M. Bahr et al. Herwig++ Physics and Manual. *Eur. Phys. J.*, C58:639–707, 2008.

[196] Andrew J. Larkoski, Ian Moult, and Duff Neill. Analytic Boosted Boson Discrimination. 2015.

[197] Josh Cogan, Michael Kagan, Emanuel Strauss, and Ariel Schwartzman. Jet-images: computer vision inspired techniques for jet tagging. *Journal of High Energy Physics*, 2015(2):1–16, February 2015.

[198] Leandro G. Almeida, Mihailo Backovic, Mathieu Cliche, Seung J. Lee, and Maxim Perelstein. Playing Tag with ANN: Boosted Top Identification with Pattern Recognition. *arXiv:1501.05968 [hep-ex, physics:hep-ph]*, January 2015. arXiv: 1501.05968.

[199] Performance of Boosted W Boson Identification with the ATLAS Detector. *Tech. Rep. ATL-PHYS-PUB-2014-004, CERN, Geneva*, Mar. 2014.

[200] Luke de Oliveira, Michael Kagan, Lester Mackey, Benjamin Nachman, and Ariel Schwartzman. Jet-Images – Deep Learning Edition. 2015.

[201] Johan Alwall et al. MadGraph 5 : Going Beyond. *JHEP*, 1106:128, 2011.

[202] S. Ovyn, X. Rouby, and V. Lemaitre. DELPHES, a framework for fast simulation of a generic collider experiment. 2009.

[203] Matteo Cacciari, Gavin P. Salam, and Gregory Soyez. The Anti-k(t) jet clustering algorithm. *JHEP*, 04:063, 2008.

[204] David Krohn, Jesse Thaler, and Lian-Tao Wang. Jet Trimming. *JHEP*, 02:084, 2010.

[205] Stephen D. Ellis and Davison E. Soper. Successive combination jet algorithm for hadron collisions. *Phys. Rev.*, D48:3160–3166, 1993.

[206] Matteo Cacciari, Gavin P. Salam, and Gregory Soyez. FastJet User Manual. *Eur.Phys.J.*, C72:1896, 2012.

[207] Jesse Thaler and Ken Van Tilburg. Maximizing Boosted Top Identification by Minimizing N-subjettiness. *JHEP*, 02:093, 2012.

[208] Andrew J. Larkoski, Ian Moult, and Duff Neill. Power Counting to Better Jet Observables. *JHEP*, 12:009, 2014.

[209] Jasper Snoek, Hugo Larochelle, and Ryan P Adams. Practical bayesian optimization of machine learning algorithms. In F. Pereira, C. J. C. Burges, L. Bottou, and K. Q. Weinberger, editors, *Advances in Neural Information Processing Systems 25*, pages 2951–2959. Curran Associates, Inc., 2012.

[210] Diederik Kingma and Jimmy Ba. Adam: A Method for Stochastic Optimization. *arXiv:1412.6980 [cs]*, December 2014. arXiv: 1412.6980.

[211] Kaiming He, Xiangyu Zhang, Shaoqing Ren, and Jian Sun. Delving Deep into Rectifiers: Surpassing Human-Level Performance on ImageNet Classification. *arXiv:1502.01852 [cs]*, February 2015. arXiv: 1502.01852.

[212] François Chollet. *Keras*. GitHub, 2015.

[213] James Bergstra, Olivier Breuleux, Frédéric Bastien, Pascal Lamblin, Razvan Pascanu, Guillaume Desjardins, Joseph Turian, David Warde-Farley, and Yoshua Bengio. Theano: a CPU and GPU math expression compiler. In *Proceedings of the Python for Scientific Computing Conference (SciPy)*, Austin, TX, June 2010. Oral Presentation.

[214] Frederic Bastien, Pascal Lamblin, Razvan Pascanu, James Bergstra, Ian Goodfellow, Arnaud Bergeron, Nicolas Bouchard, David Warde-Farley, and Yoshua Bengio. Theano: new features and speed improvements. *arXiv:1211.5590 [cs]*, November 2012.

[215] F. Pedregosa, G. Varoquaux, A. Gramfort, V. Michel, B. Thirion, O. Grisel, M. Blondel, P. Prettenhofer, R. Weiss, V. Dubourg, J. Vanderplas, A. Passos, D. Cournapeau, M. Brucher, M. Perrot, and E. Duchesnay. Scikit-learn: Machine learning in Python. *Journal of Machine Learning Research*, 12:2825–2830, 2011.

[216] Pierre Baldi, Kyle Cranmer, Taylor Faucett, Peter Sadowski, and Daniel Whiteson. Parameterized Machine Learning for High-Energy Physics. 2016.

[217] Kyle Cranmer. Approximating Likelihood Ratios with Calibrated Discriminative Classifiers. 2015.

[218] James Dolen, Philip Harris, Simone Marzani, Salvatore Rappoccio, and Nhan Tran. Thinking outside the ROCs: Designing Decorrelated Taggers (DDT) for jet substructure. 2016.

[219] Pierre Baldi, Kevin Bauer, Clara Eng, Peter Sadowski, and Daniel Whiteson. Data for jet substructure for high-energy physics, 2016. `http://http://www.igb.uci.edu/~pfbaldi/physics/`.

[229] G. Aad et al. (ATLAS), Eur. Phys. J. **C76**, 292 (2016), `1603.05598`.

[230] J. Cogan, M. Kagan, E. Strauss, and A. Schwartzman, JHEP **02**, 118 (2015), `1407.5675`.

[231] P. Baldi, K. Bauer, C. Eng, P. Sadowski, and D. Whiteson, Phys. Rev. **D93**, 094034 (2016), `1603.09349`.

[232] R. Aaij et al. (LHCb), Phys. Rev. Lett. **120**, 061801 (2018), 1710.02867.

[233] Z. Hall and J. Thaler, JHEP **09**, 164 (2018), 1805.11622.

[234] C. Brust, P. Maksimovic, A. Sady, P. Saraswat, M. T. Walters, and Y. Xin, JHEP **04**, 079 (2015), 1410.0362.

[235] Z. Hoenig et al. Phys. Rev. D **90**, 023 (2014), 1408.1075.

[241] P. T. Komiske, E. M. Metodiev, and J. Thaler, JHEP **04**, 013 (2018), 1712.07124.

[242] T. Faucett et al. (2019).

[229] G. Aad et al. (ATLAS), Eur. Phys. J. **C76**, 292 (2016), 1603.05598.

[230] J. Cogan, M. Kagan, E. Strauss, and A. Schwarztman, JHEP **02**, 118 (2015), 1407.5675.

[231] P. Baldi, K. Bauer, C. Eng, P. Sadowski, and D. Whiteson, Phys. Rev. **D93**, 094034 (2016), 1603.09349.

[232] R. Aaij et al. (LHCb), Phys. Rev. Lett. **120**, 061801 (2018), 1710.02867.

[233] Z. Hall and J. Thaler, JHEP **09**, 164 (2018), 1805.11622.

[234] C. Brust, P. Maksimovic, A. Sady, P. Saraswat, M. T. Walters, and Y. Xin, JHEP **04**, 079 (2015), 1410.0362.

[235] Z. Hoenig et al. Phys. Rev. D **90**, 023 (2014), 1408.1075.

[236] X. Glorot, A. Bordes, and Y. Bengio, in *Proceedings of the Fourteenth International Conference on Artificial Intelligence and Statistics* (PMLR, Fort Lauderdale, FL, USA, 2011), vol. 15 of *Proceedings of Machine Learning Research*, pp. 315–323, URL http://proceedings.mlr.press/v15/glorot11a.html.

[237] A. M. Saxe, J. L. McClelland, and S. Ganguli, CoRR **abs/1312.6120** (2013), 1312.6120, URL http://arxiv.org/abs/1312.6120.

[238] G. E. Hinton, N. Srivastava, A. Krizhevsky, I. Sutskever, and R. Salakhutdinov, CoRR **abs/1207.0580** (2012), 1207.0580, URL http://arxiv.org/abs/1207.0580.

[239] F. Chollet et al., *Keras*, https://keras.io (2015).

[240] M. Abadi, A. Agarwal, P. Barham, E. Brevdo, Z. Chen, C. Citro, G. S. Corrado, A. Davis, J. Dean, M. Devin, et al., *TensorFlow: Large-scale machine learning on heterogeneous systems* (2015), software available from tensorflow.org, URL https://www.tensorflow.org/.

[241] P. T. Komiske, E. M. Metodiev, and J. Thaler, JHEP **04**, 013 (2018), 1712.07124.

[242] T. Faucett et al. (2018).

[243] G. Aad et al. (ATLAS) (2015), 1608.02372.